

# Drag and drop of pores during grain boundary migration

Dissertation

zur Erlangung des akademischen Grades  
eines Doktors der Naturwissenschaften  
an der Fakultät für Geowissenschaften  
der Ruhr-Universität Bochum.

Vorgelegt von

*Elena Petrishcheva*

aus Obninsk, Russland.

Bochum, den 21.11.2006

Referees

*Prof. J. Renner*

*Prof. K. Hackl*

*Prof. S. Chakraborty*

Hiermit versichere ich, Elena Petrishcheva, dass ich die vorliegende Dissertation selbständig und ohne unerlaubte Hilfe verfaßt und an keiner anderen Hochschule eingereicht habe.

21.11.2006

Elena Petrishcheva



# Preface

I am grateful to my parents, Vyacheslav Petrishchev and Galina Petrishcheva who have ever been so very much concerned about raising their younger daughter and provide the best education available.

I am grateful to my husband Shalva Amiranashvili and to my sons Tamas and Artemi who were infinitely patient and supportive during my Ph.D. work.

It has been a very positive experience to work in the stimulating atmosphere of the earth-science department of Ruhr-University Bochum. I want to thank my mentor Prof. Jörg Renner for giving me the opportunity to join the Institute of Geology, Mineralogy and Geophysics as a doctoral student. It was him, who suggested the challenging thesis topic and who guided my work with great enthusiasm. Through his competence in the field I could attain deep insights into a physical problem and its relevance for geo-materials research. Financial support from SFB 526 is gratefully acknowledged.

Some of the ideas presented here emerged from discussions with Prof. Rainer Abart. He made me familiar with thermodynamic principles, kinetic concepts, and he pointed out some petrological implications of my studies. I want to thank him for his support of my work.

At this point a long list of friends and colleagues from Bochum and Berlin should follow. Being convinced that each of them knows about his/her contribution to this work I omit the names and give my sincere thanks to all of you.



# Contents

|          |  |           |
|----------|--|-----------|
| <b>1</b> | <b>Introduction</b>                                | <b>9</b>  |
| 1.1      | Grains and boundaries . . . . .                    | 10        |
| 1.2      | Grain growth . . . . .                             | 11        |
| 1.3      | Pores . . . . .                                    | 13        |
| 1.4      | Drag and drop . . . . .                            | 14        |
| 1.5      | Grooving . . . . .                                 | 18        |
| <b>2</b> | <b>Grain boundaries</b>                            | <b>21</b> |
| 2.1      | Boundary mobility . . . . .                        | 21        |
| 2.2      | Description of boundary motion . . . . .           | 22        |
| 2.2.1    | Physical reasoning . . . . .                       | 22        |
| 2.2.2    | Dynamic equation for a boundary . . . . .          | 24        |
| 2.2.3    | Motion due to surface tension . . . . .            | 26        |
| 2.3      | Examples of boundary motion . . . . .              | 27        |
| 2.3.1    | Stationary solutions . . . . .                     | 28        |
| 2.3.2    | Uniform boundary motion . . . . .                  | 30        |
| 2.3.3    | Pore effect on boundary mobility . . . . .         | 33        |
| 2.4      | Boundary motion in two dimensions . . . . .        | 36        |
| 2.4.1    | Basic equations . . . . .                          | 36        |
| 2.4.2    | Exact results . . . . .                            | 38        |
| <b>3</b> | <b>Pore motion by surface diffusion</b>            | <b>41</b> |
| 3.1      | Physical mechanism . . . . .                       | 42        |
| 3.2      | General properties of the basic equation . . . . . | 45        |
| 3.2.1    | Analysis of dimensions . . . . .                   | 45        |
| 3.2.2    | Stationary solutions . . . . .                     | 46        |
| 3.2.3    | Small slope approximation . . . . .                | 47        |
| 3.2.4    | Semi-scale solution . . . . .                      | 48        |
| 3.2.5    | Two-dimensional case . . . . .                     | 48        |
| 3.3      | Pore at a grain boundary . . . . .                 | 52        |
| 3.3.1    | Small slope approximation . . . . .                | 53        |

|          |   |            |
|----------|---|------------|
| 3.3.2    | Mobility of a pore at a grain boundary . . . . .      | 56         |
| 3.3.3    | Numerical solutions and critical velocities . . . . . | 63         |
| 3.3.4    | Bifurcation . . . . .                                 | 66         |
| 3.4      | Pore at a triple junction . . . . .                   | 68         |
| 3.4.1    | Pore mobility at a triple junction . . . . .          | 70         |
| 3.4.2    | Numerical solutions and critical velocities . . . . . | 78         |
| <b>4</b> | <b>Motion by diffusion through the fluid</b>          | <b>83</b>  |
| 4.1      | Basic equations . . . . .                             | 83         |
| 4.1.1    | Mathematical model . . . . .                          | 86         |
| 4.1.2    | Example . . . . .                                     | 87         |
| 4.2      | Plane interface . . . . .                             | 89         |
| 4.2.1    | An estimate of the critical velocity . . . . .        | 91         |
| 4.3      | Channel-like pore . . . . .                           | 91         |
| 4.3.1    | Pore Mobility . . . . .                               | 96         |
| 4.3.2    | Critical velocity . . . . .                           | 97         |
| 4.4      | Lenticular pore . . . . .                             | 98         |
| <b>5</b> | <b>Conclusions</b>                                    | <b>103</b> |
| 5.1      | Boundary motion . . . . .                             | 104        |
| 5.2      | Pore motion by surface diffusion . . . . .            | 105        |
| 5.3      | Diffusion through the pore-filling fluid . . . . .    | 106        |



# Chapter 1

## Introduction

Though quite differently motivated, material scientists and geoscientists share an interest in quantifying the interaction between moving grain boundaries and pores. Two principal processes are to be distinguished, *drag*, i.e., the pore remains attached to the moving boundary, and *drop*, i.e., the pore separates from the boundary into the bulk crystal. Since remaining porosity may have negative effects on the performance and physical properties of sintered or hot-pressed materials but also of thin films and coatings, production protocols aim to avoid separation conditions. For the geoscientist, pores and their fillings present in constituting minerals of rocks presently exposed on the Earth's surface bear important information on the conditions that prevailed during their formation at depth. It is crucial for the preservation potential of fluid inclusions, whether they are attached to grain boundaries or isolated within the grain interior. The goal of this thesis is to quantify these *drag and drop conditions* for different pore geometries and different mechanisms of pore motion. We start with an introductory chapter that explains basic physical concepts concerning boundaries and pores, illustrate the notions of pore mobility and critical velocity using Zener's drag as a simple example, and introduce basic physical mechanisms responsible for atom transport using the analogy with the grooving process. In the second chapter, boundary motion due to surface tension is considered. In particular, boundaries that are moving with a constant velocity are systematically discussed, the corresponding solutions are used to consider coupled pore-boundary motion thereafter. The mathematical techniques developed for boundaries in this chapter are also used to describe the dynamics of the pore-grain interface in the two following chapters. Chapters III and IV form the heart of the thesis. They are devoted to pore motion controlled by surface diffusion and by diffusion through the pore-filling fluid, respectively. The main objective is to calculate pore mobilities and critical velocities. These mobilities are used to quantify

mobilities of the complex pore-boundary systems and, in particular, to investigate the pore effect on boundary mobility. The results obtained are finally summarized and discussed in Chapter V. The main results concerning boundary motion and pore motion due to surface diffusion have been published in [Petrishcheva and Renner, 2005]. The results on pore motion controlled by diffusion through the pore-filling fluid were presented at two international conferences [Petrishcheva et al., 2006a] and [Petrishcheva et al., 2006b] (the corresponding paper is in preparation).

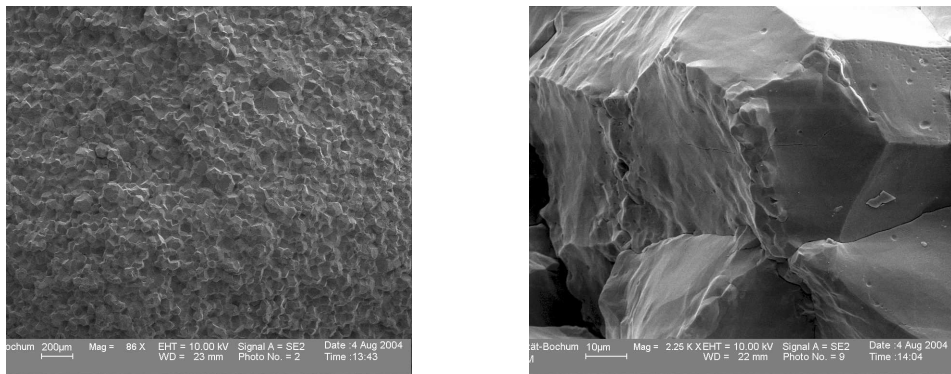


Figure 1.1: Scanning electron microscope (SEM) image of a synthetic marble. Left: grain structure of a polycrystal. Right: neighboring grains on a larger space scale.

## 1.1 Grains and boundaries

All solids have a boundary or an interface, where they are in contact with their environment. In addition, the majority of solids (e.g., ceramics, metals, rocks) are polycrystalline aggregates, i.e., they have a class of imperfections, which are internal interfaces. Polycrystals can be thought of as a set of single phase *domains* or *grains* surrounded by interfaces (Fig. 1.1). These boundary networks are common in nature and have features similar to soap films, arrays of biological cells, and even geographical and ecological territories [Weaire and Rivier, 1984].

A typical boundary (Fig. 1.2) is a macroscopically two-dimensional object with an extremely small characteristic width; the latter can be only several inter-particle distances [Beck, 1954]. Nevertheless, these boundaries determine the microstructure of the material, which in turn controls a wide range of technologically important properties including mechanical strength, toughness, electrical conductivity and magnetic susceptibility [Arzt, 1998].

The nature of the boundary network also has an important effect on different transport processes, because the diffusivity of the atoms inside the boundaries is generally high compared to that within the grains (see, e.g., [Kaur *et al.*, 1995] and [Shewmon, 1964]). Therefore the boundary network is important for physical processes related to the rapid transport of material either across or along the boundaries.

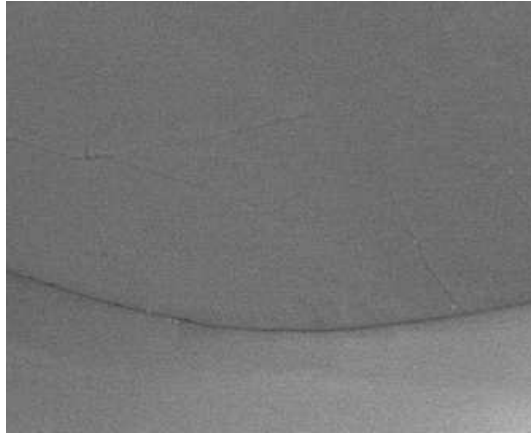


Figure 1.2: SEM microphotograph of a typical boundary in synthetic marble. Note, that the boundary is smooth on this space scale and thus a continuum approach can be followed.

## 1.2 Grain growth

Grain growth is the process by which the mean grain size of a polycrystalline aggregate increases [Yan *et al.*, 1977]. Given sufficiently high temperature or long time, a polycrystal will ideally evolve towards a single crystal. The driving forces that are responsible for the grain growth and the grain boundary migration are determined not only by the physical constants and bulk matrix characteristics but also by the shapes and dimensions of the individual grains. In many cases these forces can be associated with the surface tension of the grain boundaries [Burke, 1948].

The systematic and quantitative description of a large number of differently shaped grains is a challenge. In general, only topological statements about grain shapes can be made, as first suggested in [Smith, 1948a, Smith, 1952] (see later reviews [Smith, 1964a] and [Smith, 1964b] for considerations of relevant metallurgical applications of topology). Careful investigation shows that so called normal grain growth has two main attributes,

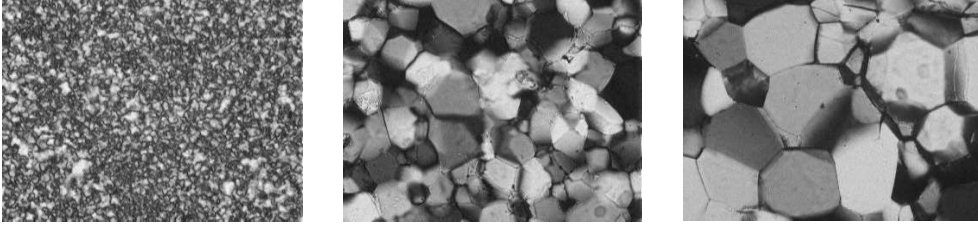


Figure 1.3: Increase of mean grain size during annealing of a quartzite with time. Optical microphotographs are courtesy of J. ter Heege.

namely (a) uniform appearance, i.e., a relatively narrow range of grain sizes is maintained, and (b) scaling or self-similar behavior, i.e., a simple change in scale is sufficient to make two distributions in sizes at two widely separated points in time coincide with each other [Atkinson, 1988]. One can then assume that this distribution is universal and that a statistical approach to the grain growth description can be followed, as first suggested in [Feltham, 1957]. An object of interest is the distribution function that shows how many grains can be found at a given time in a given size interval.

In the simplest case one asks how the averaged diameter of a grain  $D(t)$  changes with time. Note, that the very definition of  $D(t)$  is nontrivial, because we have to estimate the mean radius of a three-dimensional object, whereas for most applications the information as seen in Fig. 1.3 is essentially two-dimensional. Different approaches to this problem are reviewed in, e.g., [Underwood, 1970, Exner, 1972]. After  $D(t)$  is defined one can quantify its evolution. A parabolic relationship for grain growth kinetics was first established in a classical paper of the early 1950s [Burke and Turnbull, 1952]. It can be expressed by the relation [Feltham, 1957]

$$D(t)^2 - D(0)^2 = \frac{\Omega a \gamma_b}{\hbar} e^{-H/kT} \cdot ct$$

where  $\Omega$  is volume per atom,  $\gamma_b$  is the boundary surface tension coefficient,  $a$  is the lattice spacing. The activation energy for the grain-boundary self-diffusion is denoted by  $H$  and a numerical constant  $c \approx 1$ .

Further development of the statistical approach is related to different mean field theories as formulated in [Hilbert, 1965, Louat, 1974, Hunderi and Ryum, 1980]. A typical result is an evolution equation for the distribution function and analytical or numerical analysis of its asymptotical behavior for large times.

From the experimental side, many measurements of distribution functions have been presented. In particular, the time dependence has been found to asymptotically approach  $D(t) \sim t^{1/n}$  with  $n = \text{const}$  for the mean

grain size. Normal grain growth corresponds to the parabolic  $n = 2$  value, however, many different values from  $n = 2$  to  $n = 4$  have been found (e.g.,  $n = 4$  in *Al* [Gordon and Bassyouni, 1965],  $n \approx 2.5$  in *Fe* [Hu, 1974] and in *Pb* [Bolling and Winegard, 1958, Drolet and Galibois, 1968],  $n = 2.0$  and  $n = 2.3$  in *Sn* [Holmes and Winegard, 1959, Drolet and Galibois, 1968], etc.). Measurements of grain growth in ceramics and in rocks also demonstrate that the simple parabolic law is often violated (e.g., [Atkinson, 1988, Evans et al., 2001, Renner et al., 2002a]). Also a dependence of the exponent  $n$  on system parameters such as temperature was reported [Hu, 1974].

Because of all these difficulties any general consideration of the coupled pore-boundary motion would be extremely complicated. This is why we typically consider the grain boundary on a finite time interval so that its velocity can be assumed to be constant. Existence of such simple partial solutions for the boundary motion problem can be explicitly demonstrated at least for simple boundary geometries (see Chapter 2).

### 1.3 Pores

Pores constitute another class of objects that is often encountered in polycrystals. A pore can be considered as a small inclusion in a matrix. Such inclusions are shown in Fig. 1.4. They may occur because of different reasons. One typical situation corresponds to two-phase systems, where the second phase is generated in the form of small bubbles, e.g., the bubble can be filled with melt. Another geologically relevant case is represented by pores filled with aqueous solutions, where dissolution-precipitation and diffusion processes of matrix atoms in the solution become important [Hollister and Crawford, 1981, Roedder, 1984]. Also we are interested in gas filled pores, where the important processes are evaporation-condensation and surface diffusion on the interface.

The geometry of a pore depends on its position. A pore that is included in the matrix typically has spherical shape. Note, that the pore-boundary interfaces (e.g., in Fig. 1.5) are smooth (all characteristic space scales are much larger than the distance between the atoms) so that one can hope to describe them by well defined continuous fields for all relevant quantities, e.g., solution concentration or interface curvature. While it is acknowledged that the transport is realized by individual atoms, our considerations are based on a continuum approach. In particular, for all transport mechanisms considered below the equilibrium pore shape corresponds to a constant curvature, i.e., to a spherical pore form. The pores that are attached to the boundaries differ from those inside the grains. They are described in the next section.

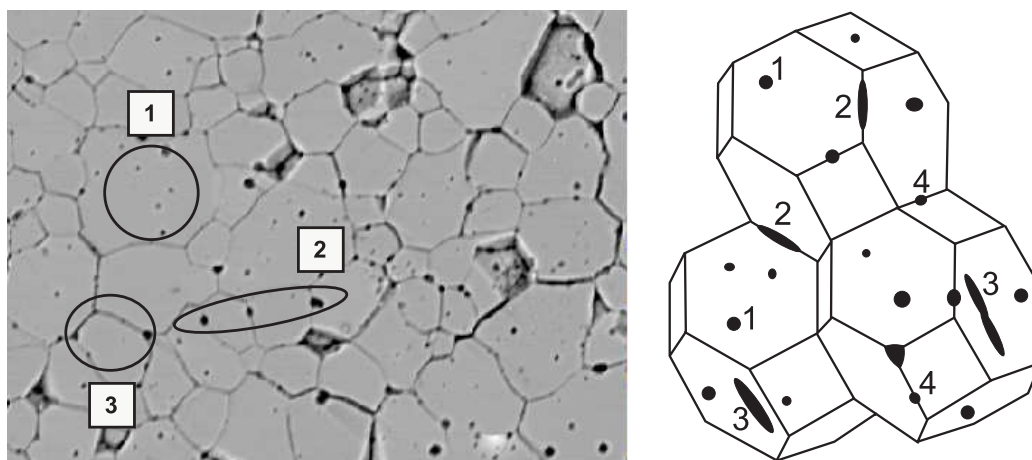


Figure 1.4: Left: example of argon-filled pores within a synthetic marble. Three situations should be distinguished: (1) pores in grains, (2) pores trapped at grain boundaries, (3) pores at triple junctions. Right: mathematical model of a space-filling set of the grains. Also pores with the different geometries are shown schematically. (1) lenticular pore between grains, (2) channel-like pore at a triple junction, (3) channel-like pore at a boundary, (4) lenticular pore at a triple junction.

## 1.4 Drag and drop

A pore can be positioned within a grain, on the interface between two grains (at a grain boundary), or on the line formed by the intersection of three grains (triple junction). Even in the first case the mutual interaction between the pore and the grain boundary may become important during grain growth that inevitably leads to “collisions” between the moving boundaries and interior pores. Also intrinsic pore-motion mechanisms (e.g., temperature gradient) can come into play.

The geometry of a pore at a boundary strongly depends on the dihedral angle, which is determined by force balance at the pore tip [see Eq. (3.20)]. For instance, for the channels at triple junctions (Fig. 1.6), the general notion is that they exist if the dihedral angle is less than some critical value. Most authors consider the critical dihedral angle to be  $\pi/3$ ; it was argued, however, that such channels also exist at larger dihedral angles in partially molten systems, if the melt fraction is high [von Bargen and Waff, 1986]. Two evolution scenarios are possible for pores, which are attached to a migrating grain boundary: (i) the pore may be trapped by the boundary and move with it (Fig. 1.5 left) or (ii) it may be dropped (Fig. 1.5 right), if the velocity of the migrating boundary is too high. In the first case, the principle

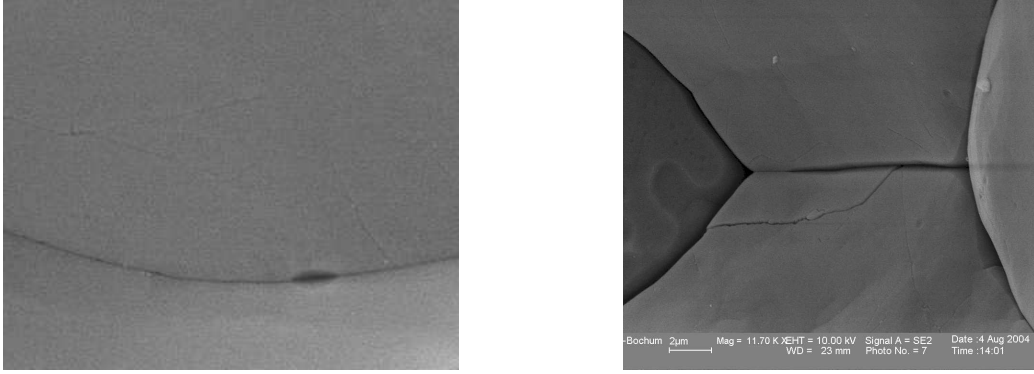


Figure 1.5: Left: pore trapped by the boundary. Right: pore that appears in the process of separation from a triple junction.

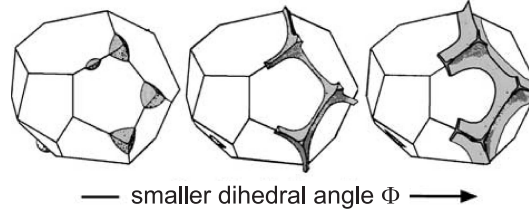


Figure 1.6: Schematic sketch (see [Takei, 2002]) to illustrate that pore geometry is strongly affected by dihedral angle.

question to be addressed in this thesis is: how the mobility of the boundary is affected by pores. To this end, the mobility of the pore-boundary complex is calculated. In the second case, drag and drop conditions become important. To illustrate them and to introduce concepts of drag force, pore mobility, and critical velocity let us consider a simple example following Zener's ideas first published in [Smith, 1948b]. Let us assume that the pore-grain surface tension coefficient is much larger than the grain-grain surface tension and correspondingly the dihedral angle is close to  $\pi$  [as defined in Eq. (3.20)]. In this case the pore can be approximated as a rigid inclusion. We assume that the mobility of this particle is known. The drag force reads

$$K_{\text{drag}} = 2\pi r \gamma_b \sin \Theta,$$

where  $\Theta$  is the drag angle, and  $\gamma_b$  is the energy density in units of [Energy/Area] at the boundary (Fig. 1.7). The radius of the contact circle  $r = R_p \cos \Theta$  with  $R_p$  being the radius of the spherical pore. Therefore the drag force

$$K_{\text{drag}} = 2\pi R_p \gamma_b \sin \Theta \cos \Theta$$

and the particle velocity is given by

$$U_p = \pi R_p \gamma_b M_p \sin 2\Theta,$$

where  $M_p$  is the mobility of the particle.

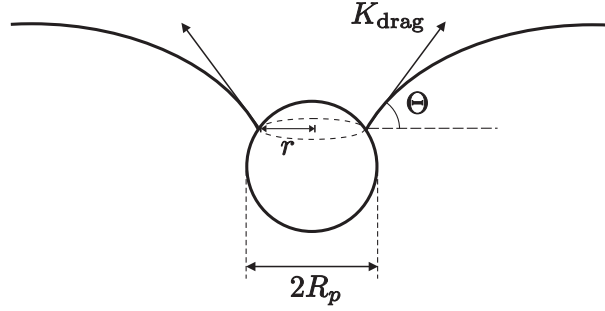


Figure 1.7: Geometry used for the calculation of the Zener drag on a spherical inclusion.

The drag force achieves its maximum value for  $\Theta = \pi/4$ . Particle drag at this condition is referred to as Zener drag

$$K_{\text{Zener drag}} = \pi R_p \gamma_b. \quad (1.1)$$

Therefore the velocity of a rigid inclusion cannot exceed the critical value

$$U_{\text{max}} = \pi R_p \gamma_b M_p. \quad (1.2)$$

If the velocity of the boundary exceeds this limit, the inclusion is separated from the boundary. It stays behind the moving boundary and remains as an isolated inclusion in the interior of the grain.

The conclusion on the existence of a maximum pore velocity that separates drag and drop scenarios is very general. The above calculation of this velocity and its generalizations, as reviewed in [Nes *et al.*, 1985], have, however, several weak points. One point is the assumption that the pore shape is fixed and spherical. In contrast, the pores in Fig. 1.5 are evidently strongly deformed because of pore-boundary interaction. In other words, one has to generalize Zener's calculation for arbitrary dihedral angles. Another difficulty is related to the pore mobility. As we will see, near the critical velocity the dependence between the drag force and the resulting pore velocity is non-linear. Strictly speaking, the concept of the pore mobility cannot be used in this context. Last but not least, different mechanisms can be responsible for pore motion. These mechanisms must be accounted for before making any quantitative conclusions on the critical velocity. Two mechanisms that are



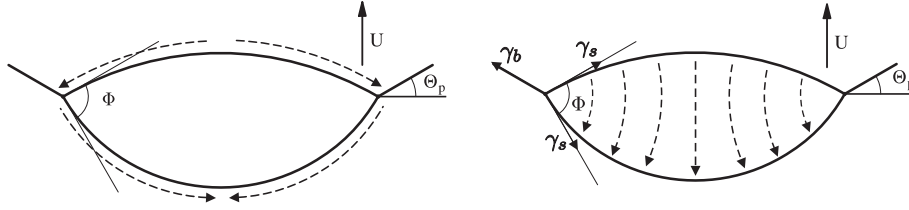


Figure 1.8: Two mechanisms that can be responsible for material transport and pore motion. Atomic fluxes are indicated by the dashed arrows. Left: surface diffusion. Right: diffusion through the fluid-phase. In any case, equilibration of surface tension forces at the pore tip determines the dihedral angle  $\Phi$ . Pore velocity  $U$  is determined by the drag angle  $\Theta_p$ .

examined in this thesis, namely, surface diffusion and diffusion through the fluid-phase are illustrated in Fig. 1.8.

The existing investigations concerning drag and drop conditions are rather contradictory and incomplete. For a pore whose motion is controlled by surface diffusion the critical velocities for arbitrary dihedral angles were first calculated in [Hsueh *et al.*, 1982] and [Spears and Evans, 1982]. In these papers a solution for stationarily moving pores and boundaries was obtained by direct numerical integration of the underlying equations. The calculated critical velocities were found to be strongly dependent on the dihedral angle. In particular, the critical velocity was zero for a spherical pore, in sharp contradiction to Zener's calculation. These results were criticized, because of the unnatural assumption that the pore volume is conserved during pore-boundary interaction. More general dynamical solutions were obtained in [Svoboda and Riedel, 1992] and [Riedel and Svoboda, 1993]. However, the critical velocities were of the same order and again strongly dependent on the dihedral angle. This problem was reconsidered in [Yu and Suo, 1999] (again under the assumption of constant pore volume and without mention of [Svoboda and Riedel, 1992, Riedel and Svoboda, 1993]), where solutions for stationary motion were obtained using appropriate implementation of a finite element method. In contrast with [Hsueh *et al.*, 1982, Spears and Evans, 1982], the critical velocities were found to be only slightly dependent on dihedral angle.

The description of pore motion that is controlled by diffusion through the pore-filling fluid is more complicated mathematically and only rough estimates of mobilities and critical velocities [Monchoux and Rabkin, 2002] can be found in the literature. To our knowledge, the effect of dihedral angle was not investigated at all. The lack or wide scatter of the published data can be understood if we recall that the separation is a highly nonlinear process

that appears as a singularity of the numerical solutions. Evidently, modelling of the singular solutions is rather tricky. Therefore the numerical solutions obtained in this thesis were justified by accurate analysis of the singularity and underlying bifurcation.

## 1.5 Grooving

Physical mechanisms that can control pore motion and pore-boundary separation are realized by atomic transport across the pore. The transport occurs via diffusion through the pore-filling fluid or via surface diffusion. Fortunately, these processes have been already investigated in the context of *grooving* studies. The relevance of these studies for the pore motion problem at hand is twofold. On the one hand, grooving constitutes a diffusion process with moving boundaries too, and corresponding model equations can be adopted even though different particular solutions are sought. On the other hand, in contrast to pores inside a polycrystalline aggregate grooves are accessible to direct investigation. Therefore studies of grooving kinetics have served as indirect means of determining important transport parameters, such as surface diffusion coefficients (see, e.g. [Mullins and Shewmon, 1959]).

A groove will develop on the surface of a polycrystal whenever a stationary grain boundary intersects the surface (Fig. 1.9). In contrast to the pore, it has a two-dimensional geometry and is positioned on the crystal surface.

Here, a plane surface is not a stationary one, because the force equilibrium condition must be met at the intersection point. Therefore a long channel [with the dihedral angle determined by Eq. (3.20)] is formed and serves as a seed perturbation for the further growth of the groove. Mention was made that the underlying physical processes are identical to those responsible for the pore drag and drop (Fig. 1.8). Actually we can directly adopt the corresponding set of partial differential equations for our needs. The known solutions can, however, not be applied directly for our purposes, because of two reasons. One reason is that the popular small slope approximation (i.e., linear limit of the mathematical model) is not appropriate for moderate and large dihedral angles and in any case does not describe pore drop. The other reason is that grooving as such is described by the semi-scale solutions of the underlying equations, whereas pore drag corresponds to special solutions that are stationary in a moving coordinate frame.

Actually grooving can be described by several mathematical theories, because under different conditions the dominant physical process also is different. In the classical paper [Mullins, 1957] two processes: evaporation-condensation and surface diffusion were considered separately. Nonlinear

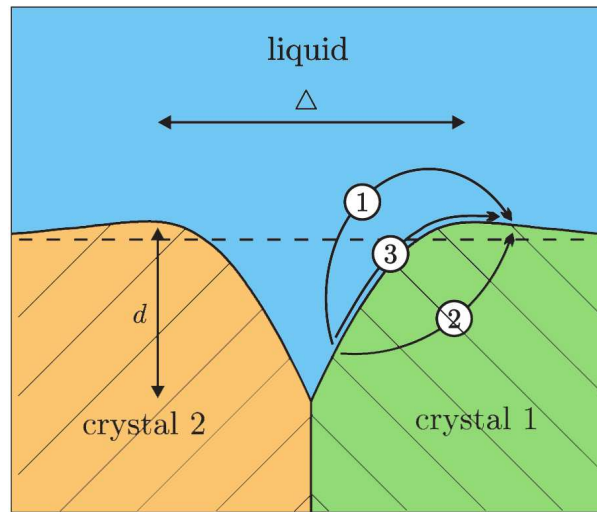


Figure 1.9: A typical cross section of a polycrystal surface and a grain boundary. Here, a groove is permanently developing at the intersection point. Particle fluxes due to (1) dissolution-precipitation (2) volume diffusion inside the matrix, and (3) surface diffusion are schematically shown by arrows.

generalizations of the corresponding mathematical equations are applied in the present thesis in Chapter 2 for the description of the boundary motion and in Chapter 3 for the pore drag and drop due to surface diffusion. Grooving due to diffusion through the filling fluid that is permanently accompanied by the dissolution-precipitation processes was considered in [Mullins, 1960]; the corresponding model is used as a starting point in Chapter 4. Also several additional mechanisms, e.g., stress effect [Genin *et al.*, 1993] or orientation effect [Ramasubramaniam and Shenoy, 2005] on grooving, were considered in the literature. Potentially they are of great interest for the pore drag and drop problem but these effects are beyond the scope of this thesis.



# Chapter 2

## Grain boundaries

In this chapter we consider general aspects concerning boundary motion, i.e., its physical reasons, corresponding mathematical models, problem posing, and typical solutions. These considerations give us the necessary basis for the heart of this thesis, which is contained in Chapters 3 and 4, where common motion of pores and boundaries is considered.

### 2.1 Boundary mobility

The physical concept of *mobility* is generic and seemingly simple. Considering a boundary, let us assume that its unit area is affected by a distributed force  $\boldsymbol{\sigma}$  that is measured in force-per-area units. A drag force  $\mathcal{K}_b$ , actually pressure, is defined as the component of  $\boldsymbol{\sigma}$ , which is normal to the boundary. The physical reasons for the drag may be different. One can mention, for instance, differences in the chemical potential of the constituent thermodynamic components during a phase transition, when the phases are not identical on the opposing sides of the interface. Alternatively, the drag force may be due to temperature gradients, externally applied stresses, etc. As suggested by physical intuition and supported by experimental data, the resulting normal boundary velocity  $v_b$  is typically proportional to  $\mathcal{K}_b$ , i.e.,

$$v_b = \mu_b \mathcal{K}_b, \tag{2.1}$$

where the proportionality coefficient  $\mu_b$  is referred to as the boundary mobility (Fig. 2.1). Equation (2.1) implies that the drag force is small enough for the linear proportionality to be valid. The boundary mobility is a local quantity, because it refers to small area elements of the boundary. The mobility may have different values for different elements, and it may also depend on element orientation. For simplicity, however, it is assumed to be uniform and

isotropic. Microscopically boundary mobility is related to the flux of atoms across the boundary: matrix atoms are transferred from the shrinking into the growing grain. An explicit value of  $\mu_b$  can be derived from experimental data. It can also be theoretically calculated by applying a specific physical model that describes the transport of atoms due to microscopical forces. Within the scope of this thesis  $\mu_b$  is considered a constant quantity.

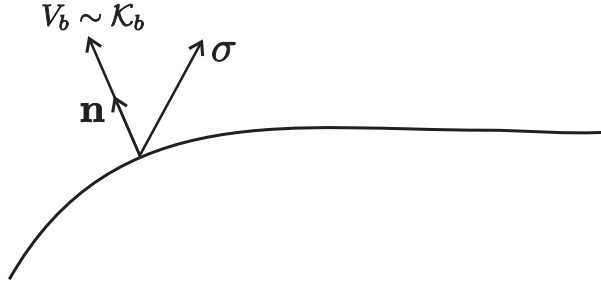


Figure 2.1: Boundary velocity is proportional to the normal component  $\mathcal{K}_b$  of the applied force. The proportionality coefficient is the boundary mobility  $\mu_b$ .

## 2.2 Description of boundary motion

### 2.2.1 Physical reasoning

Let us now turn to the boundary motion that results from a drag. We consider a single phase interface with identical phases on each side of the boundary between the grains. In this case the drag force is usually caused by surface tension [Burke, 1948] quantified by the surface tension coefficient  $\gamma$ , which is the excess of a free energy per unit area of the interface with respect to the free energy of the grain interior. It is measured in energy-per-area units. The surface tension coefficient can be nonuniform and can also depend on the interface orientation, because of the anisotropy of the crystalline materials that constitute the grains. Nevertheless, for the sake of simplicity, it is considered an isotropic uniform constant. The corresponding total excess energy is proportional to the total area of the interfaces. As a result interfaces will tend to migrate in such a way as to reduce their area. For curved surfaces, this implies that they migrate toward their center of curvature, e.g., a spherical grain will tend to shrink and disappear.

The surface tension can also be related to forces. Let us calculate a normal force  $\mathcal{K}_b dS$  that acts on a small element  $dS$  of the boundary due to surface tension. The reason for this force is a possible change of the element area (and

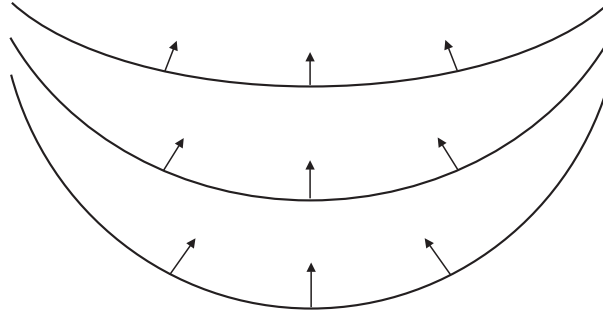


Figure 2.2: A curved interface migrates to reduce its area, i.e., toward its center of curvature.

its surface energy) as the element moves. Let  $\delta$  be the normal displacement of the element towards its center of curvature as shown in Fig. 2.2. The corresponding change (decrease) of the system surface energy is  $-\mathcal{K}_b dS \cdot \delta$ . It is also equal to  $\gamma(dS_{\text{new}} - dS)$ , where

$$dS_{\text{new}} = dS - \delta(\kappa_1 + \kappa_2)dS$$

is the new element area after the shift and  $\kappa_{1,2}$  are the two principal curvatures of the boundary. The curvatures are taken positive if the boundary is concave with respect to the growing grain. We derive that the local driving force per unit area of the boundary is given by the well known expression

$$\mathcal{K}_b = \gamma_b \kappa, \quad (2.2)$$

where  $\kappa = \kappa_1 + \kappa_2$  is the mean curvature and  $\gamma_b$  is the surface tension coefficient of the boundary.

As a simple example let us consider the *collapse* of a small spherical grain with the radius  $R(t)$  within a homogeneous matrix grain. Let the boundary normal vector be directed from the growing grain to the shrinking one, i.e., towards the center of the sphere. The projection of the boundary velocity is

$$v_b = -\frac{dR}{dt} > 0$$

and the main curvatures read

$$\kappa_1 = \kappa_2 = \frac{1}{R}.$$

Therefore the drag force equals  $2\gamma_b/R$ . In this case Eqs. (2.1) and (2.2) reduce to

$$\frac{dR}{dt} + \frac{2\mu_b\gamma_b}{R} = 0$$

and can be directly integrated

$$R(t) = \sqrt{R_0^2 - 4\mu_b\gamma_b t}, \quad (2.3)$$

where  $R_0$  is the initial radius of the grain. The latter disappears at the moment  $t_0 = R_0^2/(4\mu_b\gamma_b)$ .

Another simple example is the collapse of a cylindrical inclusion, where  $\kappa_1 = 0$  and  $\kappa_2 = 1/R$ . The drag force equals  $\gamma_b/R$ . In this case

$$R(t) = \sqrt{R_0^2 - 2\mu_b\gamma_b t}. \quad (2.4)$$

These exact analytical results are possible because of the simple geometry. A general situation is not so easily tractable and is described by a nonlinear partial differential equation that is derived in the next section.

### 2.2.2 Dynamic equation for a boundary

In this section we derive a general equation for grain boundary motion. The equation contains a general drag force that may be specified in different ways for different drag mechanisms. Let us assume that the growing grain is described as a solution of an inequality

$$\mathcal{F}(\mathbf{r}, t) \leq 0, \quad (2.5)$$

e.g.,

$$R(t)^2 - x^2 - y^2 - z^2 \leq 0$$

if the grain grows to fill a spherical inclusion. Such a *level set function*  $\mathcal{F}(\mathbf{r}, t)$  provides us with a flexible and powerful tool to handle complicated moving boundary problems. In particular, the boundary as such is given by an implicit equation

$$\mathcal{F}(\mathbf{r}_b, t) = 0, \quad \text{if and only if} \quad \mathbf{r} \in \{\mathbf{r}_b\}, \quad (2.6)$$

and is associated with the zero-level set. Here  $\{\mathbf{r}_b\}$  denotes the multitude of radius position vectors of the boundary points.

Let now an arbitrary boundary point  $\mathbf{r}_b = (x, y, z)$  be displaced by  $d\mathbf{r}_b = \mathbf{v}dt$ . Its new position  $\mathbf{r}_b + d\mathbf{r}_b$  should satisfy the same implicit Eq. (2.6) but with  $t$  replaced by  $t + dt$ . Therefore both

$$\mathcal{F}(\mathbf{r}_b, t) = 0 \quad \text{and} \quad \mathcal{F}(\mathbf{r}_b + \mathbf{v}dt, t + dt) = 0,$$



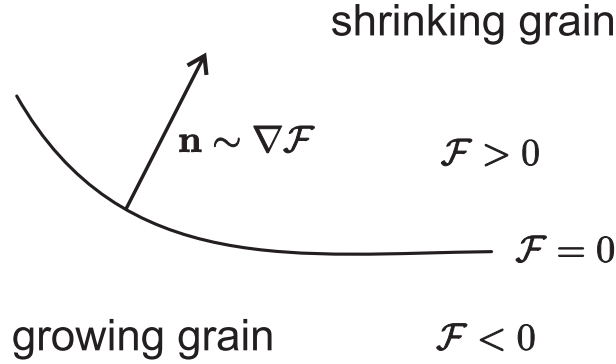


Figure 2.3: It is convenient to specify grain boundaries with a level-set function.

and applying a Taylor expansion to the last identity we arrive at the dynamic equation

$$\partial_t \mathcal{F} + \mathbf{v} \nabla \mathcal{F} = 0, \quad (2.7)$$

which is actually valid for any moving boundary, because of its pure geometrical nature. In principle, the boundary velocity  $\mathbf{v}$  has two components

$$\mathbf{v} = \mathbf{v}_n + \mathbf{v}_\tau,$$

where  $\mathbf{v}_n$  is normal and  $\mathbf{v}_\tau$  is tangential to the boundary. However, the contribution of the tangential component vanishes completely, because  $\nabla \mathcal{F}$  is orthogonal to the boundary as long as the latter is given by the level set Eq. (2.6). The normal component  $\mathbf{v}_n$  equals the boundary velocity as given by Eq. (2.1), i.e.,

$$\mathbf{v}_n = \mathbf{v}_b = \mu_b \mathcal{K}_b \mathbf{n}, \quad (2.8)$$

where

$$\mathbf{n} = \frac{\nabla \mathcal{F}}{|\nabla \mathcal{F}|}$$

is a unit vector directed normal to the boundary. Note, that  $\nabla \mathcal{F}$  points in the direction, where  $\mathcal{F}$  increases most rapidly, and therefore  $\mathbf{n}$  is automatically directed *outward* with respect to the grain defined by the inequality (2.5). That is,  $\mathcal{K}_b$  should be understood as a projection of the drag force on the outward unit normal vector. If the drag force is determined by the surface curvature, the drag projection is positive for a boundary, which is concave with respect to the grain in question, as shown in Fig. 2.3, and negative for a convex boundary.

Inserting the boundary velocity (2.8) into (2.7) we obtain the desired dynamic equation for boundary motion

$$\partial_t \mathcal{F} + \mu_b \mathcal{K}_b \sqrt{(\partial_x \mathcal{F})^2 + (\partial_y \mathcal{F})^2 + (\partial_z \mathcal{F})^2} = 0, \quad (2.9)$$

which is a nonlinear partial differential equation. Equation (2.9) is given in the most general and symmetric form, e.g., its rotational symmetry is evident. However, for practical purposes it is worth to rewrite (2.9) assuming that the boundary is given explicitly, e.g., in the vicinity of some point by

$$\mathcal{F}(x, y, z, t) = 0 \quad \Leftrightarrow \quad z = f(x, y, t), \quad (2.10)$$

and the symmetry between the variables is broken. We assume that the grain  $\mathcal{F}(\mathbf{r}, t) \leq 0$  is positioned “below” the boundary and is given by the inequality

$$z \leq f(x, y, t). \quad (2.11)$$

Therefore we insert

$$\mathcal{F}(x, y, z, t) = z - f(x, y, t)$$

into (2.9) and obtain

$$\partial_t f = \mu_b \mathcal{K}_b \sqrt{1 + (\partial_x f)^2 + (\partial_y f)^2}, \quad (2.12)$$

the latter form is less symmetric but more tractable analytically.

### 2.2.3 Motion due to surface tension

Neither Eq. (2.9) nor Eq. (2.12) are complete because an explicit expression for  $\mathcal{K}_b$  is required. This expression depends on the specific problem. We are mostly interested in a special case, where the drag force is provided by the surface tension effect. The drag is then given by Eq. (2.2), and it is always normal to the boundary. We only have to express the mean curvature  $\kappa = \kappa_1 + \kappa_2$  in terms of  $f$ . Such an expression can be found in the textbooks [Dubrovina *et al.*, 1992]

$$\kappa = \operatorname{div} \left( \frac{\nabla f}{\sqrt{1 + |\nabla f|^2}} \right) \quad (2.13)$$

and therefore our basic equation reads

$$\partial_t f = \mu_b \gamma_b \sqrt{1 + |\nabla f|^2} \operatorname{div} \left( \frac{\nabla f}{\sqrt{1 + |\nabla f|^2}} \right). \quad (2.14)$$

To our knowledge, in the context of moving boundaries the two-dimensional limit of this equation was introduced in [Mullins, 1957] for the grooving problem. In the context of nonlinear diffusion similar equations and their semi-scale solutions were originally considered in [Fujita, 1952a, Fujita, 1952b].

Before we proceed it is appropriate to recall our sign conventions (Fig. 2.4). The mean curvature as defined by Eq. (2.13) is positive if the boundary is concave and negative if the boundary is convex with respect to the grain defined by the inequality (2.11). In any case, the projection of the drag force along the unit normal vector directed outside with respect to the grain is given by the expression  $\mu_b \gamma_b \kappa$  and Eq. (2.14) correctly describes the evolution of our boundary with time.

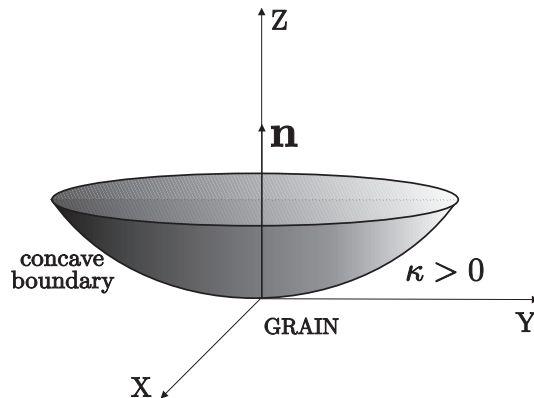


Figure 2.4: Sign conventions for Eq. (2.14).

Equation (2.14) is a closed one. It completely describes boundary motion in an appropriately chosen coordinate frame, if the initial and boundary conditions are properly specified. We now discuss several examples.

## 2.3 Examples of boundary motion

Here we discuss several typical solutions of Eq. (2.14). The main question we are interested in is a special solution for the boundary, which is moving with a constant velocity. Such a solution is used to consider the coupled motion of pores and boundaries in the following chapters.

### 2.3.1 Stationary solutions

Stationary boundaries are described by the equation  $\kappa = \kappa_1 + \kappa_2 = 0$ , i.e.,

$$\operatorname{div} \left( \frac{\nabla f}{\sqrt{1 + |\nabla f|^2}} \right) = 0, \quad (2.15)$$

which still is a complicated nonlinear partial differential equation. Its simplest analytical solution is given by the plane boundary

$$z = \text{const}, \quad \text{i.e.,} \quad f(x, y) = \text{const}.$$

Moreover, the plane boundary is stable. Indeed, inserting an arbitrary small perturbation

$$f = \text{const} + \tilde{f}(x, y, t) \quad (2.16)$$

into Eq. (2.14) and omitting all terms proportional to  $\tilde{f}^2$  we arrive at a linear diffusion equation

$$\partial_t \tilde{f} = \mu_b \gamma_b \nabla^2 \tilde{f}$$

where the parameter  $\mu_b \gamma_b$  is measured in units  $[\text{length}]^2/[\text{time}]$  and serves as an effective diffusion coefficient. We conclude that an initial perturbation  $\tilde{f}$  with a characteristic space scale  $\mathfrak{R}$  disappears on a time scale  $\mathfrak{R}^2/(\mu_b \gamma_b)$  indicating stability. An “energetic” explanation is that the planar interface evidently provides the absolute minimum of the surface area and the surface free energy.

This does, however, by no means imply that an arbitrary boundary necessarily evolves to a plane. In fact, the full set of stationary solutions of Eq. (2.14) is extremely rich. A formal mathematical reason for that is that the boundary conditions for Eq. (2.15), i.e., boundaries of the boundaries, are in general incompatible with plane solutions. The nontrivial equilibrium configurations can be sought by tracing the evolution of  $f(x, y, t)$  via Eq. (2.14) until one of the possible equilibrium states is established (relaxation method). Another possibility is direct minimization of the surface area. Note, that the area is positively defined and therefore its minimum should exist for all physically reasonable boundary conditions.

These *minimal surfaces* are well known and have been intensely investigated in differential geometry [Dubrovin *et al.*, 1992]. Actually, everybody has observed such surfaces when playing with soap films. A simple analytical example is given by a *catenoid*, i.e., a radially symmetric minimal boundary with  $f = f(r)$  and  $r = \sqrt{x^2 + y^2}$  that is shown in Fig. 2.5. In this case the mean curvature reads

$$\kappa = \frac{1}{r} \frac{\partial}{\partial r} \left( \frac{r \partial_r f}{\sqrt{1 + (\partial_r f)^2}} \right). \quad (2.17)$$

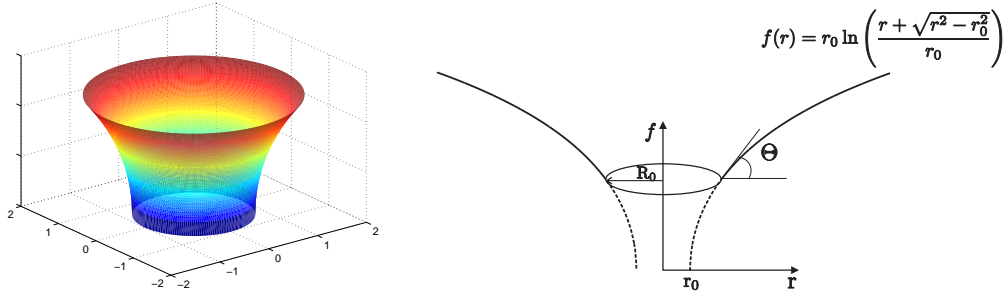


Figure 2.5: A catenoid  $z = f(r)$  given by Eq. (2.18) is observed when, e.g., a soap film, is pinned by a ring. The coordinates are normalized by  $r_0$ .

Therefore Eq. (2.15) is reduced to an ordinary differential equation

$$\frac{r \partial_r f}{\sqrt{1 + (\partial_r f)^2}} = r_0 \quad \text{with} \quad r_0 = \text{const},$$

which can be directly integrated. The solution reads

$$f(r) = r_0 \ln \left( \frac{r + \sqrt{r^2 - r_0^2}}{r_0} \right), \quad (2.18)$$

where the solution is normalized in accord with the condition  $f(r_0) = 0$  and is defined for  $r > r_0$ . It describes, e.g., a boundary that is pinned by a ring-like particle with the radius  $R_0 \geq r_0$  (see Fig. 2.5 and [Nes *et al.*, 1985]). The particle drag angle  $\Theta$  is determined by the relation

$$\tan \Theta = \left. \frac{df}{dr} \right|_{r=R_0} = \frac{r_0}{\sqrt{R_0^2 - r_0^2}}, \quad \text{i.e.,} \quad \sin \Theta = \frac{r_0}{R_0},$$

and the total drag force that acts on the particle and in turn distorts the boundary reads

$$K_{\text{drag}} = 2\pi R_0 \gamma_b \sin \Theta = 2\pi r_0 \gamma_b. \quad (2.19)$$

The drag is determined by the solution parameter  $r_0$  and is formally independent of the ring radius  $R_0$ , but the restriction  $r_0 \leq R_0$  is valid. The maximum possible drag corresponds to the maximum possible  $r_0 = R_0$ , it reads  $2\pi R_0 \gamma_b$ . The corresponding drag angle reads  $\Theta_{\text{max}} = \pi/2$ . We conclude that if a stationary plane boundary is pinned by a ring shaped particle with an external force  $K$  applied to it, a particular solution of the form (2.18) is self-organized. The solution (i.e., an appropriate value of the solution parameter  $r_0$ ) is determined by the equilibrium condition that the external force  $K$

is compensated by the surface tension force  $K_{\text{drag}}$  as given by (2.19). Such a compensation is possible as long as  $K \leq 2\pi R_0 \gamma_b$ . If  $K$  exceeds this limit, the stationary solution does not exist.

A more complicated situation occurs, when the boundary is pinned by a spherical particle (Fig. 1.7). In this case one has to distinguish the self-organized solution parameter  $r_0$ , the particle radius  $R_p$ , and the radius of the contact circle  $R_0$ , where  $r_0 \leq R_0 \leq R_p$  (see [Nes *et al.*, 1985]).

We are now in a good position to stress that we are actually interested in a slightly different situation where a moving boundary meets a stationary particle. There is no equilibrating external force that acts on the particle. In the contrary, the particle moves with the boundary due to the drag. We are interested in conditions for such a common motion. First, we have to consider a special set of dynamic solutions of Eq. (2.14), where the boundary moves with a constant velocity.

### 2.3.2 Uniform boundary motion

Here we assume that the boundary moves along the  $z$  axis (up) with some constant velocity  $U > 0$ . Therefore the time dependence of  $f(x, y, t)$  can be given explicitly, i.e.,

$$f(x, y, t) = F(x, y) + Ut \quad (2.20)$$

and our main Eq. (2.12) reduces to

$$\sqrt{1 + |\nabla F|^2} \operatorname{div} \left( \frac{\nabla F}{\sqrt{1 + |\nabla F|^2}} \right) - \frac{U}{\mu_b \gamma_b} = 0. \quad (2.21)$$

The latter equation can be considerably simplified in the case of radial symmetry  $F = F(r)$ , i.e.,

$$\sqrt{1 + (\partial_r F)^2} \frac{1}{r} \frac{\partial}{\partial r} \left( \frac{r \partial_r F}{\sqrt{1 + (\partial_r F)^2}} \right) - \frac{U}{\mu_b \gamma_b} = 0,$$

or

$$\frac{1}{1 + (\partial_r F)^2} \partial_r^2 F + \frac{1}{r} \partial_r F - \frac{U}{\mu_b \gamma_b} = 0. \quad (2.22)$$

Let us describe a typical problem posing for this equation. We consider a circular moving boundary with the radius  $R_b$  so that the solution should exist for  $0 \leq r \leq R_b$ . We have a second-order differential equation so that two additional conditions must be specified. Equation (2.22) is invariant under translations  $F \rightarrow F + \text{const}$  and without loss of generality one can put  $F(0) = 0$ . Further, the symmetry arguments suggest that  $\partial_r F(0) = 0$ . In

particular, only in this case the solution can be defined in a singular point at  $r = 0$ . We see that actually Eq. (2.22) has an unique solution for given system parameters. Several examples obtained for different values of  $U$  are shown in Fig. 2.6.

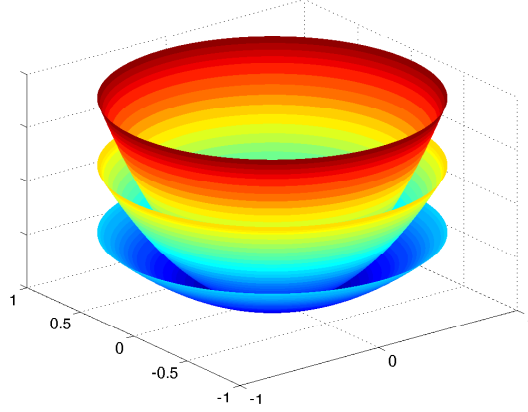


Figure 2.6: Three-dimensional images of a moving boundary  $z = F(r)$  for three different values of its velocity  $U$ , namely  $UR_b/(\mu_b\gamma_b) = 1, 3, 5$ . The deviation from the plane boundary increases with an increase of  $U$ ; the coordinates are normalized by  $R_b$ .

The simplest mathematical treatment of Eq. (2.22) is based on the small slope approximation. The latter assumes small values of the slope angle  $\theta$ , which is defined by the relation

$$\tan \theta = \partial_r F. \quad (2.23)$$

In this case the term  $(\partial_r F)^2$  in Eq. (2.22) can be ignored and (2.22) reduces to a linear equation. Its solution reads

$$F_{\text{small slope}}(r) = \frac{U}{4\mu_b\gamma_b} r^2,$$

the corresponding boundary is a concave paraboloid. The solution indicates that the slope angle

$$\theta = \arctan \frac{Ur}{2\mu_b\gamma_b}$$

gradually increases from zero at  $r = 0$  to the maximal value  $\Theta_b$  at  $r = R_b$ . This maximum value is the drag angle for our boundary. The driving force reads

$$K_{\text{drag}} = 2\pi R_b \gamma_b \sin \Theta_b \approx 2\pi R_b \gamma_b \tan \Theta_b = \frac{\pi R_b^2}{\mu_b} U$$

and is proportional to the velocity. The ratio

$$M_b = \frac{U}{K_{\text{drag}}} = \frac{\mu_b}{\pi R_b^2}, \quad (2.24)$$

should then be interpreted as the global boundary mobility, the latter characterizes the whole boundary instead of its small elements. This simple relation between the local and global mobilities holds as long as the small slope approximation is valid, i.e., if  $\Theta_b \ll 1$ .

To proceed with the general nonlinear case it is natural to transfer from  $F(r)$  to the slope angle variable  $\theta(r)$  defined by Eq. (2.23) and to the normalized length  $\rho = r/R_b$ . Equation (2.22) then takes the form

$$\partial_\rho \theta + \frac{1}{\rho} \tan \theta - \epsilon = 0 \quad (2.25)$$

with

$$0 \leq \rho \leq 1, \quad \theta(0) = 0$$

and

$$\epsilon = \frac{UR_b}{\mu_b \gamma_b} \quad (2.26)$$

being the only dimensionless parameter that uniquely determines the solution  $\theta(\rho, \epsilon)$ . The latter can be found numerically or analytically in the form of Taylor expansion in  $\rho$ . The “last” value of  $\theta(\rho, \epsilon)$  (i.e., for  $\rho = 1$ ) is the boundary drag angle  $\Theta_b(\epsilon)$ . The value of  $\sin \Theta_b(\epsilon)$  determines the drag force. The analytical solution reads

$$\begin{aligned} \theta(\rho, \epsilon) &= \frac{\epsilon \rho}{2} - \frac{\epsilon^3 \rho^3}{96} + \dots, \\ \Theta_b(\epsilon) = \theta(1, \epsilon) &= \frac{\epsilon}{2} - \frac{\epsilon^3}{96} + \dots, \\ \sin \Theta_b(\epsilon) &= \frac{\epsilon}{2} - \frac{\epsilon^3}{32} + \dots \end{aligned} \quad (2.27)$$

The series quickly converge for  $\epsilon \lesssim 1$ , i.e., if the boundary velocity is not too large. For large  $\epsilon$  a numerical solution should be used. Several examples of such solutions are shown in Fig. 2.7. For  $\epsilon \leq 3$  the dependence of  $\theta$  on  $\rho$  is almost linear and the small slope approximation is valid. For larger values of  $\epsilon$  the boundary can be divided in a parabolic “bottom” and almost vertical “sides” with the slope angle close to  $\pi/2$ .



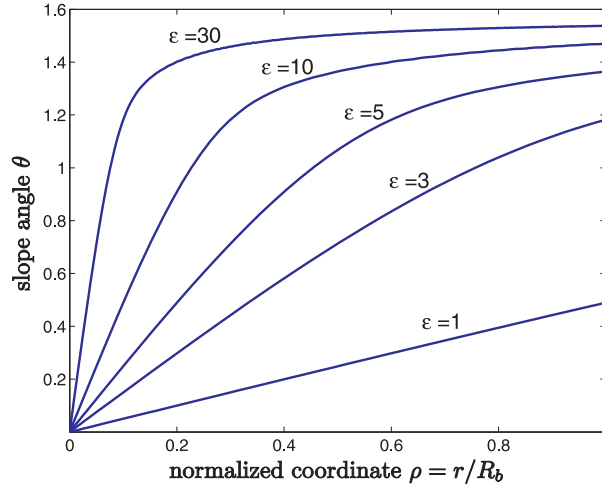


Figure 2.7: Dependence of the boundary slope angle  $\theta$  on the normalized radial coordinate  $\rho$  from numerical solutions of Eq. (2.25) for different values of  $\epsilon$ , as shown by labels.

An important new point is that if we formally introduce the global boundary mobility

$$M_b(\epsilon) = \frac{U}{K_{\text{drag}}} = \frac{\mu_b}{\pi R_b^2} \frac{\epsilon}{2 \sin \Theta_b(\epsilon)} = \frac{\mu_b}{\pi R_b^2} \left( 1 + \frac{\epsilon^2}{16} + \dots \right), \quad (2.28)$$

it depends now on  $\epsilon$  (i.e., on the normalized boundary velocity) indicating nonlinearity of our problem. This dependence was also obtained numerically for  $0 < \epsilon < 6$  (Fig. 2.8). As we see, the nonlinear boundary mobility considerably increases with an increase in velocity. Equation (2.28) is a good approximation for  $\epsilon < 5$ .

Of course, if the boundary is pinned by a particle the solution should be regular only in the interval  $r_0 < r < R_b$ , where  $r = r_0$  is the contact circle. Equation (2.22) allows then for a two-parametric family of the nontrivial solutions.

### 2.3.3 Pore effect on boundary mobility

The focus of this thesis is the coupled motion of pores and boundaries. One particular problem is how the mobility of a boundary is affected by dragged pores. The problem is addressed in this section.

We consider a boundary positioned at  $r < R_b$  that is pinned by a pore positioned at  $r < R_p$ , where  $R_p < R_b$ . The system moves with the common

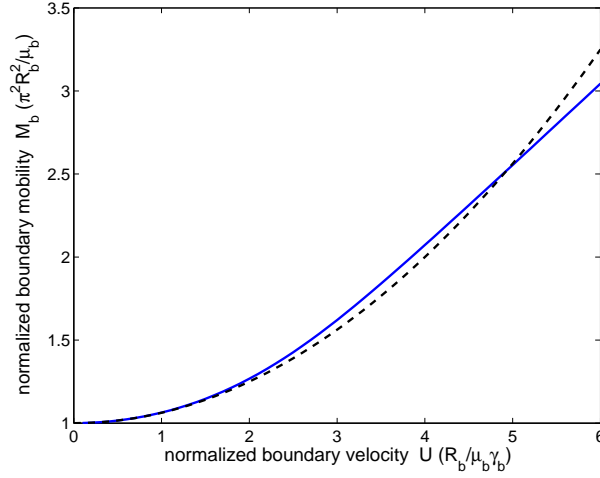


Figure 2.8: Global boundary mobility  $M_b$  normalized by  $\mu_b/(\pi R_b^2)$  versus pore velocity  $U$  normalized by  $\mu_b \gamma_b / R_b$ . Dotted line is from Eq. (2.28).

velocity  $U$ . In accord with Eq. (2.24) the ratio  $\mu_b/(\pi R_b^2)$  is considered as the boundary mobility  $M_b$ , we are interested in the system mobility  $M_{\text{sys}}$ .

The pore drag angle  $\Theta_p$  can be related to the pore mobility  $M_p$  via

$$U = M_p K_{\text{pore drag}} = M_p \cdot 2\pi R_p \gamma_b \sin \Theta_p$$

and in the small slope approximation

$$\Theta_p = \frac{U}{2\pi R_p \gamma_b M_p}, \quad (2.29)$$

where specific expressions for  $M_p$  depend on the pore motion mechanism and will be discussed in the two next chapters. The value of  $\Theta_p$  is used as an initial condition for Eq. (2.25), which should be also taken in the small slope approximation, i.e.,

$$\partial_\rho \theta + \frac{1}{\rho} \theta - \epsilon = 0, \quad \theta(\rho)|_{\rho=R_p/R_b} = \Theta_p.$$

The general solution reads

$$\theta(\rho) = \frac{\epsilon \rho}{2} + \frac{C}{\rho},$$

where the integration constant  $C$  is determined through the initial condition and reads

$$C = \Theta_p \frac{R_p}{R_b} - \frac{\epsilon R_p^2}{2 R_b^2}.$$

Therefore the boundary drag angle is

$$\Theta_b = \theta(1) = \Theta_p \frac{R_p}{R_b} + \frac{\epsilon}{2} \left( 1 - \frac{R_p^2}{R_b^2} \right)$$

and using Eq. (2.26) and (2.29) we see that the boundary drag angle is also proportional to the common velocity

$$\Theta_b = \frac{U}{2\pi R_b \gamma_b M_p} + \frac{U R_b}{2\mu_b \gamma_b} \left( 1 - \frac{R_p^2}{R_b^2} \right).$$

With this value one can calculate the boundary drag force

$$K_{\text{boundary drag}} = 2\pi R_b \gamma_b \sin \Theta_b \approx 2\pi R_b \gamma_b \Theta_b$$

and the system mobility

$$M_{\text{sys}} = \frac{U}{2\pi R_b \gamma_b \Theta_b}.$$

The result reads

$$M_{\text{sys}} = \left[ \frac{1}{M_p} + \frac{\pi(R_b^2 - R_p^2)}{\mu_b} \right]^{-1} \quad (2.30)$$

and quantifies the change in the boundary mobility. One interesting limiting case exists for large  $M_p$ , i.e.,

$$M_{\text{sys}}(M_p \rightarrow \infty) = \frac{\mu_b}{\pi(R_b^2 - R_p^2)}$$

that should be compared with Eq. (2.24). As we see, the system mobility increases because the “mobile” pore effectively decreases the boundary area. Another situation occurs for a small pore with negligible area

$$M_{\text{sys}}(R_p \ll R_b) = \left( \frac{1}{M_p} + \frac{1}{M_b} \right)^{-1},$$

where  $\mu_b/(\pi R_b^2)$  is replaced by  $M_b$ . We see that the inverse system mobility equals inverse pore mobility plus inverse boundary mobility. For  $N$  dragged pores the latter equation must be rewritten

$$M_{\text{sys}}(N \text{ pores}, R_p \ll R_b) = \left( \frac{N}{M_p} + \frac{1}{M_b} \right)^{-1}$$

and is identical to the well known result [Nichols, 1968]. If, however, the area covered by pores cannot be neglected, the system mobility must be derived from the more general Eq. (2.30). The result reads

$$M_{\text{sys}} = \left( \frac{N}{M_p} + (1 - \eta) \frac{1}{M_b} \right)^{-1}. \quad (2.31)$$

The dimensionless factor

$$\eta = \frac{NR_p^2}{R_b^2} < 1$$

shows what part of the boundary area is covered with pores. If the first term on the right hand side of Eq. (2.31) dominates, the dragged pores control the boundary motion [Brook, 1969].

## 2.4 Boundary motion in two dimensions

The above considered boundaries are two-dimensional objects, i.e., geometrical surfaces with radial symmetry embedded in the three-dimensional coordinate space. In this section we consider one-dimensional curves embedded in the two-dimensional coordinate space. To do so one should imagine a real two-dimensional boundary that is parallel to the  $OY$  axis and considerably extended in this direction. The corresponding space scale is denoted by  $L_b$  and is much larger than the spatial scales characteristic for the pore's cross-section completely described in the  $XOZ$  plane. Correspondingly, the general boundary equation  $z = f(x, y, t)$  is replaced by  $z = f(x, t)$ . This leads to considerable simplifications and even exact solutions for many problems. From the geometrical point of view either the implicit  $\mathcal{F}(x, z, t) = 0$  or the explicit  $z = f(x, t)$  boundary equation describes a moving curve in the two-dimensional  $XOZ$  space.

### 2.4.1 Basic equations

First of all, one of the principal curvatures is now equal to zero. The mean curvature equals the second principal curvature and is given by

$$\kappa = \partial_x \left( \frac{\partial_x f}{\sqrt{1 + (\partial_x f)^2}} \right) = \frac{\partial_x^2 f}{[1 + (\partial_x f)^2]^{3/2}} \quad (2.32)$$

as follows from Eq. (2.13). The basic Eq. (2.14) is then replaced by a much simpler equation

$$\partial_t f = \mu_b \gamma_b \frac{\partial_x^2 f}{1 + (\partial_x f)^2}, \quad (2.33)$$

which nevertheless, is still a nonlinear partial differential equation. For the boundary motion it was first introduced in [Mullins, 1957] for a grooving problem that naturally has a two-dimensional geometry. The new set of stationary solutions is given by a simple linear condition  $\partial_x^2 f = 0$  so that  $z$  is a linear function of  $x$  and each equilibrium solution is a straight line. In other words, all minimal surfaces are now trivial (planes). For the uniform boundary motion one should use

$$f(x, t) = F(x) + Ut, \quad (2.34)$$

which replaces Eq. (2.20). It follows that

$$\frac{\partial_x^2 F}{1 + (\partial_x F)^2} - \frac{U}{\mu_b \gamma_b} = 0. \quad (2.35)$$

The latter equation is much simpler than Eq. (2.22) and can be immediately integrated. Note, that the equation invariance with respect to translations  $F \rightarrow F + \text{const}$  still holds. Therefore, without loss of generality we can assume  $F(0) = 0$ . If, as in the previous section, we also accept that  $\partial_x F(0) = 0$ , the exact analytical solution of Eq. (2.35) reads (see also Fig. 2.9)

$$F(x) = \frac{\mu_b \gamma_b}{U} \ln \left( \cos \frac{Ux}{\mu_b \gamma_b} \right)^{-1}. \quad (2.36)$$

It presents a cylindrical boundary in 3D space for  $-R_b < x < R_b$ . Note, that the  $z$  dimension of the boundary is given by the expression

$$F(R_b) = \frac{\mu_b \gamma_b}{U} \ln \left( \cos \frac{UR_b}{\mu_b \gamma_b} \right)^{-1},$$

which gradually increases with the increase of  $U$ . This dimension formally becomes infinite for  $UR_b/(\mu_b \gamma_b) = \pi/2$ . Therefore a uniform motion of a cylindrical boundary is possible only below the critical velocity

$$U < U_{\max} = \frac{\pi \mu_b \gamma_b}{2R_b}. \quad (2.37)$$

Concerning boundary mobility we note that the driving force is now  $K_{\text{drag}} = 2L_b \gamma_b \sin \Theta_b$ . The local slope depends linearly on the  $x$  coordinate

$$\theta = \arctan \partial_x F = \frac{Ux}{\mu_b \gamma_b}$$

and therefore the drag angle for the boundary reads

$$\Theta_b = \theta(R_b) = \frac{UR_b}{\mu_b \gamma_b}. \quad (2.38)$$

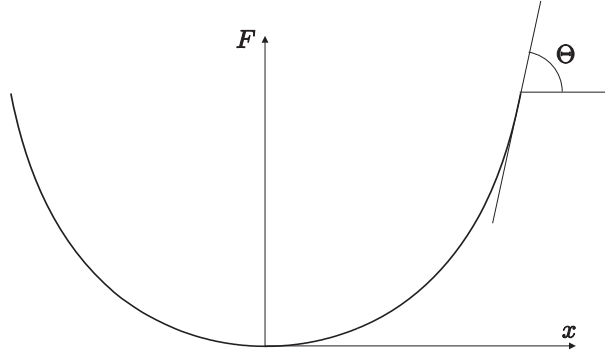


Figure 2.9: Cross-section of a uniformly moving cylindrical boundary  $z = F(x)$ , as given by Eq. (2.36).

The latter ratio was referred to as  $\epsilon$  in the previous section. Equation (2.27) is now simply  $\Theta_b(\epsilon) = \epsilon$ . Defining the global boundary mobility as a ratio of the velocity and the drag force we obtain

$$M_b(\epsilon) = \frac{U}{K_{\text{drag}}} = \frac{\mu_b}{2L_b R_b} \frac{\epsilon}{\sin \epsilon} = \frac{\mu_b}{2L_b R_b} \left( 1 + \frac{\epsilon^2}{6} + \dots \right). \quad (2.39)$$

This equation should be compared with Eq. (2.28). In Eqs. (2.28) and (2.39) the global mobility depends on  $\epsilon$  (i.e., on the boundary velocity) indicating nonlinearity of the problem. In the small slope approximation one can ignore  $\epsilon$  and obtains

$$M_b = \frac{\mu_b}{2L_b R_b} \quad (2.40)$$

in analogy with Eq. (2.24). In Eqs. (2.24) and (2.40) the global mobility equals the local one divided through the boundary area, this representation is generic in the small slope approximation.

Finally in full analogy with the previous section one can quantify mobility of a pore-boundary system for a channel-like pore. The result reads

$$M_{\text{sys}} = \frac{1}{\frac{1}{M_p} + \frac{2L_b(R_b - R_p)}{\mu_b}} \quad (2.41)$$

and is similar to Eq. (2.30). Here  $L_b = L_p$ . Equation (2.31) still applies for  $N$  dragged pores.

## 2.4.2 Exact results

To conclude the discussion of the boundary motion in two dimensions let us consider an exact result that was found by von Neumann and Mullins

[Neumann, 1952, Mullins, 1956]. Exact solutions play an important role as benchmarks for numerical schemes. In addition they help us to develop physical intuition, and they serve as a starting point for different perturbation schemes. To begin the discussion let us consider a part  $a \leq x \leq b$  of a two-dimensional boundary  $z = f(x, t)$  that is moving, e.g., up in accord with Eq. (2.33). We ask: at which rate does the volume  $V(t)$  of the grain in question increase? This rate is given by the integral

$$\frac{dV}{dt} = L_b \frac{d}{dt} \int_a^b f(x, t) dx,$$

which can be calculated *exactly*, if we take the time derivative before integration and use Eq. (2.33). The result reads

$$\frac{dV}{dt} = L_b \mu_b \gamma_b (\arctan \partial_x f) \Big|_{x=a}^{x=b}. \quad (2.42)$$

The latter expression is the difference between the slope angles for our boundary. One immediate application is for a symmetrical boundary with  $-R_b < x < R_b$  and equal drag angles  $\Theta_b$ . We have

$$\frac{dV}{dt} = 2L_b \mu_b \gamma_b \Theta_b. \quad (2.43)$$

For the uniform motion with the velocity  $U$  we have  $dV/dt = 2R_b L_b U$  and Eq. (2.43) reduces to Eq. (2.38). We see that if the drag angles are fixed, the grain volume always increases with the same rate as for the partial exact solution given by Eq. (2.36).

Another application is to use Eq. (2.42) for a smooth closed boundary. In this case the difference on the right-hand-side of Eq. (2.42) is equal to  $-2\pi$  and we have

$$\frac{dV}{dt} = -2\pi L_b \mu_b \gamma_b,$$

the latter equation can be directly integrated. The volume of our collapsing cylindrical grain is given by the simple exact expression

$$V(t) = V(0) - 2\pi L_b \mu_b \gamma_b t. \quad (2.44)$$

Equation (2.44) is a natural generalization of Eq. (2.4). We see that the collapse occurs at the moment  $t_c = V(0)/(2\pi L_b \mu_b \gamma_b)$  for any cylindrical grain.

A further application is a cylindrical grain surrounded by  $N$  other grains, where we encounter  $N$  boundaries connected via  $N$  triple junctions. If we

integrate along the grain boundaries, the tangent vector makes a smooth rotation (changes its direction over an angle of  $-2\pi$ ) as above, but  $N$  sudden changes of  $2\pi/3$  occur at each triple junction. Therefore the volume of the grain is changing in accord with

$$\frac{dV}{dt} = - \left( 2\pi - N \frac{2\pi}{3} \right) L_b \mu_b \gamma_b.$$

One consequence is that a pentagonal grain collapses six times slower than a smooth cylindrical grain. A hexagonal  $N = 6$  grain does not change its volume at all, the only way to reduce the surface energy for such a grain is to straighten its boundaries and to form a proper hexagon with straight edges. If the number of surrounding triple junctions is more than six, the grain grows instead of collapsing, this is a classical result of Mullins [*Mullins*, 1956] and von Neumann [*Neumann*, 1952].



## Chapter 3

# Pore motion controlled by surface diffusion

In this chapter we discuss pore motion via the surface diffusion mechanism. The main questions to be addressed are (a) pore mobility calculation and (b) conditions for the pore drag and drop. A typical example is a gas filled pore. It is assumed that the surface diffusion dominates over evaporation-condensation. In contrast to the Zener drag case, both the pore shape and the pore velocity are calculated self-consistently for a given drag angle and arbitrary dihedral angles.

In this chapter, calculations are made for cylindrical channel-like pores, the latter can be completely described by their cross-sections, i.e., in two spatial dimensions. In contrast to lenticular pores (see Introduction and Fig. 3.1b), channel-like pores are not frequently encountered. Nevertheless, close analysis of the experimental data presented in Fig. 3.1a,c,d (see [Renner *et al.*, 2002b] for details of the procedure) shows that elongated channel-like pores also exist in nature. Another situation where the pores can be considered as two-dimensional objects is grain growth in a thin film [Gottstein and Shvindlerman, 1999, Huang *et al.*, 2004, Jankowski and Hayes, 2004]. On the other hand, mathematical description of two-dimensional objects is relatively simple. Mention was made that there is a wide scatter of the published data on lenticular pores. Therefore a careful investigation of a more simple case is also a useful guideline for interpretation of these contradictory results. In particular, our calculations indicate that dependence of the critical velocity on the drag angle is relatively weak in agreement with results of [Yu and Suo, 1999] but in conflict with [Hsueh *et al.*, 1982, Spears and Evans, 1982] and [Svoboda and Riedel, 1992, Riedel and Svoboda, 1993].

Another situation we have to consider is a pore that is filled with a fluid.

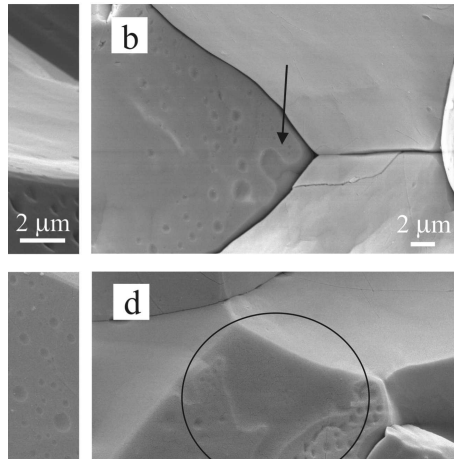


Figure 3.1: SEM microphotograph of a synthetic marble (pure  $\text{CaCO}_3$  hot-pressed at 973 K and 300 MPa confining pressure, showing features associated with pore channels along grain edges. (a) View onto flattened grain edges forming parts of the surface of an elongated channel. (b) Pore (arrow) with a shape typical for drag close to critical conditions, i.e., approaching drop, originating at a grain edge channel. (c) The elongated groove (arrow) may have resulted from drop of a substantial part of the grain boundary edge channel now situated to the left. (d) The depression of the grain face (encircled area) possibly documents drag of a grain boundary channel. The preponderance of lenticular pores in the wake of the channels suggests a generic relation between channels and pores.

In this case the matrix material that dissolves on the leading face of the pore and then crystallizes (precipitates) on the trailing face is effectively transferred across the pore by diffusion through the pore-filling fluid. This mode of mass transfer is considered in the next chapter.

### 3.1 Physical mechanism

From the physical point of view, surface diffusion results from two basic effects: (i) atoms can effectively move along the surface of a phase; (ii) the chemical potential of an atom on the surface of a phase is related to the curvature of the latter. A nonuniform curvature results then in an atomic flux, which tends to make the curvature uniform. For instance, a non-rigid inclusion inside the matrix must evolve to a sphere. The inclusion at the

boundary between two grains has the same tendency. The perfect sphere can, however, not be formed, because boundary conditions have to be satisfied, where the pore branches meet the boundary. For a pore at a stationary boundary we have two segments of a sphere, branching off at either side of the boundary. The two spherical segments adjust themselves to form the correct dihedral angle at the junction with the grain boundary. The dihedral angle is determined by the force balance among the two spherical segments of the pore and the grain boundary [Eq. (3.20)]. When the boundary moves, the geometry of the pore changes self-consistently.

To describe surface diffusion mathematically we have to know the diffusivity of the atoms on the surface of the pore. It will be denoted  $D_s$ . As usual, the corresponding atomic mobility reads  $D_s/(kT)$ . To proceed we have to find an expression for the chemical potential.

Let the chemical potential of an atom on a flat surface be  $\mathbf{m}_0$ . The chemical potential of the atoms on a curved pore surface  $\mathbf{m}_s$  reads [Mullins, 1957]

$$\mathbf{m}_s(\kappa) = \mathbf{m}_0 - \gamma_s \Omega \kappa \quad (3.1)$$

where as in Chapter 2 the quantity  $\kappa = \kappa_1 + \kappa_2$  is the mean curvature of the pore surface.

Henceforth we use the following notations. The equations

$$\mathcal{F}(x, y, z, t) = 0 \quad \Leftrightarrow \quad z = f(x, y, t)$$

as introduced in Eq. (2.10) always refer to the interface between two grains of the same phase (grain boundary). The interface between a pore and a grain (pore surface) is given by

$$\mathcal{G}(x, y, z, t) = 0 \quad \Leftrightarrow \quad z = g(x, y, t) \quad (3.2)$$

and the grain is specified by the inequality  $z < g(x, y, t)$ , i.e., it is positioned “bellow” the pore in a local coordinate frame. The mean surface curvature is defined by Eq. (2.13) where  $f$  is replaced by  $g$ . It is positive if the grain is concave with respect to the pore surface and negative otherwise.

Note that if the curvature is nonuniform, there is a force that acts on each atom and reads  $-\nabla_s \mathbf{m}_s$ . The atoms move parallel to  $\nabla_s \kappa$ , where the gradient  $\nabla_s$  is calculated on the surface.

The mean velocity of an atom reads

$$\mathbf{v}_a = -\frac{D_s}{kT} \nabla_s \mathbf{m}_s.$$

The number of atoms involved in motion per unit area of the surface reads  $\nu = \delta/\Omega$  where  $\delta$  is an effective width of the surface and  $\Omega$  is the volume per

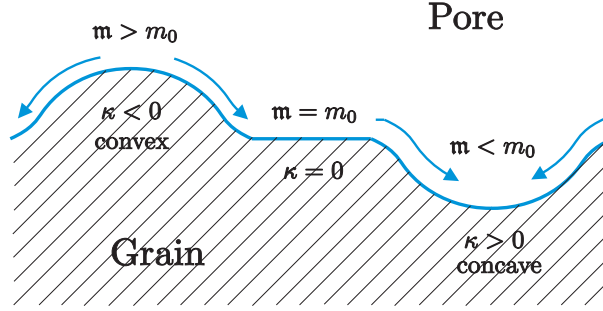


Figure 3.2: Matrix atoms move along the surface towards lower chemical potential.

atom. The resulting atomic flux over the surface reads

$$\mathbf{J}_a = \nu \mathbf{v}_a = -\frac{D_s \delta}{kT \Omega} \nabla_s \mathbf{m}_s,$$

and a unit area of the surface obtains  $-\text{div}_s \mathbf{J}_a$  atoms per second. The corresponding normal velocity of the surface reads

$$v_n = -\Omega \text{div}_s \mathbf{J}_a = \frac{D_s \delta}{kT} \nabla_s^2 \mathbf{m}_s = -\frac{D_s \gamma_s \Omega \delta}{kT} \nabla_s^2 \kappa,$$

where the laplace operator  $\nabla_s^2$  is calculated on the surface. These expressions may be substituted in the general dynamic equation

$$\partial_t g = v_n \sqrt{1 + |\nabla g|^2}, \quad (3.3)$$

which is valid for any moving surface and is derived for  $g(x, y, t)$  exactly like Eq. (2.12) for  $f(x, y, t)$ . The result reads

$$\partial_t g + \frac{D_s \gamma_s \Omega \delta}{kT} \sqrt{1 + |\nabla g|^2} \cdot \nabla_s^2 \kappa = 0,$$

where we still have to derive an explicit expression for  $\nabla_s^2 \kappa$ .

Note, that  $x$  and  $y$  provide us with a local coordinate system on the surface  $z = g(x, y, t)$ . However, the lines on the surface with either  $x = \text{const}$  or  $y = \text{const}$  are not orthogonal to each other and a general expression for the surface Laplace operator  $\nabla_s^2$  should be used instead of the familiar  $\nabla^2 = \partial_x^2 + \partial_y^2$ . Such an expression can be found in textbooks on differential geometry [Dubrovin *et al.*, 1992] and reads

$$\nabla_s^2 \kappa = \frac{1}{\sqrt{1 + |\nabla g|^2}} \text{div} \left( \frac{\nabla \kappa}{\sqrt{1 + |\nabla g|^2}} \right).$$

We can now formulate the main result of this section and arrive at the starting point for the entire chapter. The evolution of the interface between the pore given by  $z > g(x, y, t)$  and the grain given by  $z < g(x, y, t)$  is governed by the nonlinear partial differential equation

$$\partial_t g + \frac{D_s \gamma_s \Omega \delta}{kT} \operatorname{div} \left( \frac{\nabla \kappa}{\sqrt{1 + |\nabla g|^2}} \right) = 0, \quad (3.4)$$

where the mean curvature of the surface is calculated as

$$\kappa = \operatorname{div} \left( \frac{\nabla g}{\sqrt{1 + |\nabla g|^2}} \right). \quad (3.5)$$

This basic equation was first introduced by Mullins for a similar problem of groove evolution along a boundary between two grains, which were in contact with an aqueous phase [Mullins, 1957]. It was solved using a small slope approximation, which as we will see is not sufficient to treat pore detachment. The appropriate solutions of Eq. (3.4) are discussed in the remainder of this chapter.

## 3.2 General properties of the basic equation

Equation (3.4) provides the basis for the description of pore motion. It can be given in a closed form

$$\partial_t g + \frac{D_s \gamma_s \Omega \delta}{kT} \operatorname{div} \left\{ \frac{1}{\sqrt{1 + |\nabla g|^2}} \nabla \left[ \operatorname{div} \left( \frac{\nabla g}{\sqrt{1 + |\nabla g|^2}} \right) \right] \right\} = 0. \quad (3.6)$$

Its general properties are discussed below.

### 3.2.1 Analysis of dimensions

It is worth to note that all physical characteristics of the pore are gathered in a single combination with the dimension

$$\left[ \frac{D_s \gamma_s \Omega \delta}{kT} \right] = \frac{\text{length}^4}{\text{time}}.$$

For example, if the pore between the boundaries can be characterized by a single length parameter  $R_p$  and moves with the constant velocity  $U$ , its behavior depends only on two dimensionless parameters, one is

$$\frac{D_s \gamma_s \Omega \delta}{U R_p^3 kT}$$

and the second is the dihedral angle. For a fluid filled pore with a self-organized shape and a fixed volume  $\mathcal{V}$  the corresponding dimensionless combination reads

$$\frac{D_s \gamma_s \Omega \delta}{U \mathcal{V} k T},$$

and the critical velocity must be proportional to the inverse volume.

### 3.2.2 Stationary solutions

Stationary solutions for the pore-boundary interface are given by the nonlinear partial differential equation

$$\kappa = \operatorname{div} \left( \frac{\nabla g}{\sqrt{1 + |\nabla g|^2}} \right) = \text{const}, \quad (3.7)$$

that is, from the geometrical point of view the stationary solutions are surfaces with constant curvature. The simplest example is provided by a plane, where  $g(x, y)$  is a linear function of  $x$  and  $y$ , therefore  $\nabla g$  is a constant vector and  $\kappa = 0$ . More generally, any minimal surface, i.e., that with the zero mean curvature, provides a solution of Eq. (3.7). Such minimal surfaces were discussed in Chapter I.

Another simple analytic example [Dubrovin *et al.*, 1992] is a rotationally symmetric pore surface with  $g = g(r)$  where  $r = \sqrt{x^2 + y^2}$ . In this case the mean curvature is given by Eq. (2.17) and Eq. (3.7) reduces to an ordinary differential equation

$$\frac{1}{r} \frac{\partial}{\partial r} \left( \frac{r \partial_r g}{\sqrt{1 + (\partial_r g)^2}} \right) = \pm \frac{2}{r_0}$$

with  $r_0 = \text{const}$ . Here,  $\pm 2/r_0$  represents the right-hand-side of Eq. (3.7) for concave and convex surfaces, respectively. After one integration we get

$$\frac{r \partial_r g}{\sqrt{1 + (\partial_r g)^2}} = \pm \frac{r^2}{r_0} + C,$$

where taking  $r \rightarrow 0$  we see that for a regular solution the integration constant  $C = 0$  and

$$\frac{\partial_r g}{\sqrt{1 + (\partial_r g)^2}} = \pm \frac{r}{r_0}.$$

The latter equation can be directly integrated. The solution reads

$$g(r) = \mp \sqrt{r_0^2 - r^2} \quad \text{or} \quad x^2 + y^2 + z^2 = r_0^2$$

and represents a sphere or a spherical segment. Later on we will construct stationary pores on the boundary and at the triple junction as combinations of spherical (cylindrical) segments.

### 3.2.3 Small slope approximation

In this approximation one assumes that  $\nabla g$  is small and ignores the terms proportional to  $|\nabla g|^2$ . In this case the basic Eq. (3.4) reads

$$\partial_t g + \frac{D_s \gamma_s \Omega \delta}{kT} \nabla^2 (\nabla^2 g) = 0 \quad (3.8)$$

and is recognized as a bi-Laplace equation. Considering a plane wave solution of the form

$$g = \text{const} + a(t) \exp(i\mathbf{k}\mathbf{r})$$

we see that

$$\dot{a} = -\frac{D_s \gamma_s \Omega \delta \mathbf{k}^4}{kT} a$$

and therefore the perturbation quickly decays with time and a stationary plane solution  $g(x, y) = \text{const}$  is stable. In other words, an initial perturbation with a characteristic space scale  $\mathfrak{R}$  disappears on a time scale  $\mathfrak{R}^4 kT / (D_s \gamma_s \Omega \delta)$ . One can use this result to obtain a simple estimate of the critical pore velocity. Indeed, let us assume that a pore with the characteristic radius  $R_p$  is subject to uniform motion with the constant velocity  $U$  induced by boundary motion. The characteristic time scale is  $R_p / U$  and the pore should have enough time to adjust itself to perturbations that permanently result from the moving boundaries. Therefore

$$\frac{R_p^4 kT}{D_s \gamma_s \Omega \delta} < \frac{R_p}{U}$$

and

$$U < \frac{D_s \gamma_s \Omega \delta}{R_p^3 kT}.$$

One can then assume that the maximum (critical) pore velocity is given by the expression

$$U_{\max} = C \frac{D_s \gamma_s \Omega \delta}{R_p^3 kT}, \quad (3.9)$$

where the unknown factor  $C(\Phi) \sim 1$  depends on the dihedral angle  $\Phi$ . This result also follows directly from the dimension analysis.

### 3.2.4 Semi-scale solution

One can directly check that the basic Eq. (3.6) allows a partial solution of the form

$$g(x, y, t) = \sqrt[4]{t} \mathbf{g}(\xi), \quad \xi = \frac{r}{\sqrt[4]{t}}, \quad (3.10)$$

where  $\mathbf{g}(\xi)$  is subject to an ordinary differential equation. This special solution can be derived from the symmetry properties following, e.g., [Sedov, 1959]. Indeed, the basic Eq. (3.6) is invariant under a specially chosen scaling transformation. Namely, if  $g(x, y, t)$  is a valid solution of Eq. (3.6), one can build a new valid solution

$$g_\lambda(x, y, t) = \frac{g(\lambda x, \lambda y, \lambda^4 t)}{\lambda}$$

for any constant  $\lambda$ . One can now look for a partial solution that is invariant (does not change) under the scaling transformation. It should have the form given by Eq. (3.10), because in this case  $g_\lambda(x, y, t)$  is identical to  $g(x, y, t)$ . Such a solution is referred to as a semi-scale solution. It is easy to see that  $\mathbf{g}(\xi)$  indeed is subject to an ordinary differential equation, the latter is much more tractable than the partial differential equations. Under the small slope approximation the corresponding solution for  $\mathbf{g}(\xi)$  was solved by Mullins [Mullins, 1957]; for the general nonlinear case its solution is not known. One important conclusion can, however, be drawn from the very form of Eq. (3.10). First of all, the full set of the semi-scale solutions is given by a more general expression

$$g(x, y, t) = \sqrt[4]{\pm(t - t_0)} \mathbf{g} \left( \frac{r}{\sqrt[4]{\pm(t - t_0)}} \right),$$

where  $t_0$  is an arbitrary constant. In other words, there are solutions that are defined either only for  $t > t_0$  or only for  $t < t_0$ . The latter case corresponds to a collapsing singular solution, e.g., the pore can be divided in two parts or separated from the boundary.

### 3.2.5 Two-dimensional case

Imagine an elongated channel-like pore that can be formally assumed to be infinite in  $y$  direction and therefore specified by the equation  $z = g(x, t)$ . One of the principal curvatures is zero, the other is defined by an equation similar to Eq. (2.32)

$$\kappa = \partial_x \left( \frac{\partial_x g}{\sqrt{1 + (\partial_x g)^2}} \right) = \frac{\partial_x^2 g}{[1 + (\partial_x g)^2]^{3/2}}, \quad (3.11)$$



and the basic Eq. (3.4) takes the form

$$\partial_t g + \frac{D_s \gamma_s \Omega \delta}{kT} \partial_x \left( \frac{1}{\sqrt{1 + (\partial_x g)^2}} \partial_x \left\{ \frac{\partial_x^2 g}{[1 + (\partial_x g)^2]^{3/2}} \right\} \right) = 0. \quad (3.12)$$

This equation provides the base for what follows in this chapter and is used to consider the drag and drop problem for channel-like pores. First, we omit  $\partial_t g$  for the stationary solutions and Eq. (3.12) can be integrated

$$\frac{1}{\sqrt{1 + (\partial_x g)^2}} \partial_x \left\{ \frac{\partial_x^2 g}{[1 + (\partial_x g)^2]^{3/2}} \right\} = C, \quad (3.13)$$

where  $C$  is the constant of integration. As in the previous chapter we restrict ourselves to the symmetric solutions such that  $g(-x) = g(x)$ . Symmetry requires  $C = 0$  because the left-hand-side of Eq. (3.13) changes its sign after transformation  $x \rightarrow -x$ , whereas the right-hand-side is not affected. Equation (3.13) can then be integrated once again to obtain

$$\frac{\partial_x^2 g}{[1 + (\partial_x g)^2]^{3/2}} = \pm \frac{1}{r_0}, \quad r_0 = \text{const.}$$

For  $r_0 = \infty$  the solution is a straight line, otherwise it is segment of a circle. Let us introduce an angle variable  $\varphi$  such that

$$\tan \varphi = \partial_x g. \quad (3.14)$$

Symmetry requires that  $\varphi(0) = 0$ . In geometrical terms Eq. (3.14) indicates that  $\varphi$  is the angle between the tangent vector to the pore surface  $z = g(x)$  and  $OX$  axis. Changing variables from  $g$  to  $\varphi$  we obtain

$$\cos \varphi \partial_x \varphi = \pm \frac{1}{r_0} \Rightarrow \sin \phi = \pm \frac{x}{r_0}$$

and therefore

$$\partial_x g = \pm \frac{x}{\sqrt{r_0^2 - x^2}} \Rightarrow g(x) = \mp \sqrt{r_0^2 - x^2}.$$

The solution in question is therefore a segment of a circle, the segment is convex or concave with respect to the underlying grain  $z < g(x)$ . Two such segments can be used to construct an equilibrium solution for a channel-like pore between two grains, as shown in Fig. 3.3.

In a next step let us consider a pore moving uniformly parallel to the  $\hat{z}$  axis with velocity  $U$  identical to the velocity of the grain boundary. The pore

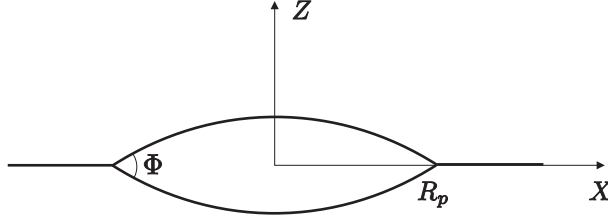


Figure 3.3: Stationary equilibrium pore between two grains. The pore is symmetrical and positioned in a region  $|x| \leq R_p$ . The pore width  $2R_p$  together with the dihedral angle  $\Phi$  uniquely determine the geometry of the pore.

is positioned between two grains and the functional dependence  $z = g(x, t)$  describes the interface between the pore and the bottom boundary. For the uniform motion

$$g(x, t) = Ut + G(x). \quad (3.15)$$

Substituting this pore surface function into Eq. (3.12) and integrating we arrive at

$$Ux + \frac{D_s \gamma_s \Omega \delta}{kT} \frac{1}{\sqrt{1 + (\partial_x G)^2}} \partial_x \left\{ \frac{\partial_x^2 G}{[1 + (\partial_x G)^2]^{3/2}} \right\} = C, \quad (3.16)$$

where  $C$  denotes the constant of integration. As above, considerable simplifications can be achieved, if we restrict ourselves to symmetric solutions  $G(-x) = G(x)$  in which case  $C = 0$ .

To determine the problem completely, we have to formulate boundary conditions involving curvature and dihedral angle. We explicitly give these for the left tip. The conditions on the right side are analogous owing to symmetry. The boundary conditions can be treated in a more natural way if Eq. (3.16) is rewritten for  $C = 0$  as a system of three first order equations

$$\partial_x \varphi = \frac{\kappa}{\cos \varphi}, \quad (3.17)$$

$$\partial_x G = \tan \varphi, \quad (3.18)$$

$$\partial_x \kappa = -\frac{U kT}{D_s \gamma_s \Omega \delta} \frac{x}{\cos \varphi}, \quad (3.19)$$

where  $\varphi$  is the angle between the tangent vector  $(1, \partial_x G)$  and the  $\hat{x}$  axis as expressed by Eq. (3.18). Equation (3.17) is equivalent to the geometrical definition of the curvature (i.e.,  $\kappa = \partial_s \varphi$ , where  $s$  is the natural parameter, see e.g., [Dubrovin *et al.*, 1992]). Equation (3.19) directly follows from Eq. (3.16).

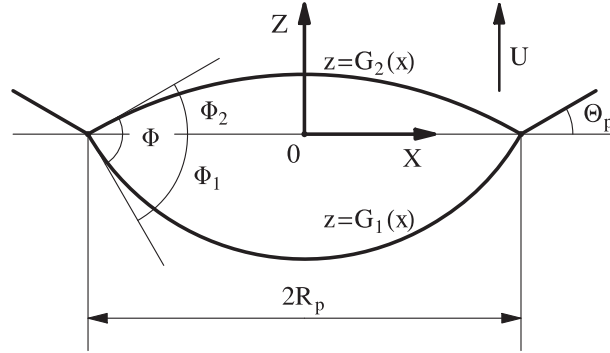


Figure 3.4: Pore that moves upwards with a small constant velocity and therefore is slightly different from that shown in Fig. 3.3.

The moving pore shown in Fig. 3.4 can be considered as a deformation of that shown in Fig. 3.3. It has two branches of total width  $2R_p$ , that is Eqs. (3.17–3.19) must be solved for  $-R_p < x < R_p$ . We index the convex down branch (positive curvature) as the first solution and the convex up branch (negative curvature) as the second. The angles  $\Phi_1$  and  $\Phi_2$  can take different values, but their sum  $\Phi_1 + \Phi_2 = \Phi$  is fixed to the dihedral angle

$$\Phi = 2 \arccos \left( \frac{\gamma_b}{2\gamma_s} \right), \quad (3.20)$$

that is derived from the condition of force equilibrium. Then we have  $\varphi_1(-R_p) = -\Phi_1$  and  $\varphi_2(-R_p) = \Phi_2$  and

$$\varphi_2(-R_p) - \varphi_1(-R_p) = \Phi \quad (3.21)$$

results as the boundary condition for angles on the left tip. Appropriate choice of the coordinate system ensures that

$$G_1(-R_p) = G_2(-R_p) = 0. \quad (3.22)$$

Finally, the chemical potential is proportional to the absolute value of the curvature and has to be continuous at the tip

$$\kappa_1(-R_p) + \kappa_2(-R_p) = 0. \quad (3.23)$$

An important note must be made here. Both pore branches as shown in Fig. 3.4 are concave with respect to the corresponding grains, their curvatures are therefore positive. These curvatures must be calculated in accord with Eq. (3.11) in a corresponding local coordinate frame, i.e.,  $(x, z)$  for the leading

surface and with  $z' = -z$  for the trailing surface. To avoid replication of the actually identical equations for the leading and trailing surfaces we, however, prefer to use only one coordinate frame, therefore  $\kappa_2$  is formally negative. This explains the signs in Eq. (3.23).

Equations (3.17–3.19) together with the symmetry requirement and boundary conditions (3.21–3.23) completely determine the change of the pore shape with variations in its velocity. Similar equations were originally formulated in [Hsueh *et al.*, 1982] for a lenticular pore with rotational symmetry. These equations will be solved analytically and numerically in the next sections both for the pore on the boundary and (after some reformulation) for the pore at the triple junction. Analytical solution is possible in some special cases, e.g., for small velocities or small dihedral angles. The most important property that can be obtained in this way is the mobility of the pore in question. In this case the difference between the equilibrium pore (Fig. 3.3) and the deformed one (Fig. 3.4) is small and a perturbation expansion in pore velocity can be applied. With an increase of the velocity a numerical solutions must be used. This solution is also constructed and the critical velocity of a channel-like pore is obtained.

### 3.3 Pore at a grain boundary

As shown in Section 3.2.1 pore behavior depends on two dimensionless parameters: a dihedral angle  $\Phi$  [defined via ratio of  $\gamma_b$  and  $\gamma_s$  in Eq. (3.20)] and the dimensionless combination

$$u = \frac{UR_p^3 kT}{D_s \gamma_s \Omega \delta} \quad (3.24)$$

that will be referred to as a normalized pore velocity. We also introduce normalized variables

$$\bar{x} = \frac{x}{R_p}, \quad \bar{G} = \frac{G}{R_p}, \quad \bar{\kappa} = R_p \kappa. \quad (3.25)$$

To simplify the notations the bars will henceforth be omitted. The normalized Eq. (3.17) and Eq. (3.19) read

$$\partial_x \varphi = \frac{\kappa}{\cos \varphi}, \quad (3.26)$$

$$\partial_x \kappa = -\frac{ux}{\cos \varphi}, \quad (3.27)$$

and can be solved independently from the third one. These equations are solved for the pore between two grains in this section and for the pore at a

triple junction in the next one. Symmetry reasons allow us to consider only half of the pore, e.g., for  $-1 \leq x \leq 0$ . The normalized left-tip boundary conditions read

$$\varphi_2(-1) - \varphi_1(-1) = \Phi, \quad (3.28)$$

$$\kappa_1(-1) + \kappa_2(-1) = 0, \quad (3.29)$$

as follows from (3.21) and (3.23). Because of the symmetry the conditions for the pore center are

$$\varphi_1(0) = \varphi_2(0) = 0. \quad (3.30)$$

The last two equations replace the boundary conditions at  $x = 1$ . Note, that we have to determine two branches  $\varphi_{1,2}(x)$ ,  $\kappa_{1,2}(x)$  that depend on each other. Therefore four boundary conditions are required. This problem is more complicated than the familiar initial value problem for the ordinary differential equations, and lends itself to solution using a shooting method. The dependence of the solution on parameter  $u$  must be traced. After the solutions for the curvature and the slope angle are found, one can restore the shape of the pore using (normalized) Eq. (3.18)

$$\partial_x G = \tan \varphi, \quad (3.31)$$

with the initial condition

$$G_{1,2}(-1) = 0, \quad (3.32)$$

which replaces Eq. (3.22).

### 3.3.1 Small slope approximation

Here we consider a special case, where an analytical solution of Eqs. (3.28) and (3.29) is available. This happens in the limit

$$\Phi \ll 1 \quad \Leftrightarrow \quad \gamma_b \approx 2\gamma_s, \quad (3.33)$$

i.e., in the small slope approximation as follows from Eq. (3.20).

In principle, small  $\Phi$  does not necessarily demand small  $\phi_{1,2}(x)$ . In particular, the pore can be strongly distorted when its velocity is close to the critical one (see, e.g., numerical solutions below). However, for the equilibrium  $u = 0$  pore (see Fig. 3.3) the slope angles are small together with  $\Phi$ . Therefore one can assume that they stay small at least for the small velocity  $u \ll 1$ . One can then replace  $\cos \varphi$  with 1 and reduce the system (3.28–3.29) to

$$\partial_x \varphi = \kappa, \quad (3.34)$$

$$\partial_x \kappa = -ux, \quad (3.35)$$

the latter equations can be immediately solved. The analytical solutions for the curvature

$$\kappa_1 = \frac{u}{2}(1 - x^2) + \frac{\Phi}{2}, \quad (3.36)$$

$$\kappa_2 = \frac{u}{2}(1 - x^2) - \frac{\Phi}{2}, \quad (3.37)$$

for the slope angle

$$\varphi_1 = \frac{u}{2} \left( x - \frac{x^3}{3} \right) + \frac{\Phi}{2} x, \quad (3.38)$$

$$\varphi_2 = \frac{u}{2} \left( x - \frac{x^3}{3} \right) - \frac{\Phi}{2} x, \quad (3.39)$$

and for the shape of the pore

$$G_1 = \frac{1}{24}(1 - x^2)(ux^2 - 5u - 6\Phi), \quad (3.40)$$

$$G_2 = \frac{1}{24}(1 - x^2)(ux^2 - 5u + 6\Phi), \quad (3.41)$$

are obtained by straightforward integration.

Several interesting conclusions can be derived from this solution. First, the lower branch is concave (with respect to the lower grain) for  $u = 0$  and remains concave for  $u > 0$  [Eq. (3.36)]. The upper grain is also initially concave (with respect to the upper grain), but it changes shape with increasing velocity [Eq. (3.37)]. For  $u > \Phi$  the curvature  $\kappa_2(x)$  changes its sign at the pore center. A slightly deformed pore is illustrated in Fig. 3.5. Similar deformation also occurs in the general case with an arbitrary value of  $\Phi$ .

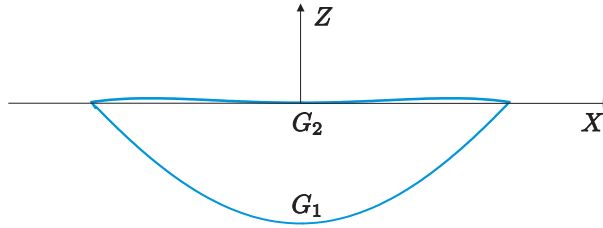


Figure 3.5: Pore shape in the small slope approximation when  $u > \Phi$

Let us now address the pore drag angle  $\Theta_p$  (see Fig. 3.4)

$$\Theta_p = - \left. \frac{\varphi_1(x) + \varphi_2(x)}{2} \right|_{x=-1}. \quad (3.42)$$

It can be explicitly calculated from Eqs. (3.38) and (3.39)

$$\Theta_{\text{p small slope}} = \frac{u}{3} \quad (3.43)$$

and is proportional to the pore velocity. The pore drag is created by the surface tension force that acts on a line of the total length  $2L_p$ , where  $L_p$  is the pore width in  $y$  direction. Therefore

$$K_{\text{pore drag}} = 2L_p\gamma_b \sin \Theta_p \approx \frac{2}{3}L_p\gamma_b u = \frac{4}{3}L_p \frac{UR_p^3 kT}{D_s\Omega\delta}, \quad (3.44)$$

because the small slope limit requires  $\gamma_b/\gamma_s = 2$ . The drag force is also proportional to the pore velocity. One can therefore calculate the mobility of the pore analytically

$$M_{\text{p small slope}} = \frac{U}{K_{\text{pore drag}}} = \frac{3}{4} \frac{D_s\Omega\delta}{kTL_pR_p^3}. \quad (3.45)$$

This expression will later be generalized for an arbitrary value of  $\Phi$ . However, a general structure of mobility of the channel-like pore is already clear

$$M_p = C \frac{D_s\Omega\delta}{kTL_pR_p^3}, \quad (3.46)$$

where an unknown factor  $C = C(\Phi)$  can depend on the dihedral angle.

It is important to note that the analytical solution (3.36–3.41) remains regular with the increase of the pore velocity  $u$  and does not describe the separation of the pore from the moving boundary. In other words, near the critical velocity the values of  $\varphi_{1,2}(x)$  are not small regardless of  $\Phi$ . The separation can be considered only with numerical solutions of the Eqs. (3.26–3.27). Before calculating them let us note that all analytical solutions given by Eqs. (3.36–3.41) have the same structure

$$(\text{quantity}) = (\text{equilibrium value}) + u \cdot (\text{perturbation}). \quad (3.47)$$

One can use this expression to look for an analytical solution of the basic Eqs. (3.26–3.27) for arbitrary values of  $\Phi$  and  $u \ll 1$ . The solution is obtained as a series in  $u$ , i.e., it is valid as long as the normalized pore velocity remains small. In the next section we will derive this solution and use it to determine pore mobility but not the separation criteria. Thereafter, the numerical solution and separation criteria will be obtained.

### 3.3.2 Mobility of a pore at a grain boundary

To make further analytical and numerical calculations for a pore at a boundary and at a triple junction as similar as possible it is convenient to introduce a natural parameter  $s$  for the pore shape. That is, the function  $z = G(x)$  is now determined implicitly by two functions

$$x = x(s) \quad \text{and} \quad z = z(s),$$

with an additional restriction that the tangent vector  $\boldsymbol{\tau} = [x'(s), z'(s)]$  has a unit length and therefore

$$\boldsymbol{\tau} = \begin{pmatrix} \cos \varphi \\ \sin \varphi \end{pmatrix},$$

where we recall that  $\varphi$  was defined as the slope angle for  $\boldsymbol{\tau}$ . The normalized basic Eqs. (3.26), (3.27) and (3.31) are now replaced by four equations

$$\partial_s \varphi = \kappa, \tag{3.48}$$

$$\partial_s \kappa = -ux, \tag{3.49}$$

$$\partial_s x = \cos \varphi, \tag{3.50}$$

$$\partial_s z = \sin \varphi, \tag{3.51}$$

where the first three equations are independent of the last one and can be given in an extremely compact form

$$\partial_s^3 \varphi + u \cos \varphi = 0 \tag{3.52}$$

indicating intrinsic simplicity of formulations which make use of the natural parameter. The only disadvantage is that the integration interval in  $s$  cannot be determined a priori like that in  $x \in [-1, 1]$ . The integration procedure runs, (e.g., from the left tip) before the necessary conditions (e.g., at the right tip) are met.

#### Problem posing

The goal is to calculate mobility of a channel-like pore at a boundary. The pore is formally infinite in  $y$  direction the corresponding large scale is denoted by  $L_p$  and all variables are independent of  $y$ . The system (3.48–3.51) specifies  $\varphi$ ,  $\kappa$ ,  $x$  and  $z$  as functions of the natural parameter  $s$ . These functions have an index 1 or 2 for the lower and upper pore branch, respectively. We have four differential equations that should be solved two times for both branches of the pore. Therefore eight boundary conditions are needed. The pore tips



are positioned at the points  $z = 0$  and  $x = \pm 1$  (normalization). We assume that the left tip corresponds to  $s = 0$ . Therefore we have four conditions

$$x_1(0) = x_2(0) = -1, \quad (3.53)$$

$$z_1(0) = z_2(0) = 0. \quad (3.54)$$

The curvature should be continuous at the tips whereas  $\varphi_1$  and  $\varphi_2$  should combine to provide a predefined dihedral angle  $\Phi$ . Therefore instead of (3.28) and (3.29) we have two additional conditions at the left tip

$$-\varphi_1(0) + \varphi_2(0) = \Phi, \quad (3.55)$$

$$\kappa_1(0) + \kappa_2(0) = 0. \quad (3.56)$$

At some (yet unknown) values of the natural parameters, e.g.,  $s_1^{\max}$  and  $s_2^{\max}$ , the pore branches intersect the  $z$  axis; the latter is the symmetry axis of our solution. Therefore we have four more conditions

$$x_1(s_1^{\max}) = x_2(s_2^{\max}) = 0, \quad (3.57)$$

$$\varphi_1(s_1^{\max}) = \varphi_2(s_2^{\max}) = 0. \quad (3.58)$$

Altogether we have specified ten conditions instead of eight, two extraneous equations are necessary to find two unknowns  $s_{1,2}^{\max}$ . The problem is correctly posed.

### Solution strategy

To obtain the mobility of the pore we have to solve (3.48–3.51), (in fact, only the first three equations) for small values of the normalized velocity  $u$ . The solution should be looked for as a Taylor expansion in  $u$ ; only the first two terms like in Eq. (3.47) are necessary. The solution for  $\varphi_{1,2}(s)$  should then be used to find the pore drag angle (see Eq. (3.42) and Fig. 3.4)

$$\Theta_p = - \left. \frac{\varphi_1(s) + \varphi_2(s)}{2} \right|_{s=0}, \quad (3.59)$$

which is proportional to  $u$ . Actually this is because the drag force is proportional to the resulting pore velocity. Indeed, similar to Eq. (3.44) the drag force is small together with the drag angle and

$$K_{\text{pore drag}} = 2L\gamma_b \sin \Theta_p \approx 2L\gamma_b [\varphi_1(0) + \varphi_2(0)] \quad (3.60)$$

is proportional to  $u$ . This proportionality, if given in physical units, is a proportionality between the drag force and the resulting pore velocity. It provides us with the mobility of the pore. Let us now describe the solution.

### Equilibrium state

In the equilibrium state, that is for  $u = 0$ , the pore is constructed of two equal circle segments with zero drag angle (Fig. 3.3). For zero velocity the curvatures are constant  $\partial_s \kappa_{1,2} = 0$  [Eq. (3.49)], therefore  $\varphi_{1,2}(s)$  and then  $x_{1,2}(s)$  can be found by direct integration. It is convenient to introduce two new parameters

$$\rho = \frac{1}{\sin \Phi/2} \quad (3.61)$$

and

$$s_0 = \frac{\rho \Phi}{2}, \quad (3.62)$$

where  $\rho$  is the common radius of the segments (measured in  $R_p$  units) and  $s_0$  is the normalized half length of the segments. The constant curvatures of the pore branches at equilibrium read

$$\kappa_1 = \frac{1}{\rho} \quad \kappa_2 = -\frac{1}{\rho},$$

and therefore we can directly integrate Eq. (3.48) for  $\partial_s \varphi$  to obtain

$$\varphi_1 = \frac{s - s_1^{\max}}{\rho}, \quad \varphi_2 = -\frac{s - s_2^{\max}}{\rho},$$

where we take into account that  $\varphi_{1,2}(s)$  should disappear for  $s = s_{1,2}^{\max}$  [Eq. (3.58)]. Now we can integrate  $\cos \varphi_{1,2}(s)$  to obtain  $x_{1,2}(s)$  [Eq. (3.50)], i.e.,

$$x_1 = \rho \sin \frac{s - s_1^{\max}}{\rho}, \quad x_2 = \rho \sin \frac{s - s_2^{\max}}{\rho},$$

where we take into account that  $x_{1,2}(s)$  should disappear for  $s = s_{1,2}^{\max}$  [Eq. (3.57)]. Further, considering the set of the above formulated boundary conditions we see that only Eqs. (3.53) and (3.55) are left. These conditions are satisfied if

$$s_1^{\max} = s_0 \quad \text{and} \quad s_2^{\max} = s_0. \quad (3.63)$$

That is, the equilibrium state is completely defined. We now perform the next step of the perturbation theory.

### Perturbation

To quantify the perturbed solution we present all variables as a sum of the equilibrium ones and a small perturbation. This should be done separately

for each pore branch. Therefore,

$$\begin{aligned} \kappa_1 &= \frac{1}{\rho} + \tilde{\kappa}_1 & \kappa_2 &= -\frac{1}{\rho} + \tilde{\kappa}_2 \\ \varphi_1 &= \frac{s - s_0}{\rho} + \tilde{\varphi}_1 & \varphi_2 &= -\frac{s - s_0}{\rho} + \tilde{\varphi}_2 \\ x_1 &= \rho \sin \frac{s - s_0}{\rho} + \tilde{x}_1 & x_2 &= \rho \sin \frac{s - s_0}{\rho} + \tilde{x}_2, \end{aligned}$$

where all perturbations are denoted by tilde and are proportional to  $u$ .

### Reformulation of the boundary conditions

First of all, the perturbed quantities must be substituted into the boundary conditions. In a first step, inserting  $s = 0$  into Eqs. (3.53), (3.55) and (3.56) for the left tip we obtain

$$\tilde{x}_{1,2}(0) = 0, \quad (3.64)$$

$$-\tilde{\varphi}_1(0) + \tilde{\varphi}_2(0) = 0, \quad (3.65)$$

$$\tilde{\kappa}_1(0) + \tilde{\kappa}_2(0) = 0. \quad (3.66)$$

The other boundary conditions involve  $s = s_{1,2}^{\max}$ . They are not so simple because the equilibrium values of  $s_{1,2}^{\max}$  is also perturbed. Therefore we substitute

$$\begin{aligned} s_1^{\max} &= s_0 + \delta_1 \\ s_2^{\max} &= s_0 + \delta_2 \end{aligned}$$

with  $\delta_{1,2} \sim u$  into (3.57) and (3.58), use Taylor expansion in  $\delta$  to obtain

$$\begin{aligned} \delta_1 + \tilde{x}_1(s_0) &= 0, & \delta_1 + \rho \tilde{\varphi}_1(s_0) &= 0, \\ \delta_2 + \tilde{x}_2(s_0) &= 0, & -\delta_2 + \rho \tilde{\varphi}_2(s_0) &= 0. \end{aligned}$$

Fortunately one can eliminate  $\delta_{1,2}$  and write two equations directly for the “old” values of  $s_{1,2}^{\max}$

$$\tilde{x}_1(s_0) - \rho \tilde{\varphi}_1(s_0) = 0, \quad (3.67)$$

$$\tilde{x}_2(s_0) + \rho \tilde{\varphi}_2(s_0) = 0. \quad (3.68)$$

Altogether we have six conditions (3.64–3.68) to specify six integration constants in the further expressions for  $\tilde{\kappa}_{1,2}(s)$ ,  $\tilde{\varphi}_{1,2}(s)$ ,  $\tilde{x}_{1,2}(s)$ .

### Perturbation of the lower branch

We substitute the perturbed expressions for  $\kappa_1(s)$ ,  $\varphi_1(s)$ ,  $x_1(s)$  into our basic system (3.48–3.50) and obtain

$$\begin{aligned}\partial_s \tilde{\kappa}_1 &= -u\rho \sin \frac{s-s_0}{\rho}, \\ \partial_s \tilde{\varphi}_1 &= \tilde{\kappa}_1, \\ \partial_s \tilde{x}_1 &= -\sin \frac{s-s_0}{\rho} \tilde{\varphi}_1,\end{aligned}$$

which is a linear system of ordinary differential equations. It can be directly integrated

$$\begin{aligned}\tilde{\kappa}_1 &= u\rho^2 \cos \frac{s-s_0}{\rho} + C_1, \\ \tilde{\varphi}_1 &= u\rho^3 \sin \frac{s-s_0}{\rho} + C_1(s-s_0) + C_2, \\ \tilde{x}_1 &= -\frac{1}{2}u\rho^3 \left[ (s-s_0) - \frac{\rho}{2} \sin \frac{2(s-s_0)}{\rho} \right] - \\ &\quad C_1\rho^2 \left[ \sin \frac{s-s_0}{\rho} - \frac{s-s_0}{\rho} \cos \frac{s-s_0}{\rho} \right] + \\ &\quad C_2\rho \cos \frac{s-s_0}{\rho} + C_3,\end{aligned}$$

where  $C_{1,2,3}$  are integration constants.

### Perturbation of the upper branch

In a similar way we substitute the perturbed expressions for  $\kappa_2(s)$ ,  $\varphi_2(s)$ ,  $x_2(s)$  in (3.48–3.50) to get

$$\begin{aligned}\partial_s \tilde{\kappa}_2 &= -u\rho \sin \frac{s-s_0}{\rho}, \\ \partial_s \tilde{\varphi}_2 &= \tilde{\kappa}_2, \\ \partial_s \tilde{x}_2 &= \sin \frac{s-s_0}{\rho} \tilde{\varphi}_2,\end{aligned}$$

and therefore

$$\begin{aligned}\tilde{\kappa}_2 &= u\rho^2 \cos \frac{s-s_0}{\rho} + D_1, \\ \tilde{\varphi}_2 &= u\rho^3 \sin \frac{s-s_0}{\rho} + D_1(s-s_0) + D_2, \\ \tilde{x}_2 &= \frac{1}{2}u\rho^3 \left[ (s-s_0) - \frac{\rho}{2} \sin \frac{2(s-s_0)}{\rho} \right] + \\ &D_1\rho^2 \left[ \sin \frac{s-s_0}{\rho} - \frac{s-s_0}{\rho} \cos \frac{s-s_0}{\rho} \right] - \\ &D_2\rho \cos \frac{s-s_0}{\rho} + D_3,\end{aligned}$$

where  $D_{1,2,3}$  are integration constants.

### Mobility

We have six expressions for  $\tilde{\kappa}_{1,2}(s)$ ,  $\tilde{\varphi}_{1,2}(s)$ ,  $\tilde{x}_{1,2}(s)$  with six integration constants  $C_{1,2,3}$  and  $D_{1,2,3}$  and six restrictions (3.64–3.68) to find them. The expressions for the integration constants are rather cumbersome, but they are not of great interest; we are mainly interested in the pore drag angle, which is given by Eq. (3.59), i.e.,

$$\Theta_p = u\rho^2 + \frac{s_0}{2}(C_1 + D_1) - \frac{1}{2}(C_2 + D_2),$$

the resulting expression is very simple

$$\Theta_p = \frac{\Phi - \sin \Phi}{4 \sin^3 \frac{\Phi}{2} \cos \frac{\Phi}{2}} u. \quad (3.69)$$

Correspondingly, the mobility of the pore at a boundary can be calculated based on the discussion that follows Eq. (3.60). The result reads

$$M_p = \frac{\sin^3 \Phi/2}{\Phi - \sin \Phi} \frac{D_s \Omega \delta}{kT L_p R_p^3}, \quad (3.70)$$

where we expressed all quantities in physical units and replaced  $\gamma_b/\gamma_s$  with  $2 \cos \Phi/2$  [Eq. (3.20)]. The dependence of the pore mobility on the surface tension coefficients is completely integrated into the dependence on dihedral angle. The general structure of Eq. (3.70) coincides with the prediction (3.46), the result that follows in the small slope  $\Phi \rightarrow 0$  limit also is in agreement with Eq. (3.45). In general, the mobility decreases with the increase

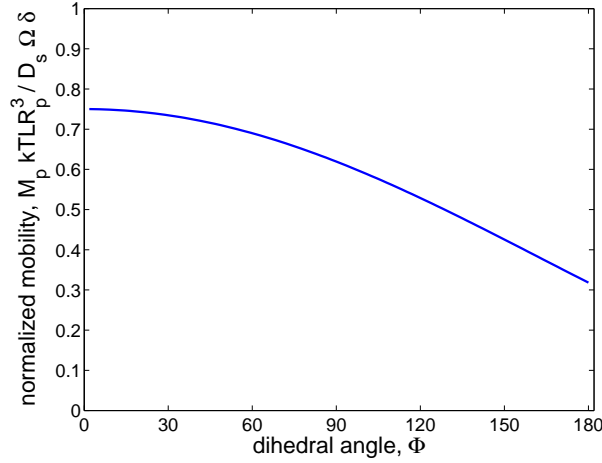


Figure 3.6: Mobility of a channel-like pore normalized in accord with Eq. (3.70) versus dihedral angle.

of the dihedral angle. This dependence is, however, relatively weak, i.e., the numerical factor in Eq. (3.70) changes from  $3/4$  at  $\Phi = 0$  to  $1/\pi$  at  $\Phi = \pi$ . The relation between  $\Phi$  and normalized mobility is illustrated in Fig. 3.6.

An expression similar to Eq. (3.70) was also obtained in a preceding paper [Svoboda and Riedel, 1992] from energy arguments. Our calculation is more cumbersome but has two advantages (a) it can be readily generalized to get further velocity dependent corrections if necessary (b) following our line one can also obtain mobility of a pore at the triple junction (see the next section).

Having in mind possible applications it is also of interest to rewrite Eq. (3.70) in terms of the pore volume. In principle, one should distinguish the equilibrium pore size, say,  $R_{\text{eq}}$  and that (i.e.,  $R_p$ ) of a pore moving with a constant velocity  $U$ . However, for the mobility calculations the pore is only slightly disturbed and the difference between  $R_{\text{eq}}$  and  $R_p$  can be ignored. The volume of the equilibrium pore is given by the expression

$$V_p = \frac{\Phi - \sin \Phi}{\sin^2 \Phi/2} R_p^2 L_p \quad (3.71)$$

and the modified expression (3.70) for the pore mobility reads

$$M_p = \frac{\sin \Phi/2}{R_p} \frac{D_s \Omega \delta}{V_p kT}. \quad (3.72)$$

An even more simple expression can be obtained if one notes that the first factor in Eq. (3.72) is the equilibrium value  $\kappa_{\text{eq}}$  of the pore curvature and

therefore

$$M_p = \frac{D_s \Omega \kappa_{\text{eq}} \delta}{V_p kT}. \quad (3.73)$$

### 3.3.3 Numerical solutions and critical velocities

In this section solutions of Eqs. (3.48–3.51) are sought numerically. For given  $u$  and  $\Phi$ , a shooting method is applied to obtain a two-parametric family of trial pore shapes starting from the left tip by specifying  $\Phi_1$  and  $\kappa_1$  and determining  $\Phi_2$  and  $\kappa_2$  from the boundary conditions (3.55) and (3.56). Each trial solution consists of two branches. The values of  $\Phi_1$  and  $\kappa_1$  are uniquely determined, when we impose the natural restriction that both branches have to join at the right tip, determining the shape of a pore that moves stationary at given  $u$  and  $\Phi$ . The boundary conditions at the right tip are satisfied automatically owing to symmetry.

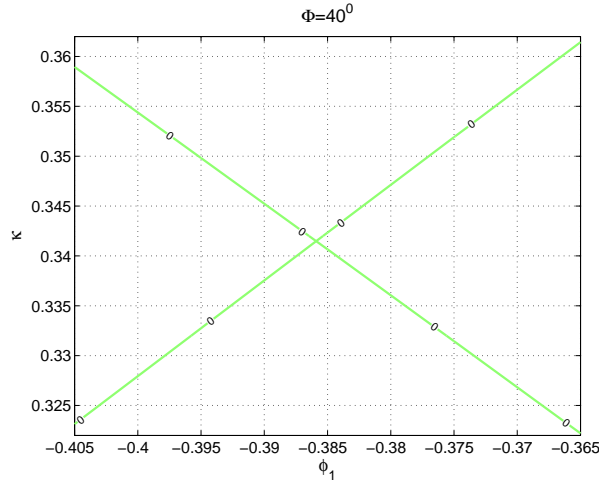


Figure 3.7: Application of a shooting method for  $u = 0.1$  and  $\Phi = 2\pi/9$ . See text for explanation.

A typical calculation is illustrated in Fig. 3.7 obtained for  $u = 0.1$  and  $\Phi = 2\pi/9$ . Each point on the coordinate plane corresponds to a pair of potentially possible initial values (at the left tip) of  $\kappa_1$  and  $\Phi_1$ . Lines indicate suitable choices of  $(\kappa_1, \Phi_1)$  that ensure that the corresponding solution of Eqs. (3.48–3.51) goes through the right tip. There are two such lines one for the trailing and one for the leading pore branch. The intersection point indicates the only possible choice of the initial conditions at which both branches go through the right tip. Now, the pore shape can be completely restored for the given values of  $u$  and  $\Phi$ . One can then change  $u$  and repeat

the whole procedure again. With increasing  $u$ , the pore shape deviates more and more from the stationary shape. This is illustrated in Fig. 3.8.

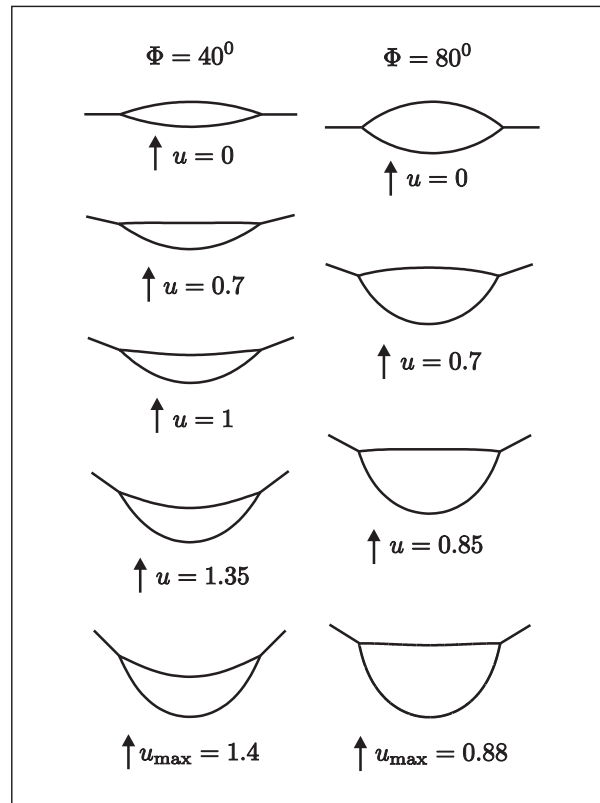


Figure 3.8: Change of pore shape with an increase of the normalized velocity  $u$  for two different dihedral angles. If the velocity exceeds some critical value, no solution exists and the coupled motion of the pore and boundary is not possible.

Using numerical solutions one can trace the relation between the pore drag angle  $\Theta_p$  and the resulting pore velocity  $u$ . One can then compare the numerical result with the analytical prediction given by Eq. (3.69). This is shown in Fig. 3.9. We see that for small values of  $\Theta_p$  its dependence on  $u$  is linear and the correspondence between the theory and numerics is good. In this region the concept of pore mobility can be used. With increasing  $\Theta_p$  the dependence between the drag and resulting velocity becomes nonlinear and out of scope of the analytical considerations. Here, a new nonlinear effect becomes important: the pore can separate from the boundary. In our framework this inevitably happens, when no regular solution of the system (3.48–3.51) exists.



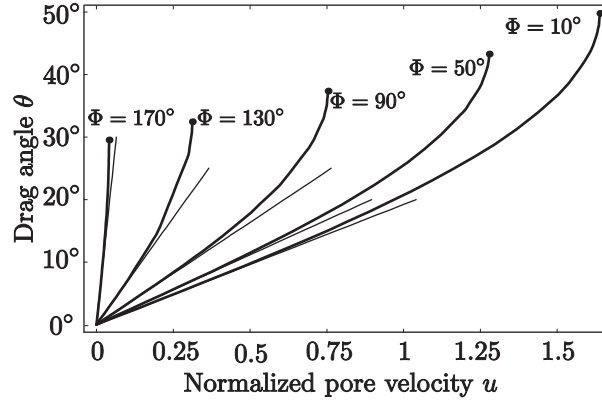


Figure 3.9: Drag angle versus pore velocity as results from Eq. (3.69) (straight lines) and from numerical solutions of Eqs. (3.48–3.51) (curved lines) for five different values of the dihedral angle  $\Phi$ . As long as the drag angle  $\Theta_p$  is small enough the concept of linear mobility applies.

Indeed, above some critical velocity  $u_{\max}$  no numerical solution can be found, i.e., the steady coupled motion of the pore and the boundary exists only in a bounded region  $u < u_{\max}(\Phi)$  of the  $(u, \Phi)$  plane. This region was obtained numerically and is shown in Fig. 3.10. Here, the numerical results are given by points and the solid line is from the analytical expression

$$u_{\max} = (1.75 - 0.44\Phi) \cos \frac{\Phi}{2}, \quad (3.74)$$

which is a good approximation, especially for large dihedral angles. For  $\Phi \rightarrow 0$  the velocity  $u_{\max}$  tends to a finite value, while  $u_{\max} \rightarrow 0$  as  $\Phi \rightarrow \pi$ , i.e., a normalized critical velocity for a channel-like pore vanishes. A vanishing normalized critical velocity was also obtained for a spherical pore [Hsueh *et al.*, 1982] leading to a seemingly correct conclusion that critical pore velocity strongly depends on dihedral angle and that steady-state motion accommodated by surface diffusion is impossible for a pore with  $\Phi \sim \pi$ . In fact, this is not correct. Note, that the normalization that was used to define  $u$  [Eq. (3.24)] also depends on  $\gamma_s$  and therefore changes with  $\Phi$  [Eq. (3.20)]. Before making conclusion on channel-like pores we have to return to physical units to fully reveal the dependence on dihedral angle in Eq. (3.74). By doing this we derive our main result for the grain boundary detachment problem

$$U_{\max} = (0.88 - 0.22\Phi) \frac{D_s \Omega \delta}{kT} \frac{\gamma_b}{R_p^3}. \quad (3.75)$$

This also corresponds to the above obtained estimate (3.9). Notably, the critical velocity for  $\Phi = \pi$  is nonzero. In fact, the dependence of  $U_{\max}$  on the dihedral angle is relatively weak. Similar results were also obtained in a recent investigation of drag and drop of a lenticular pore [Yu and Suo, 1999].

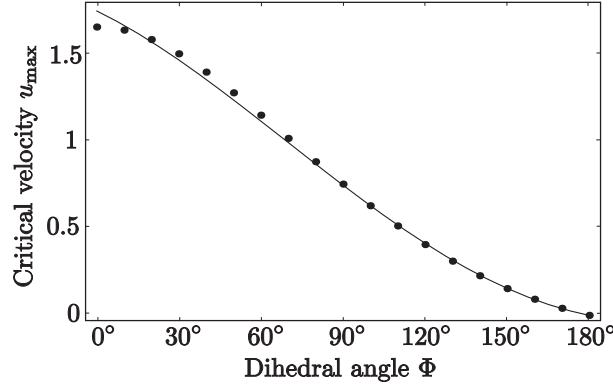


Figure 3.10: The normalized critical pore velocity  $u_{\max}$  is shown as a function of the dihedral angle  $\Phi$ . The numerical results are given by points, the solid line is the analytical approximation (3.74).

It should be emphasized that in our stationary approach pore width  $R_p$  is fixed and used to normalize lengths. In dynamic situations, pore width changes either during detachment or with varying boundary velocity [Svoboda and Riedel, 1992]. We did not incorporate a physical constraint on pore width such as volume conservation [Hsueh et al., 1982, Spears and Evans, 1982] since our main interest is whether a particular pore remains attached to the boundary moving with fixed velocity. If a stationary solution exists, the width of the attached pore remains constant.

### 3.3.4 Bifurcation

We now discuss a critical problem: why does the solution disappear, what are the mathematical reasons for that? In other words: we have to investigate, whether we observe a real phenomenon or could it be attributed to some imperfectness of the numerical algorithm near the singular point, e.g., to numerical instabilities mentioned in [Hsueh et al., 1982]?

Let us recall that our nonlinear boundary problem has unique physical solutions, as shown by the series expansion for small  $u$ . More precisely, the solution for  $u > 0$  is unique as long as we look for a state that is continuously connected with the equilibrium state for  $u = 0$ . In the context of Fig. 3.7 that means that the just calculated values of  $\kappa_1$  and  $\Phi_1$  can be used as

a good initial “guess” for investigation of the “next” value of  $u$ . On the other hand, a careful search for *all solutions* of Eqs. (3.48–3.51) results in supplementary states that cannot be derived by a steady increase of the pore velocity. Two examples of such states are shown in Fig. 3.11. Similar necked and even multiply-necked stationary pores were also found for three-dimensional geometry [Yu and Suo, 1999].

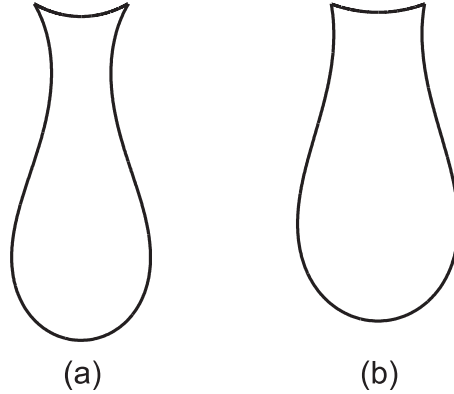


Figure 3.11: Two examples of supplementary solutions obtained from Eqs. (3.48–3.51) for (a)  $\Phi = \pi/6$ ,  $u = 0.15$  and (b)  $\Phi = \pi/3$ ,  $u = 0.1$

These supplementary solutions also evolve with increasing velocity. In contrast to the physical solutions described above, pores of supplementary solutions “shorten” with increasing velocity and become identical to the physical solutions for the critical velocity. The solutions “collide” and then disappear together. Such a phenomenon is similar to a saddle-node bifurcation (see, e.g., [Thompson, 1982]) strongly suggesting that our numerical results represent physical reality. This is illustrated in Fig. 3.12 (compare with Fig. 3.7), where an application of the shooting method for  $\Phi = \pi/18$  and  $u$  just below and just above  $u_{\max}$  is shown. The second intersection point corresponds to the supplementary solution. It can be “traced back” to the solutions shown in Fig. 3.11. The collision occurs for  $u = u_{\max}$ .

Note, that if the boundary velocity is smaller than the critical one, the stationary solution does exist. Stability, however, is not guaranteed and can be investigated only in a dynamical treatment. In the case of lenticular pores, such a treatment shows that the stationary solutions are indeed stable and give correct values for critical velocities [Yu and Suo, 1999]. In contrast, supplementary solutions evidently correspond to a larger value of surface energy and are therefore unstable. The analogy with the saddle-node bifurcation also suggests, that the supplementary solutions are unstable [Thompson, 1982].

Our treatment of the channel-like pores trapped by the boundary is now

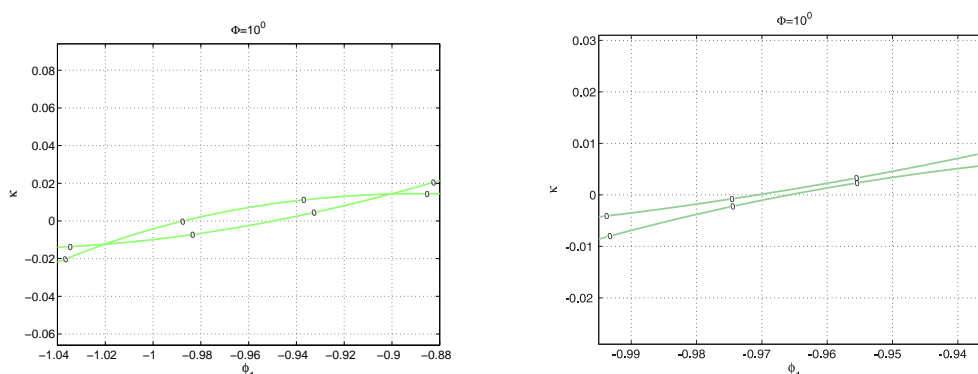


Figure 3.12: Application of the shooting method for  $\Phi = \pi/18$ . Left:  $u$  is slightly before  $u_{\max}$ ; right:  $u$  is slightly above  $u_{\max}$ . The two intersection points correspond to two possible solutions.

complete. In the next section of this chapter we consider channel-like pores that are positioned at the triple junction between three grains.

### 3.4 Pore at a triple junction

In the previous section of this chapter a long channel-like pore was attached to the boundary and moved with it. We now consider a long pore attached to a triple junction, i.e., to a long straight channel along three grain edges. As above, in the equilibrium state the pore surface consists of circle segments with equal curvatures. However, there are three such segments — one segment for each grain-pore interface. The grain boundaries enclose equal angles and form three tips. A cross-section of the equilibrium channel-like pore looks like a (curved) triangle as shown in Fig. 3.13.

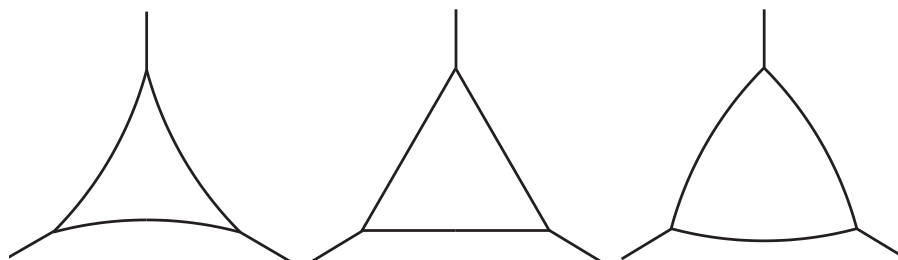


Figure 3.13: Cross-sections of equilibrium channel-like pores at triple junctions for three different dihedral angles: (a)  $\Phi = \pi/6$ , (b)  $\Phi = \pi/3$ , (c)  $\Phi = \pi/2$ .

As we see, the cross section can have different shapes. It can reduce to a right triangle for  $\Phi = \pi/3$  and to a sphere for  $\Phi = \pi$  (compare with Fig. 3.3). All dihedral angles are assumed equal. Also the boundaries are assumed to meet each other at equilibrium  $2\pi/3$  angle.

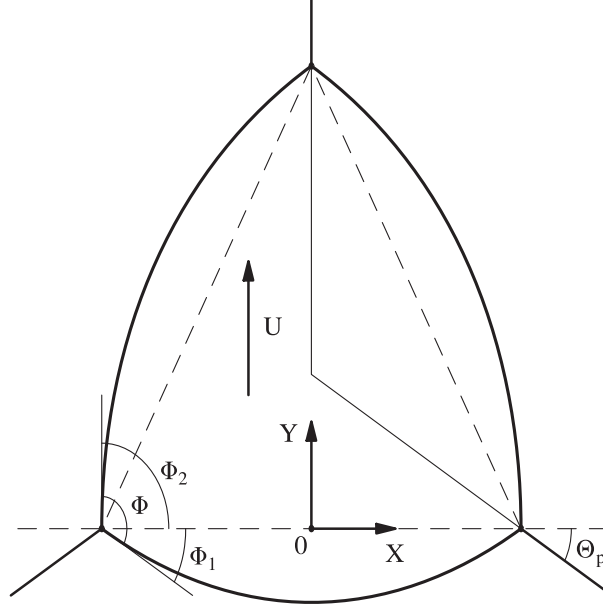


Figure 3.14: Geometry of a moving pore at the triple junction.

Let us now consider the case, where an external surface tension force deforms the pore and brings it to motion as shown in Fig. 3.14. We assume all boundaries to move with a common velocity  $U$  and consider only symmetrical solutions so that there are only two directions of motion: upwards and downwards. In contrast with the previous section, these directions should be distinguished, in particular both the corresponding perturbations of the pore shape and critical velocities are not identical. Another point to be considered is the drag angle. Henceforth, we refer to  $\Theta_p$  in Fig. 3.14 as the pore drag angle, so that the equilibrium drag angle is  $\pi/6$ . The  $OZ$  projection of the drag force reads

$$K_{\text{pore drag}} = L_p \gamma_b (1 - 2 \sin \Theta_p) \quad (3.76)$$

and the pore moves upwards for  $\Theta_p < \pi/6$  and downwards for  $\Theta_p > \pi/6$ . For small drag forces  $\Theta_p \approx \pi/6$  and

$$K_{\text{pore drag}} = \sqrt{3} \left( \frac{\pi}{6} - \Theta_p \right) L_p \gamma_b. \quad (3.77)$$

In this case the resulting velocity is proportional to the drag force and one can introduce pore mobility. In the following sections we first perform an an-

alytical calculation of this mobility. The results obtained are then compared with the direct numerical solution of the normalized basic Eqs. (3.48–3.51) and with the mobility of the pore at a boundary. The numerical solutions are finally used to determine critical velocities both for upwards and downwards pore motion.

### 3.4.1 Pore mobility at a triple junction

#### Problem posing

As in the section 3.3, pore branches are assumed to be given in parametric form, i.e.,  $x_i(s)$  and  $z_i(s)$  by means of the natural parameter  $s$ ; index  $i$  attributes to different branches ( $i = 1$  for the lower pore branch,  $i = 2$  for the upper left, and  $i = 3$  for the upper right branch in Fig. 3.14). Our basic system of Eqs. (3.48–3.51) is identical for all three indices and specifies  $x_i(s)$ ,  $z_i(s)$ ,  $\kappa_i(s)$ , and  $\varphi_i(s)$ . We have four differential equations, which should be solved three times for the three pore branches. Therefore twelve boundary conditions are necessary. It is however natural to use symmetry of the equilibrium pore and to restrict ourselves to the symmetrical solutions. Therefore we have to consider only two branches, e.g., the upper left branch ( $i = 2$ ) and the left half of the lower branch ( $i = 1$ ). Eight conditions are necessary.

First of all, for  $s = 0$  our branches have to meet at the point  $x = -1$ ,  $z = 0$  (left pore tip), therefore [similar to Eqs. (3.53–3.54)]

$$x_1(0) = x_2(0) = -1, \quad (3.78)$$

$$z_1(0) = z_2(0) = 0. \quad (3.79)$$

The curvature should be continuous at the tips whereas  $\varphi_1$  and  $\varphi_2$  should combine to provide the predefined dihedral angle  $\Phi$ . Therefore we have two additional conditions at the left tip [similar to Eqs. (3.55–3.56)]

$$-\varphi_1(0) + \varphi_2(0) = \Phi, \quad (3.80)$$

$$\kappa_1(0) + \kappa_2(0) = 0. \quad (3.81)$$

Further, at some yet unknown values of the natural parameters,  $s_{1,2}^{\max}$  the pore branches intersect the  $z$  axis; the latter is the symmetry axis of our solution. Therefore we have four more conditions [note the difference from Eqs. (3.57–3.58)]

$$x_1(s_1^{\max}) = x_2(s_2^{\max}) = 0, \quad (3.82)$$

$$\varphi_1(s_1^{\max}) = 0. \quad (3.83)$$

$$\varphi_2(s_2^{\max}) = \frac{1}{2}(\pi - \Phi). \quad (3.84)$$

Altogether we have specified ten conditions instead of eight, however they incorporate two extraneous unknowns  $s_{1,2}^{\max}$ . The problem is correctly posed. The boundary conditions on the right tip are satisfied automatically because of symmetry.

### Solution strategy

In principle, the strategy is similar to that used in Section 3.3, however, the solution is much more cumbersome. We solve our equations for the small values of  $u$  using the Taylor expansion given in Eq. (3.47). The solution allows us to find a drag angle [see Fig. 3.14 and note the difference from Eq. (3.59)]

$$\Theta_p = \frac{\varphi_1(s) + \varphi_2(s)}{2} \Big|_{s=0}, \quad (3.85)$$

where the difference  $\pi/6 - \Theta_p$  is proportional to the dimensionless velocity  $u$ . This proportionality must be substituted into Eq. (3.77). Thereafter the latter equation must be rewritten in physical units for the velocity. We get a linear dependence between the drag force and the resulting pore velocity and can calculate the mobility of the pore.

As in Section 3.3, the equations for  $z_{1,2}(s)$  are actually independent of the others, one can find the other variables and then restore  $z_{1,2}(s)$  if necessary. That requires two additional direct integrations, where the integration constants are determined by the conditions (3.79). Therefore we have to solve three Eqs. (3.48), (3.49), and (3.50) for each of the two branches. Let us now describe the solution.

### Equilibrium state

The state occurs for  $u = 0$ ; the pore is constructed of three equal circle segments, the drag angle is  $\pi/6$ . For  $u = 0$  the curvatures from Eq. (3.49) are constant  $\partial_s \kappa_{1,2} = 0$ , therefore  $\varphi_{1,2}(s)$  and then  $x_{1,2}(s)$  can be found by direct integration of Eqs. (3.48) and (3.50), respectively. It is convenient to introduce two new parameters [compare with Eqs. (3.61) and (3.62)]

$$\rho = \frac{1}{\sin(\Phi/2 - \pi/6)} \quad (3.86)$$

and

$$s_0 = \rho \left( \frac{\Phi}{2} - \frac{\pi}{6} \right), \quad (3.87)$$

where the former is the common radius of the equilibrium pore segments (normalized by  $R_p$ ) and the latter is the normalized half length of the segments.

The constant curvatures of the pore branches at equilibrium read

$$\kappa_1 = \frac{1}{\rho} \quad \kappa_2 = -\frac{1}{\rho},$$

and therefore we can directly integrate Eq. (3.48) for  $\partial_s \varphi$  to obtain

$$\varphi_1 = \frac{s - s_1^{\max}}{\rho}, \quad \varphi_2 = \frac{\pi}{2} - \frac{\Phi}{2} - \frac{s - s_2^{\max}}{\rho},$$

where we take into account the boundary conditions (3.83) and (3.84). Now we can integrate  $\cos \varphi_{1,2}(s)$  in Eq.(3.50) to obtain  $x_{1,2}(s)$ , i.e.,

$$x_1 = \rho \sin \frac{s - s_1^{\max}}{\rho}, \quad x_2 = \rho \cos \frac{\Phi}{2} - \rho \cos \left( \frac{s - s_2^{\max}}{\rho} + \frac{\Phi}{2} \right),$$

where we take into account the boundary conditions given by (3.82). Further, considering our set of ten boundary conditions we see that only three of them given by Eqs. (3.78) and (3.80) still have to be satisfied. These conditions are satisfied if [compare with Eq. (3.63)]

$$s_1^{\max} = s_0 \quad \text{and} \quad s_2^{\max} = 2s_0. \quad (3.88)$$

Hence, the equilibrium state is completely defined. We now perform the next step of the perturbation theory.

### Perturbation

To quantify the perturbed solution we present all variables as a sum of the equilibrium ones and a small perturbation. This should be done separately for each pore branch, in our case only for two branches. Therefore,

$$\begin{aligned} \kappa_1 &= \frac{1}{\rho} + \tilde{\kappa}_1 & \kappa_2 &= -\frac{1}{\rho} + \tilde{\kappa}_2 \\ \varphi_1 &= \frac{s - s_0}{\rho} + \tilde{\varphi}_1 & \varphi_2 &= \frac{\pi}{2} - \frac{\Phi}{2} - \frac{s - 2s_0}{\rho} + \tilde{\varphi}_2 \\ x_1 &= \rho \sin \frac{s - s_0}{\rho} + \tilde{x}_1 & x_2 &= \rho \cos \frac{\Phi}{2} - \rho \cos \left( \frac{s - 2s_0}{\rho} + \frac{\Phi}{2} \right) + \tilde{x}_2 \end{aligned}$$

where all perturbations are denoted by tilde and are proportional to  $u$ .



### Reformulation of the boundary conditions

First of all the perturbed quantities should be substituted to the boundary conditions. In the first step, inserting  $s = 0$  in the Eqs. (3.53), (3.55), and (3.56) for the left tip we obtain four conditions similar to Eqs. (3.64–3.66)

$$\tilde{x}_{1,2}(0) = 0, \quad (3.89)$$

$$-\tilde{\varphi}_1(0) + \tilde{\varphi}_2(0) = 0, \quad (3.90)$$

$$\tilde{\kappa}_1(0) + \tilde{\kappa}_2(0) = 0. \quad (3.91)$$

The other conditions involve  $s = s_{1,2}^{\max}$ . They are not so simple, because the equilibrium values of  $s_{1,2}^{\max}$  should be perturbed as well. Therefore we substitute

$$\begin{aligned} s_1^{\max} &= s_0 + \delta_1 \\ s_2^{\max} &= 2s_0 + \delta_2 \end{aligned}$$

with  $\delta_{1,2} \sim u$  into (3.82), (3.83), and (3.84) and use a Taylor expansion in  $\delta$  to obtain

$$\begin{aligned} \delta_1 + \tilde{x}_1(s_0) &= 0, & \delta_1 + \rho\tilde{\varphi}_1(s_0) &= 0, \\ \delta_2 \sin \frac{\Phi}{2} + \tilde{x}_2(2s_0) &= 0, & -\delta_2 + \rho\tilde{\varphi}_2(2s_0) &= 0. \end{aligned}$$

As in the Section 3.3, one can eliminate  $\delta_{1,2}$  and write two equations directly for the “old” values of  $s_{1,2}^{\max}$  [compare with Eqs. (3.67) and (3.68)]

$$\tilde{x}_1(s_0) - \rho\tilde{\varphi}_1(s_0) = 0, \quad (3.92)$$

$$\tilde{x}_2(2s_0) + \rho \sin \frac{\Phi}{2} \tilde{\varphi}_2(2s_0) = 0. \quad (3.93)$$

Altogether we have six conditions (3.89–3.93) [compare with (3.64–3.68)] to specify six integration constants in the further expressions for  $\tilde{\kappa}_{1,2}(s)$ ,  $\tilde{\varphi}_{1,2}(s)$ , and  $\tilde{x}_{1,2}(s)$ .

### Perturbation of the lower branch

We substitute the perturbed expressions for  $\kappa_1(s)$ ,  $\varphi_1(s)$ ,  $x_1(s)$  in our basic system and obtain

$$\begin{aligned} \partial_s \tilde{\kappa}_1 &= -u\rho \sin \frac{s-s_0}{\rho}, \\ \partial_s \tilde{\varphi}_1 &= \tilde{\kappa}_1, \\ \partial_s \tilde{x}_1 &= -\sin \frac{s-s_0}{\rho} \tilde{\varphi}_1, \end{aligned}$$

which is a system of linear ordinary differential equations. It can be directly integrated

$$\begin{aligned}\tilde{\kappa}_1 &= u\rho^2 \cos \frac{s-s_0}{\rho} + u\rho^2 C_1, \\ \tilde{\varphi}_1 &= u\rho^3 \sin \frac{s-s_0}{\rho} + u\rho^3 \frac{s-s_0}{\rho} C_1 + u\rho^3 C_2, \\ \tilde{x}_1 &= -\frac{1}{2}u\rho^4 \left( \frac{s-s_0}{\rho} - \sin \frac{s-s_0}{\rho} \cos \frac{s-s_0}{\rho} \right) \\ &\quad - u\rho^4 \left( \sin \frac{s-s_0}{\rho} - \frac{s-s_0}{\rho} \cos \frac{s-s_0}{\rho} \right) C_1 \\ &\quad + u\rho^4 \cos \frac{s-s_0}{\rho} C_2 + u\rho^4 C_3,\end{aligned}$$

where  $C_{1,2,3}$  are integration constants.

### Perturbation of the upper branch

In a similar way, we substitute the perturbed expressions for  $\kappa_2(s)$ ,  $\varphi_2(s)$ ,  $x_2(s)$  in our basic system to get

$$\begin{aligned}\partial_s \tilde{\kappa}_2 &= u\rho \cos \left( \frac{s-2s_0}{\rho} + \frac{\Phi}{2} \right) - u\rho \cos \frac{\Phi}{2}, \\ \partial_s \tilde{\varphi}_2 &= \tilde{\kappa}_2, \\ \partial_s \tilde{x}_2 &= -\cos \left( \frac{s-2s_0}{\rho} + \frac{\Phi}{2} \right) \tilde{\varphi}_2,\end{aligned}$$

and therefore after cumbersome but direct integration we get

$$\begin{aligned}\tilde{\kappa}_2 &= u\rho^2 \sin \left( \frac{s-2s_0}{\rho} + \frac{\Phi}{2} \right) - u\rho^2 \cos \frac{\Phi}{2} \left( \frac{s-2s_0}{\rho} + \frac{\Phi}{2} \right) + u\rho^2 D_1, \\ \tilde{\varphi}_2 &= -u\rho^3 \cos \left( \frac{s-2s_0}{\rho} + \frac{\Phi}{2} \right) - \frac{1}{2}u\rho^3 \cos \frac{\Phi}{2} \left( \frac{s-2s_0}{\rho} + \frac{\Phi}{2} \right)^2 \\ &\quad + u\rho^3 \left( \frac{s-2s_0}{\rho} + \frac{\Phi}{2} \right) D_1 + u\rho^3 D_2,\end{aligned}$$

and

$$\begin{aligned}
\tilde{x}_2 = & \frac{1}{2}u\rho^4 \left[ \left( \frac{s-2s_0}{\rho} + \frac{\Phi}{2} \right) + \sin \left( \frac{s-2s_0}{\rho} + \frac{\Phi}{2} \right) \cos \left( \frac{s-2s_0}{\rho} + \frac{\Phi}{2} \right) \right] \\
& + \frac{1}{2}u\rho^4 \cos \frac{\Phi}{2} \left[ \left( \frac{s-2s_0}{\rho} + \frac{\Phi}{2} \right)^2 \sin \left( \frac{s-2s_0}{\rho} + \frac{\Phi}{2} \right) \right. \\
& \quad + 2 \left( \frac{s-2s_0}{\rho} + \frac{\Phi}{2} \right) \cos \left( \frac{s-2s_0}{\rho} + \frac{\Phi}{2} \right) \\
& \quad \left. - 2 \sin \left( \frac{s-2s_0}{\rho} + \frac{\Phi}{2} \right) \right] \\
& - u\rho^4 \left[ \left( \frac{s-2s_0}{\rho} + \frac{\Phi}{2} \right) \sin \left( \frac{s-2s_0}{\rho} + \frac{\Phi}{2} \right) + \cos \left( \frac{s-2s_0}{\rho} + \frac{\Phi}{2} \right) \right] D_1 \\
& - u\rho^4 \sin \left( \frac{s-2s_0}{\rho} + \frac{\Phi}{2} \right) D_2 + u\rho^4 D_3,
\end{aligned}$$

where  $D_{1,2,3}$  are integration constants.

### Mobility

We have now to substitute the expressions for  $\tilde{\kappa}_{1,2}(s)$ ,  $\tilde{\varphi}_{1,2}(s)$ , and  $\tilde{x}_{1,2}(s)$  to the perturbed boundary conditions given by Eqs. (3.89–3.93). The result is a closed system of six equations that uniquely determines  $C_{1,2,3}$  and  $D_{1,2,3}$ , and therefore uniquely determines the perturbed solution. We use the following notations

$$\alpha = \frac{s_0}{\rho} = \frac{\Phi}{2} - \frac{\pi}{6} \quad (3.94)$$

and

$$\beta = \frac{\Phi}{2} - \frac{2s_0}{\rho} = \frac{\pi}{3} - \frac{\Phi}{2} \quad (3.95)$$

and derive the following set of six equations.

- From Eq. (3.92) it follows that

$$C_3 = 0.$$

- From Eq. (3.93) it follows that

$$\cos \frac{\Phi}{2} D_1 - D_3 = \frac{\Phi}{2} \left( \frac{1}{2} + \cos^2 \frac{\Phi}{2} \right) - \frac{3}{2} \sin \frac{\Phi}{2} \cos \frac{\Phi}{2}.$$

- From Eq. (3.91) it follows that

$$C_1 + D_1 = \beta \cos \frac{\Phi}{2} - \sin \beta - \cos \alpha.$$

- From Eq. (3.90) it follows that

$$\alpha C_1 - C_2 + \beta D_1 + D_2 = \cos \beta + \frac{1}{2} \beta^2 \cos \frac{\Phi}{2} - \sin \alpha.$$

- From  $\tilde{x}_1(0) = 0$  [Eq. (3.89)] it follows that

$$(\sin \alpha - \alpha \cos \alpha) C_1 + \cos \alpha C_2 = \frac{1}{2} \sin \alpha \cos \alpha - \frac{1}{2} \alpha.$$

- From  $\tilde{x}_2(0) = 0$  [Eq. (3.89)] it follows that

$$\begin{aligned} (\beta \sin \beta + \cos \beta) D_1 + \sin \beta D_2 - D_3 = \\ \frac{1}{2} (\beta + \sin \beta \cos \beta) + \\ \frac{1}{2} \cos \frac{\Phi}{2} (\beta^2 \sin \beta + 2\beta \cos \beta - 2 \sin \beta). \end{aligned}$$

Altogether, we have six integration constants and six restrictions to find them. The cumbersome final expressions for  $C_{1,2,3}$  and  $D_{1,2,3}$  can be found directly or better using computer algebra programs and are not of great interest, however, they give us a possibility to find the drag angle

$$\Theta_p = \frac{\varphi_1(0) + \varphi_2(0)}{2} = \frac{\pi}{6} + \frac{\tilde{\varphi}_1(0) + \tilde{\varphi}_2(0)}{2} = \frac{\pi}{6} + \frac{C_2 - \alpha C_1 - \sin \alpha}{\sin^3 \alpha} u,$$

where we replaced  $\rho$  by  $\sin^{-1} \alpha$ , and then to find the mobility of the pore. The final expression for the mobility of a pore at a triple junction reads

$$M_p^{3j} = \mathfrak{M} \frac{D_s \Omega \delta}{k T L_p R_p^3}, \quad (3.96)$$

where the factor  $\mathfrak{M}$  depends only on dihedral angle and is given by a very cumbersome expression

$$\mathfrak{M}(\Phi) = \frac{6 \cos(\frac{\Phi}{2} - \frac{\pi}{6}) - 3 \cos(\frac{5\Phi}{2} + \frac{\pi}{6}) - 9 \sin(\frac{3\Phi}{2})}{k_1 + k_2 \cos(\Phi + \frac{\pi}{6}) + k_3 \cos(2\Phi + \frac{\pi}{6}) + k_4 \sin 2\Phi}, \quad (3.97)$$

where

$$\begin{aligned} k_1 &= -36 + 2\sqrt{3}\pi - 6\sqrt{3}\Phi \\ k_2 &= -24\sqrt{3} + 20\pi - 60\Phi, \\ k_3 &= 4\pi - 12\Phi \\ k_4 &= 24\sqrt{3}. \end{aligned}$$

The general structure of the mobility given by Eq. (3.96) is similar to that of Eq. (3.70). The dependence on the dihedral angle from Eq. (3.97) is, however, much more complicated. Nevertheless the numerical value of  $\mathfrak{M}(\Phi)$  is always comparable with unity. For instance,  $\mathfrak{M} \rightarrow 1/2$  for  $\Phi \rightarrow \pi/3$ , the simple case of a pore with a triangular cross-section, which can be also solved independently using a small slope approximation. The normalized mobility as calculated from Eq. (3.97) is shown in Fig. 3.15.

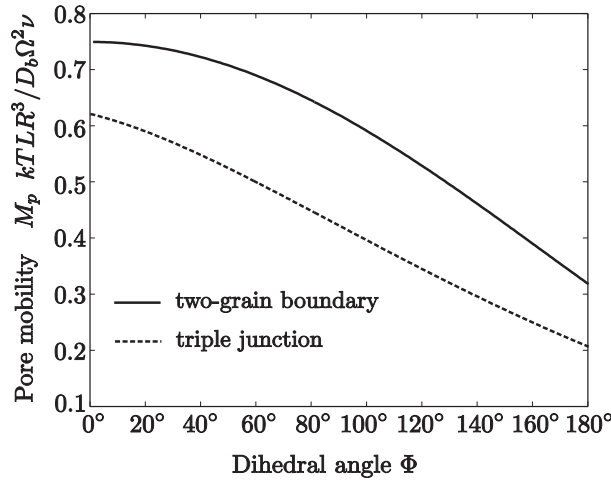


Figure 3.15: Pore mobility at the triple junction [normalized in accord with Eq. (3.96)] versus dihedral angle (dotted line). For comparison the mobility of the pore at the boundary [Eq. (3.70)] is also shown (solid line).

We see that the dependence of  $M_p^{3j}$  on the dihedral angle is weak and that the mobility decreases with an increase of  $\Phi$ . The mobility  $M_p^{3j}$  is always smaller than  $M_p$  from Section 3.3. For instance, for  $\Phi = \pi/3$  the ratio  $M_p^{3j}/M_p \approx 0.72$ . Equation (3.97) is also in good agreement with our numerical results for small velocities. The numerics is described in the next section together with the calculation of critical velocities.

### 3.4.2 Numerical solutions and critical velocities

In this section solutions of Eqs. (3.48–3.51) are sought numerically for the case of a triple junction. The symmetry arguments allow us to reduce the calculations to only two branches. In fact, the shooting method can be applied as in Section 3.3.3 with only small modifications. We assume some small velocity  $u$  to provide a small perturbation of the equilibrium pore. Then we produce a two-parametric set of trial branches by integrating the system (3.48–3.51) starting from the left tip. To this end, we fix the tip curvature  $\kappa_1$  and  $\Phi_1$ ; the other tip parameters are determined from the left tip boundary conditions [Eqs. (3.80–3.81)].

The branches are calculated up to the symmetry axis, i.e., the end points are determined by Eq. (3.82). In this way the values of  $s_{1,2}^{\max}$  are calculated. Then we impose the other boundary restrictions (3.83) and (3.84). This allows us to trace the only suitable trial solution and to determine  $\kappa_1$  and  $\Phi_1$ . The shape of the moving pore is completely constrained owing to symmetry. The boundary conditions at the right tip are satisfied automatically. We then increase the velocity and repeat the whole procedure as long as a solution exists.

With increasing  $u$ , the pore shape strongly deviates from the stationary shape as illustrated in Fig. 3.16. From the numerical solutions one can derive the relation between the pore drag angle  $\Theta_p$  and the pore velocity  $u$  (Fig. 3.17). The dependence is linear for small velocities and can be used to check Eq. (3.97) for the mobility, the correspondence between the theory and numerics is good.

In contrast to mobilities, the critical velocities can be derived only from numerical solution. Note that positive (upwards motion) and negative (downwards motion) values of the velocity should be distinguished. For positive velocity detachment will leave the pore in the bottom grain. For negative velocity detachment will transfer the pore to a grain boundary from whereon the mechanism from the Section 3.3 operates. Depending on the direction of velocity, the pores are quite differently distorted (Fig. 3.16). In the negative direction, detachment occurs at critical velocities that are smaller by a factor of ca. 5 than the critical velocities for detachment during motion in the positive direction (Fig. 3.18). Thus, a pore, which is initially at a triple junction, is most likely detached to a grain boundary; the direct detachment to the body of the bottom grain requires considerably larger boundary velocities and possibly negative drag angles.

Our numerical results for the critical velocities are shown in Fig. 3.18. Analytical expressions for the numerical data on  $u_{\max}^{\pm}(\Phi)$  are similar to

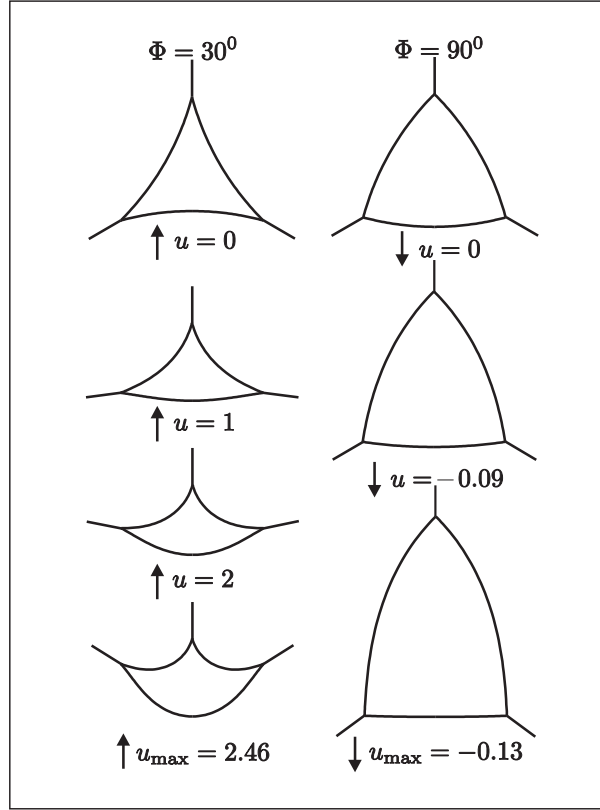


Figure 3.16: Changes of pore shape with variations of the normalized velocity  $u$  for two different dihedral angles and two different directions of motion. If  $u$  exceeds some critical value, no solution exists and the coupled motion of the pore and the triple junction is not possible.

Eq. (3.74) and read

$$u_{\max}^+ = (2.85 - 0.65\Phi) \cos \frac{\Phi}{2}, \quad (3.98)$$

$$u_{\max}^- = -(0.34 - 0.088\Phi) \cos \frac{\Phi}{2}. \quad (3.99)$$

The latter expressions are seen to be good approximations (Fig. 3.18). Similar to Section 3.3 it is convenient to transform the latter equations to physical units

$$U_{\max}^+ = (1.43 - 0.32\Phi) \frac{D_s \Omega \delta}{kT} \frac{\gamma_b}{R_p^3}, \quad (3.100)$$

$$U_{\max}^- = -(0.17 - 0.044\Phi) \frac{D_s \Omega \delta}{kT} \frac{\gamma_b}{R_p^3}. \quad (3.101)$$

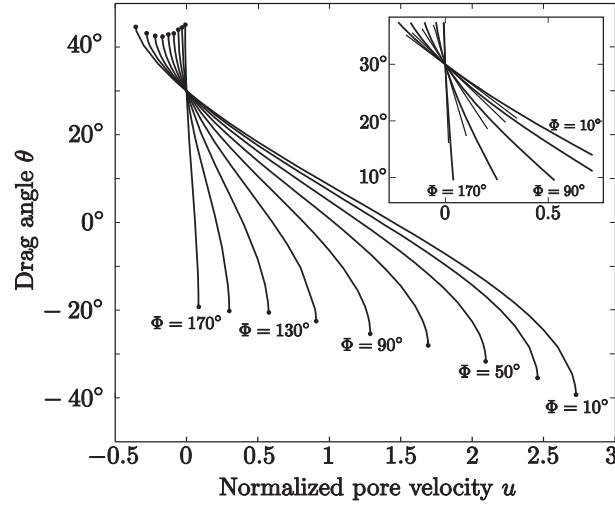


Figure 3.17: Relation between the pore drag angle  $\Theta_p$  and the normalized boundary velocity  $u$  for a pore at a triple junction as obtained from numerical solutions of Eqs. (3.48–3.51). Lines correspond to different values of the dihedral angle  $\Phi$  as indicated by the labels. The drag angle increases for negative (downwards) pore velocities; for positive (upwards) pore velocities it decreases and even changes sign. The points at the ends of the lines indicate the values of the critical velocities and peak drag angles. The numerical solutions agree with the analytical results (tangents) derived from Eq.(3.97) for the small velocities, as shown in the insert in the top right corner.

As we see, the critical velocities only slightly depend on dihedral angle. In either case, the critical velocity for  $\Phi \rightarrow \pi$  is nonzero.



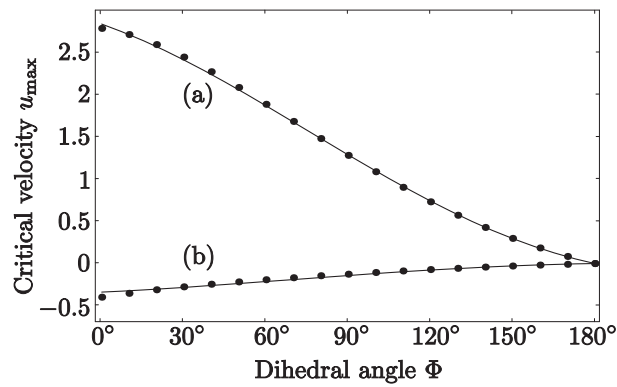


Figure 3.18: The normalized critical velocity  $u_{\max}$  for pores moving (a) in the positive and (b) in the negative direction (see Fig. 3.14), at a triple junction as a function of the dihedral angle. The numerical results are given by points, the solid lines represent analytical approximations given by Eqs. (3.98) and (3.99).



# Chapter 4

## Pore motion controlled by diffusion through the pore-filling fluid

In this chapter, we consider pores filled with a fluid phase, e.g., water or melt, in which the constituting elements of the solid matrix are dissolved. In addition to diffusion along the grain-pore interface now a second transport mechanism is important, diffusion through the fluid-phase. This mechanism of pore motion, as well as corresponding mobilities and critical velocities is discussed in this chapter.

### 4.1 Basic equations

The distribution of matrix atoms in the solution filling the pore is represented by the concentration  $c(\mathbf{r}, t)$ , i.e., number of matrix atoms per unit volume of the solution. The corresponding flux of matrix atoms is denoted by  $\mathbf{j}$ . The latter is given by Fick's first law

$$\mathbf{j} = -D_m \nabla c, \quad (4.1)$$

where the diffusion coefficient  $D_m$  corresponds to the matrix atoms in the solution. Note, that the total number of atoms changes only on the boundaries where dissolution and precipitation may occur. Therefore inside the pore a general continuity equation for  $c(\mathbf{r}, t)$  should be satisfied

$$\partial_t c + \operatorname{div} \mathbf{j} = 0. \quad (4.2)$$

Combining (4.1) and (4.2) we see that the concentration is subject to a parabolic diffusion equation (see, e.g., [Crank, 1975])

$$\partial_t c = D_m \nabla^2 c, \quad (4.3)$$

where the diffusion coefficient  $D_m$  is assumed to be an isotropic constant. The characteristic time of evolution of  $c$  is given by  $R_p^2/D_m$ , where  $R_p$  is the pore radius. This time is generally much smaller than the characteristic time of pore and boundary motion. That is, the equilibrium concentration of  $c$  is quickly established. Using the modern language of synergetic, one can say that the concentration  $c$  is “slaved” [Haken, 2004] and given by the elliptic Laplace equation

$$\nabla^2 c = 0. \quad (4.4)$$

where  $c(x, y, z, t)$  only shows “slow” variation with time so that the time derivative in the Eq. (4.3) can be ignored. The time dependence is determined by an additional process, not directly by diffusion through the pore-filling fluid. This process can affect Eq. (4.4) through time dependent parameters or through time dependent boundary conditions. In general, neither Eq. (4.3) nor Eq. (4.4) can be solved without boundary conditions on the pore surface. To formulate them we first introduce an equilibrium concentration  $c_0$  of the solution at a *plane* interface with the solid matrix. If  $c = c_0$  the rates of dissolution and precipitation at a plane interface between solid and solution are equal. The value of  $c_0$  depends on pressure and temperature. Note, that starting from a non-equilibrium situation at the solid-solution interface, there is a characteristic time for the equilibrium concentration to establish through differential dissolution and precipitation. For most applications, the diffusion processes we are interested in are much slower than the characteristic time for the attainment of a local equilibrium at the solid-solution interface. Therefore we assume that the equilibrium concentration is established instantaneously.

If the surface of the pore is *curved*, the equilibrium concentration of the solution is denoted by  $c_s$  and is defined by the Gibbs-Thompson relation (see e.g., [Partington, 1952])

$$c_s = c_0(1 - \Gamma\kappa), \quad (4.5)$$

where  $\kappa$  is a mean curvature of the interface and a proportionality factor  $\Gamma$  is a constant measured in units of length. As usual, we assume that the pore-grain interface is given explicitly  $z = g(x, y, t)$  in a local coordinate frame with the  $OZ$  axis directed inwards into the pore. Equation (4.5) indicates that if the interface is convex with respect to the solid (and therefore the mean curvature given by Eq. (3.5) is negative)  $c_s > c_0$  and vice versa. The collective effect of both dissolution-precipitation and diffusion through the

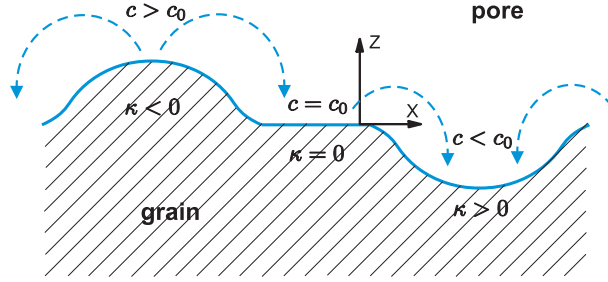


Figure 4.1: Equilibrium concentration of the solution depends on the curvature of the solid-solution interface in accord with Eq. (4.5). Note, that diffusion through the pore-filling fluid permanently removes atoms from the regions where the grain-pore interface is convex and  $c_s > c_0$ . This reduction of concentration is compensated through permanent dissolution from the grain surface. Therefore a “peak” on the pore-grain interface dissolves. Similarly, a “cave” is filled, because of the combined effects of diffusion and precipitation.

pore-filling fluid is illustrated in Fig. 4.1. Parameter  $\Gamma$  is defined by the relation

$$\Gamma = \frac{\gamma_s \Omega}{kT}, \quad (4.6)$$

i.e., through the pore-boundary surface tension coefficient, atomic volume, and temperature in energetic units. For typical system parameters the value  $\Gamma \simeq 10^{-7} cm$  [Mullins, 1960]. The boundary condition we look for simply states that

$$c(\mathbf{r}, t) \Big|_{z=g(x,y,t)} = c_s. \quad (4.7)$$

Equations (4.4) and (4.7) completely determine the concentration of the matrix atoms in the solution and do not contain the time derivative. As discussed above, the concentration can still depend on time. However, the dependence results from a process that is slower than diffusion, e.g., from the motion of the pore surfaces. Let us describe this in more detail now.

From the general point of view the evolution of the pore surface is given by the general dynamic Eq. (3.3) for  $z = g(x, y, t)$ . However, the expression for the normal velocity of the surface  $v_n$  differs from that used in (3.4) and must be derived separately.

Let us consider an element  $dS$  of the pore surface. If its normal displacement is  $v_n dt$ , the corresponding increase of the grain volume is  $dS v_n dt$  and the ratio  $dS v_n dt / \Omega$  gives the net “income” (precipitation minus dissolution) of the matrix atoms. The latter are supplied by the diffusion flux. The net income equals  $-j_n dS dt$ , where the flux  $\mathbf{j}$  is projected on the outward

(with respect to the grain) normal vector  $\mathbf{n}$  and is negative for positive  $v_n$ . Therefore

$$j_n = -\frac{v_n}{\Omega}$$

and using Fick's first law (4.1) we obtain

$$v_n = D_m \Omega \cdot (\nabla c)_n = D_m \Omega (\mathbf{n} \nabla c) \Big|_{z=g(x,y,t)} = D_m \Omega \left( \frac{\partial c}{\partial n} \right)_{z=g(x,y,t)}. \quad (4.8)$$

### 4.1.1 Mathematical model

Let us summarize the mathematical (and numerical) model that will be used in this chapter. The surface  $z = g(x, y, t)$  is attributed to some local coordinate frame and separates the grain (with  $z < g$ ) and the pore (with  $z > g$ ). To obtain the concentration  $c(\mathbf{r}, t)$  one must solve the Laplace equation inside the pore, i.e.,

$$\nabla^2 c = 0, \quad \text{for } z > g(x, y, t) \quad (4.9)$$

with the boundary condition

$$c \Big|_{z=g(x,y,t)} = c_0(1 - \Gamma \kappa), \quad (4.10)$$

where the mean curvature is

$$\kappa = \operatorname{div} \left( \frac{\nabla g}{\sqrt{1 + |\nabla g|^2}} \right). \quad (4.11)$$

The motion of the pore surface is then determined from

$$\partial_t g = v_n \sqrt{1 + |\nabla g|^2}, \quad (4.12)$$

where in accord with Eq. (4.8)

$$v_n = D_m \Omega \left( \frac{\partial c}{\partial n} \right)_{z=g(t,x,y)}. \quad (4.13)$$

In this way the position of the pore interface at time  $t$  can be used to calculate its position at time  $t + dt$ . This new position is then used to solve the Laplace equation again, and so on.

### 4.1.2 Example

The equations presented in the previous subsection look (and indeed are) rather complicated. Therefore it is convenient to illustrate them with a simple example (following [*Lifshitz and Slyozov, 1961*]), where the problem in question (i.e., a nonlinear problem with moving boundaries) allows for a full solution. Let us consider a spherical inclusion with an initial radius  $r_s(0)$  that is inserted into the solution with the constant concentration  $c_\infty$ . The dissolution-precipitation process changes (increases) the equilibrium concentration just near the inclusion, at any moment of time the new concentration is

$$c_s = c_0 \left[ 1 + \frac{2\Gamma}{r_s(t)} \right]. \quad (4.14)$$

The difference between  $c_s$  and  $c_\infty$  causes flux of matrix atoms, which in turn results in either increasing or decreasing  $r_s(t)$ . The latter should be determined.

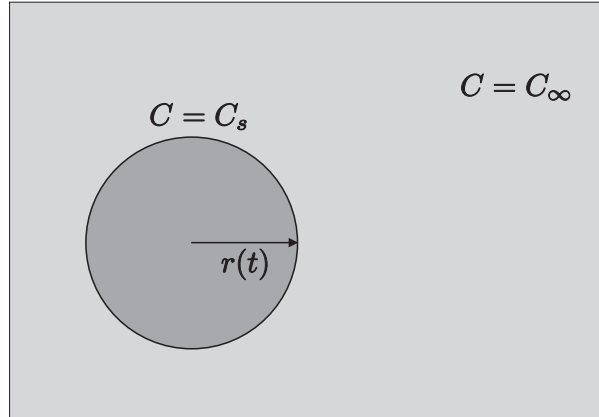


Figure 4.2: Evolution of a spherical inclusion: growth or collapse?

At each moment of time the concentration is determined by a radially symmetric solution  $c(r, t)$  of the Laplace equation

$$\nabla^2 c = \frac{1}{r^2} \frac{\partial}{\partial r} \left( r^2 \frac{\partial c}{\partial r} \right) = 0$$

with the boundary conditions

$$c(r, t) \Big|_{r \rightarrow \infty} = c_\infty \quad \text{and} \quad c(r, t) \Big|_{r=r_s} = c_s.$$

This situation can be compared to an electrical potential created by a charged sphere, where the potential at infinity is  $c_\infty$  and the sphere potential is  $c_s$ .

Therefore the solution reads

$$c = c_\infty + (c_s - c_\infty) \frac{r_s}{r}.$$

This latter expression can also be obtained by direct integration. We now calculate

$$\left( \frac{\partial c}{\partial n} \right)_{r=r_s} = \left( \frac{\partial c}{\partial r} \right)_{r=r_s} = - \frac{c_s - c_\infty}{r_s}.$$

The evolution of  $r_s(t)$  is determined by the equation

$$\dot{r}_s = D_m \Omega \left( \frac{\partial c}{\partial n} \right)_s = -D_m \Omega \frac{c_s - c_\infty}{r_s}.$$

Finally inserting  $c_s$  from Eq. (4.14) we obtain a closed ordinary differential equation

$$\dot{r}_s = D_m \Omega \left( \frac{c_\infty - c_0}{r_s} - \frac{2c_0\Gamma}{r_s^2} \right), \quad (4.15)$$

which can be integrated and completely defines  $r_s(t)$ . In the undersaturated solution with  $c_\infty < c_0$  the right-hand-side is always negative and an inclusion disappears independent of its initial size. In the oversaturated solution with  $c_\infty > c_0$  and the initial radius of the inclusion is small enough, namely

$$r_s(0) \leq \frac{2c_0\Gamma}{c_\infty - c_0}$$

the right-hand-side of Eq. (4.15) is still negative and the inclusion disappears again at some  $t = t_0$ . In both cases  $r_s(t)$  decreases and finally only the term  $\sim r_s^{-2}$  is important on the right-hand-side of Eq. (4.15). For  $t$  close to  $t_0$  the radius of the inclusion is given by

$$r_s(t) = \sqrt[3]{6D_m\Omega c_0\Gamma(t_0 - t)}.$$

As we see, an oversaturated solution ( $c_\infty > c_0$ ) can still be in a metastable state and survive by dissolving small matrix inclusions. However, if  $r_s(0)$  is large enough

$$r_s(0) > \frac{2c_0\Gamma}{c_\infty - c_0}$$

the inclusion starts to grow. Here,  $r_s(t)$  increases and finally the  $\sim r_s^{-2}$  term in Eq. (4.15) can be ignored. Asymptotically for  $r_s(t) \gg r_s(0)$  the inclusion radius is determined by [Zener, 1949]

$$r_s(t) = \sqrt{2D_m\Omega(c_\infty - c_0)t}.$$

For this example the geometry of the grain-solution interface is very simple allowing for direct full solution. In general, this is, however, not the case and more sophisticated approaches, e.g. approximations and numerical solutions must be used. They will be discussed in the next sections.



## 4.2 Plane interface

In this section the simplest dynamical equilibrium between a grain and a pore filled with solution is considered. Namely, both pore and grain are formally infinite; the grain is described by the inequality  $z < 0$ , the pore by  $z > 0$  so that the interface is the plane  $z = 0$  with  $\kappa = 0$ . Correspondingly, the concentration of the solution  $c = c_0$ . We are going to investigate stability of such an interface in the small slope approximation. The analysis is similar to that of [Mullins and Sekerka, 1960], where stability of a growing particle is considered. In our case, the interface turns out to be always stable, this indicates that the problem posing in the previous section is correct and physically meaningful. The results of this section will be applied to derive general conclusions about pore motion and to obtain an estimate for the critical velocity thereafter. The method of investigation is standard: we consider a small perturbation of the interface and investigate whether it grows or not.

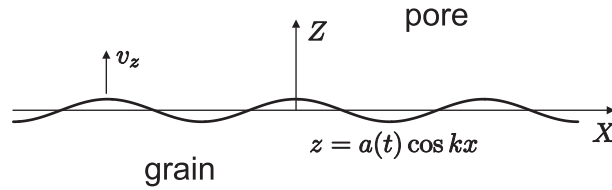


Figure 4.3: Perturbation of a plane interface should disappear if the latter is stable.

After an arbitrary perturbation is applied the new interface is given by some functional dependence  $z = g(x, y, t)$ . If the perturbation is small, the nonlinear character of the interface motion is not important and Eq. (4.12) can be linearized, i.e.,

$$\partial_t g = v_n. \quad (4.16)$$

In particular, one can present  $g(x, y, t)$  as a composition of Fourier harmonics and consider only one harmonic. Without loss of generality the corresponding wave vector is assumed to be parallel to the  $OX$  axis. Thus, the perturbed pore surface is of the form

$$z = g(x, t) = a(t) \cos kx, \quad (4.17)$$

where  $k$  is the wave vector of the perturbation and  $a(t)$  is sought. The perturbation is small if both  $a(t)$  is small and the curvature of the perturbed pore-grain interface remains small. We apply the small slope approximation

$$\kappa = \nabla^2 g = \partial_x^2 g = -ak^2 \cos kx,$$

and assume that the dimensionless combination

$$a\Gamma k^2 \ll 1, \quad (4.18)$$

is much smaller than one. Here,  $\Gamma$  plays the role of a characteristic length scale. The Laplace equation must be solved in the region

$$\nabla^2 c = 0 \quad \text{for} \quad z > a(t) \cos kx$$

with the boundary condition

$$c = c_0(1 + a\Gamma k^2 \cos kx) \quad \text{for} \quad z = a(t) \cos kx.$$

Inequality (4.18) guaranties that the perturbation of the concentration is small. We use this smallness of the perturbation and solve the Laplace equation in the unperturbed region  $z \geq 0$  using the same boundary values but for  $z = 0$ . It is easy to see that the induced error is of order  $O(a^2)$  and can be ignored. Now, the solution for  $c(x, z, t)$ , which

- (i) is a harmonic function,
- (ii) equals  $c_0(1 + a\Gamma k^2 \cos kx)$  at  $z = 0$ ,
- (iii) tends to  $c_0$  for  $z \rightarrow +\infty$ ,

reads

$$c = c_0 \left( 1 + a\Gamma k^2 e^{-kz} \cos kx \right). \quad (4.19)$$

The velocity of the interface

$$v_n = D_m \Omega \left( \frac{\partial c}{\partial n} \right)_{z=a(t) \cos kx}$$

in the same approximation is replaced by

$$v_z = D_m \Omega \left( \frac{\partial c}{\partial z} \right)_{z=0} = -D_m \Omega c_0 \Gamma a k^3 \cos kx.$$

The latter equation is inserted in Eq. (4.16) together with Eq. (4.17). Note that  $\cos kx$  factors disappear indicating that the linear approximation is correctly applied and indeed different harmonics in  $z = g(x, y, t)$  are independent. The final equation for  $a(t)$  reads

$$\dot{a} = -D_m \Omega c_0 \Gamma k^3 a. \quad (4.20)$$

We see that  $a(t)$  decreases and the interface is stable. The initial perturbation with the characteristic space scale  $\mathfrak{R}$  disappears on the time scale

$$\tau = \frac{\mathfrak{R}^3}{D_m \Omega c_0 \Gamma}. \quad (4.21)$$

### 4.2.1 An estimate of the critical velocity

Equation (4.21) can be used to estimate the critical velocity of the pore. Indeed, let a pore with the characteristic radius  $R_p$  move with a constant velocity  $U$ . The corresponding characteristic time is

$$\tau_1 = \frac{R_p}{U}.$$

On the other hand, the permanent displacement of the pore may be considered as a perturbation with the characteristic wave vector  $k \approx 1/R_p$ . In accord with Eq. (4.21) such a perturbation disappears on the time scale

$$\tau_2 = \frac{R_p^3}{D_m \Omega c_0 \Gamma}.$$

Now, the stationary motion is possible if the pore has enough time to react on the perturbation and therefore  $\tau_1 > \tau_2$ . We obtain

$$U < \frac{D_m \Omega c_0 \Gamma}{R_p^2} \quad (4.22)$$

that is the sought estimate. In what follows we will see that

$$U_{\text{crit}} = C(\Phi) \frac{D_m \Omega c_0 \Gamma}{R_p^2},$$

where  $C(\Phi)$  depends only on the pore dihedral angle  $\Phi$ .

## 4.3 Mobility and critical velocity for a channel-like pore

In this section we use a simple analytical method to find both mobility and critical velocity of a channel-like cylindrical pore.

Let us consider a channel-like pore that is parallel to the  $OY$  axis; the corresponding large space scale is denoted by  $L_p$ . Along the  $OX$  axis the pore is positioned in the region  $-R_p < x < R_p$ ; the pore tips are at  $x = \pm R_p$ . An equilibrium pore can be illustrated by Fig. 3.3; the geometry of a stationary pore controlled by diffusion through the pore-filling fluid is identical to that with only surface diffusion at the grain-pore interface. As in Chapter 3, the two branches of the pore meet each other with the dihedral angle  $\Phi$

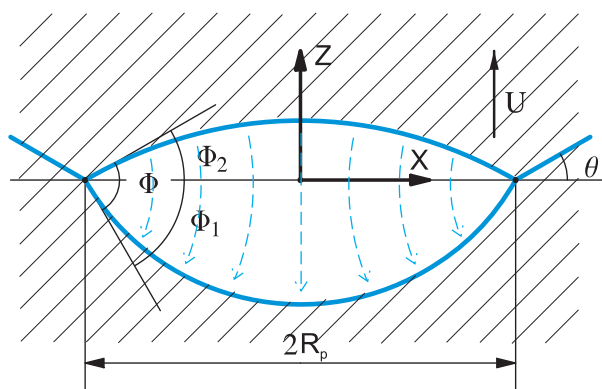


Figure 4.4: Pore motion because of diffusion through the pore-filling fluid. The curvature of the leading surface is smaller than that of the trailing surface. Therefore the concentration at the leading surface is larger than that at the trailing surface in accord with Eq. (4.5). The concentration gradient results in the diffusion flux shown by the arrows. This downwards transfer of matter is responsible for the upwards motion of the pore. For theoretical considerations both leading and trailing surfaces are approximated with circular segments.

determined by Eq. (3.20). The equilibrium pore shape is given by two circular segments with identical radius

$$R_{\text{eq}} = \frac{R_p}{\sin \Phi/2}, \quad (4.23)$$

which depends on the dihedral angle. The solution concentration inside the pore is constant and given by Eq. (4.5)

$$c_{\text{eq}} = c_0 \left( 1 - \frac{\Gamma}{R_{\text{eq}}} \right), \quad (4.24)$$

where we take into account that one of the principal curvatures of any channel-like pore is zero.

We now consider a pore that moves upwards with a constant velocity  $U$ . The motion is induced by the motion of a boundary between two grains of the solid matrix. Let us assume that the shape of the pore can still be approximated by two circular segments, the radii of the leading and trailing surfaces are now different, however, and they are denoted by  $R_2$  and  $R_1$ , respectively. In accord with Eq. (4.24) the boundary values of the solution concentration are

$$c_{s2} = c_0 \left( 1 - \frac{\Gamma}{R_2} \right), \quad c_{s1} = c_0 \left( 1 - \frac{\Gamma}{R_1} \right), \quad (4.25)$$

where  $R_2 > R_1$  and therefore

$$c_0 > c_{s2} > c_{s1}. \quad (4.26)$$

Note that for small velocities both pore surfaces are concave with respect to the surrounding grains and the corresponding curvatures are positive. However, with an increase of the velocity the leading surface can become convex (compare with Fig. 3.8). In this case the corresponding curvature becomes negative and the solution concentration at the leading surface reads  $c_{s2} = c_0(1 + \Gamma/R_2)$  and

$$c_{s2} > c_0 > c_{s1}. \quad (4.27)$$

In Eq. (4.26) and (4.27), the concentration at the leading surface is larger than that at the trailing surface  $c_{s2} > c_{s1}$ , and therefore there is a diffusion flux inside the pore that is directed downwards [Eq. (4.1)] counter wise to the direction of pore motion. Indeed this flux causes the upwards motion of the pore (Fig. 4.4).

The solution concentration inside the pore can be found as a solution of the Laplace equation (4.4) in two dimensions

$$\partial_x^2 c + \partial_z^2 c = 0 \quad (4.28)$$

with the boundary conditions

$$c|_{\text{leading}} = c_0 \left( 1 - \frac{\Gamma}{R_p} \sin \Phi_2 \right), \quad (4.29)$$

$$c|_{\text{trailing}} = c_0 \left( 1 - \frac{\Gamma}{R_p} \sin \Phi_1 \right), \quad (4.30)$$

where the angles  $\Phi_{1,2}$  are between the pore branches and the  $OX$  axis (Fig. 4.4), the dihedral angle  $\Phi = \Phi_1 + \Phi_2$ .

It should be stressed that by considering leading and trailing surfaces as cylindrical (or spherical) segments we make an approximation that is not quite satisfactory especially at the pore tips. The advantage is that the mathematical problem, as was initially given in Section 4.1.1, is greatly simplified. In particular, in two spatial dimensions the problem allows for an exact solution. The key point is that a test function [Lavrentjev and Shabat, 1998]

$$\arctan \left( \frac{2z}{1 - x^2 - z^2} \right)$$

satisfies the Laplace equation (4.28) and takes identical values at each circle segment connecting two points at  $x = \pm 1$ . These values are  $-\Phi_1$  and  $\Phi_2$  for

the segments shown in Fig. 4.4. One can therefore look for a solution of our problem in the form

$$\frac{c}{c_0} = A \arctan \left( \frac{2R_p z}{R_p^2 - x^2 - z^2} \right) + B,$$

where  $A$  and  $B$  are suitable constants and we scaled the coordinates to have pore tips at  $x = \pm R_p$ . To obtain these constants one solves the following system

$$\begin{aligned} -A\Phi_1 + B &= 1 - \frac{\Gamma}{R_p} \sin \Phi_1, \\ A\Phi_2 + B &= 1 - \frac{\Gamma}{R_p} \sin \Phi_2, \end{aligned}$$

and obtains

$$\begin{aligned} A &= \frac{\Gamma}{R_p} \frac{\sin \Phi_1 - \sin \Phi_2}{\Phi_1 + \Phi_2}, \\ B &= 1 - \frac{\Gamma}{R_p} \frac{\Phi_1 \sin \Phi_2 + \Phi_2 \sin \Phi_1}{\Phi_1 + \Phi_2}. \end{aligned}$$

The result for the concentration reads

$$\begin{aligned} \frac{c}{c_0} = 1 + \frac{\Gamma/R_p}{\Phi_1 + \Phi_2} \left[ (\sin \Phi_1 - \sin \Phi_2) \arctan \left( \frac{2R_p z}{R_p^2 - x^2 - z^2} \right) \right. \\ \left. - \Phi_1 \sin \Phi_2 - \Phi_2 \sin \Phi_1 \right], \quad (4.31) \end{aligned}$$

the latter equation can also be checked by a direct substitution. The values of  $\Phi_{1,2}$  can be expressed through the dihedral angle  $\Phi$  and the pore drag angle  $\Theta_p$  as

$$\Phi_{1,2} = \frac{1}{2}\Phi \pm \Theta_p. \quad (4.32)$$

Equation (4.31) uniquely determines the concentration of the solution for given values of  $R_p$ ,  $\Gamma$ ,  $\Phi$ ,  $\Theta_p$ . It is convenient to rewrite it in the form

$$\frac{c}{c_0} = \frac{2\Gamma \cos \Phi/2}{R_p \Phi} \sin \Theta_p \arctan \left( \frac{2R_p z}{R_p^2 - x^2 - z^2} \right) + \text{const},$$

where the last term on the right-hand-side accumulates all terms in Eq. (4.31), which do not depend on space coordinates and therefore do not contribute to the particle flux  $\mathbf{j}$  [Eq. (4.1)].

We recall that the moving pore is assumed to belong to the region  $|x| \leq R_p$  with the tips at  $x = \pm R_p$ . In principle, the pore size  $2R_p$  can change as the pore velocity increases. Therefore, similar to Chapter 3, our problem posing is that of a stationary motion for given values of  $R_p$  and  $U$ .

Let us now calculate the velocity of the pore. To this end we calculate  $j_z|_{z=0}$ , i.e., the flux of atoms across the  $OX$  axis for  $-R_p < x < R_p$ . We have [Eq. (4.1)]

$$j_z|_{z=0} = -D_m \left( \frac{\partial c}{\partial z} \right)_{z=0} = -\frac{4 \cos \Phi/2}{\Phi} \frac{D_m \Gamma c_0}{R_p^2 - x^2} \sin \Theta_p$$

and the total number of atoms transferred per second reads

$$J = \iint (-j_z|_{z=0}) dx dy = L_p \int_{-R_p}^{R_p} (-j_z|_{z=0}) dx, \quad (4.33)$$

where integration is over the pore cross section. The integral (4.33) can be related to the pore velocity

$$J\Omega = 2R_p LU$$

and therefore

$$U = \frac{2 \cos \Phi/2}{\Phi} \frac{D_m \Omega \Gamma c_0}{R_p} \sin \Theta_p \int_{-R_p}^{R_p} \frac{dx}{R_p^2 - x^2}.$$

At first glance, the last expression cannot be accepted because the integral is infinite. The reason is that exactly at  $x = \pm R_p$  our approximation is not valid, because the pore curvature should be continuous at the tips and cannot be equal to both  $1/R_1$  and  $1/R_2$  with  $R_1 \neq R_2$ . One can assume that in some region near the tips the approximation of the constant curvatures is violated, however these regions cause only small contribution to the total particle flux and can be ignored during calculation of the pore velocity. The characteristic scale of these special tip regions is denoted by  $\Delta$  and is much smaller than  $R_p$ . Therefore we assume that the integral should be calculated over the region  $|x| < R_p - \Delta$

$$\int_{-R_p+\Delta}^{R_p-\Delta} \frac{dx}{R_p^2 - x^2} = \frac{1}{R_p} \ln \frac{2R_p - \Delta}{\Delta} \approx \frac{1}{R_p} \ln \frac{2R_p}{\Delta}$$

and we obtain

$$U = \frac{2 \cos \Phi/2}{\Phi} \frac{D_m \Omega \Gamma c_0}{R_p^2} \sin \Theta_p \ln \frac{2R_p}{\Delta}.$$

We see that the dependence on the ratio  $R_p/\Delta$  is logarithmic and the exact value of this ratio is not so important, e.g. one can define  $\Delta$  very differently without changing the result for  $U$  much. A reasonable choice is  $\Delta \sim \Gamma$ , because the latter quantity is a characteristic length for the curvature to change. This factor is denoted  $C_{\log}$ . Therefore, we rewrite the result as

$$U = C_{\log} \frac{2 \cos \Phi/2}{\Phi} \frac{D_m \Omega \Gamma c_0}{R_p^2} \sin \Theta_p, \quad (4.34)$$

where  $C_{\log} = \ln(2R_p/\Gamma)$  is always of order 1. Finally we recall that  $\cos \Phi/2$  is proportional to  $\gamma_b/\gamma_s$  [Eq. (3.20)] and that  $\Gamma$  is proportional to  $\gamma_s$  [Eq. (4.6)]. Therefore the resulting expression for the pore velocity reads

$$U = \frac{C_{\log}}{\Phi} \frac{\gamma_b D_m \Omega^2 c_0}{R_p^2 kT} \sin \Theta_p. \quad (4.35)$$

### 4.3.1 Pore Mobility

Let us assume that the pore velocity is small so that its description in terms of pore mobility is appropriate. The pore drag force reads

$$K_{\text{pore drag}} = 2L_p \gamma_b \sin \Theta_p$$

and therefore Eq. (4.35) results in the following expression for the pore mobility

$$M_p = \frac{U}{K_{\text{drag}}} = \frac{C_{\log}}{2\Phi} \frac{D_m \Omega^2 c_0}{L_p R_p^2 kT}. \quad (4.36)$$

It is useful to rewrite the last equation in terms of pore volume, because the latter cannot change for a water filled pore at constant pressure and temperature. The volume of an equilibrium pore is given by the expression (3.71) where the possible difference between  $R_{\text{eq}}$  and  $R_p$  can be neglected. Finally we have

$$M_p = \frac{C_{\log}}{2} \frac{\Phi - \sin \Phi}{\Phi \sin^2 \Phi/2} \frac{D_m \Omega^2 c_0}{V_p kT}. \quad (4.37)$$

The latter expression is finite for all values of  $\Phi \in [0, \pi]$  and is our main result for the pore mobility. The second factor represents the dependence on dihedral angle (Fig. 4.5).



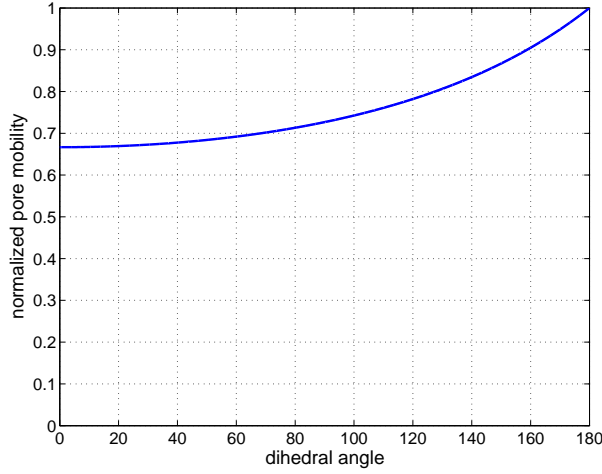


Figure 4.5: Normalized pore mobility  $M_p$  versus dihedral angle  $\Phi$ . The mobility is calculated for constant pore volume in accord with Eq. (4.37). The factor  $C_{\log}/2$  is included in the normalization.

As we see, the pore mobility only slightly depends on the dihedral angle. For estimates one can always use an expression

$$M_p \simeq \frac{D_m \Omega^2 c_0}{V_p kT} \quad (4.38)$$

that is correct to order 1.

### 4.3.2 Critical velocity

The perturbation theory for surface diffusion from Chapter 3 is a systematic Taylor expansion: using the ansatz given by Eq. (3.47) one can first find terms linear in  $u$ , then quadratic ones, then cubic corrections, and so on. The expansion is, however, valid only for small velocities. An analytical approach for diffusion through the pore-filling fluid from this chapter essentially given by Eq. (4.31) is an approximation and cannot be improved stepwise. On the other hand, small velocities are not assumed here and one can find the critical pore velocity directly from Eq. (4.35). The maximal value of the drag force is for  $\Theta_p = \pi/2$  and therefore the maximal possible velocity reads

$$U_{\max} = \frac{C_{\log}}{\Phi} \frac{\gamma_b D_m \Omega^2 c_0}{R_p^2 kT}. \quad (4.39)$$

This is our main result for the separation problem in the case that diffusion through the pore-filling fluid controls the pore motion. Note, the critical

velocity becomes large for fixed  $R_p$  and small values of  $\Phi$ . The underlying geometry is illustrated in Fig. 4.6.

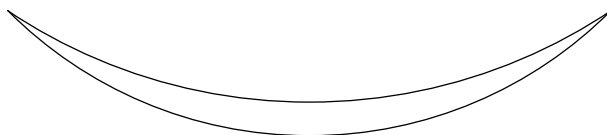


Figure 4.6: Moving pore for small values of the dihedral angle  $\Phi$ . Note that a finite jump between the equilibrium values of  $c_s$  on the leading and trailing surfaces occurs on a small length scale that is proportional to  $\Phi$ . This results in a large flux proportional to  $1/\Phi$  and correspondingly in a large velocity of the pore in accord with Eq. (4.39).

In this case the difference between the boundary values of the concentrations reads

$$c|_{\text{leading}} - c|_{\text{trailing}} = c_0 \left(1 + \frac{\Gamma}{R_2}\right) - c_0 \left(1 - \frac{\Gamma}{R_1}\right) \approx c_0 \frac{2\Gamma}{R_1},$$

where  $R_1 \approx R_2$ . This change of  $c$  occurs on a small distance and causes a large diffusion flux. Correspondingly the resulting pore velocity also is large in accord with Eq. (4.39). In other words, a decrease of  $\Phi$  decreases the distance that should be passed by diffusing atoms [Raj, 1982]. If, instead of  $R_p = \text{const}$ , one considers a pore with constant volume,  $R_p$  increases with the decrease  $\Phi$ . Here, for a channel-like pore  $R_p^2 \Phi \approx \text{const}$  and two effects compensate each other. Of course, even for  $R_p = \text{const}$  the singularity for  $\Phi = 0$  cannot be reached. Indeed, for  $\Phi \rightarrow 0$ , the expressions (4.29–4.30) should be reconsidered simply because the solution concentration must be continuous. Also the time derivative in Eq. (4.3) cannot be ignored. The latter situation is out of scope of Eq. (4.3.2).

## 4.4 Critical velocity for a lenticular pore

With only small changes the technique developed in the previous section can be applied to a lenticular pore. Note, that Fig. 3.3 still illustrates the equilibrium pore, the latter has now rotational symmetry and can be obtained by rotation of the cross-section around the  $OZ$  axis.

For the moving 3D pore the pore-boundary interfaces are approximated with spherical caps and the transport mechanism for the matrix atoms is diffusion through the pore-filling fluid (Fig. 4.4), where the pore image also

must be rotated around the  $OZ$  axis. The boundary conditions read

$$c_{s2} = c_0 \left(1 - \frac{2\Gamma}{R_2}\right), \quad c_{s1} = c_0 \left(1 - \frac{2\Gamma}{R_1}\right), \quad (4.40)$$

where we take into account that the two principal curvatures are identical. Equation (4.28) is replaced by the radially symmetric version of (4.4), i.e.,

$$\frac{1}{r} \frac{\partial}{\partial r} \left( r \frac{\partial c}{\partial r} \right) + \frac{\partial^2 c}{\partial z^2} = 0, \quad (4.41)$$

where the pore is positioned in the region  $r < R_p$  and  $r = \sqrt{x^2 + y^2}$ .

The solution strategy is as follows. All length are normalized by  $R_p$ . We first fix the dihedral angle  $\Phi$  and choose several values for the drag angle  $\Theta_p$ . For each value we restore the geometry of the pore and in particular calculate the radii of the spherical segments  $R_{1,2} = R_p / \sin \Phi_{1,2}$ , where [Eq. (4.32)]  $\Phi_{1,2} = \Phi/2 \pm \Theta_p$ . The Laplace equation (4.41) is then solved numerically within the pore. The result is a space distribution of  $c$  that should be used instead of Eq. (4.31). In fact, only the difference  $c - c_0$  must be calculated, the latter is normalized according to

$$\bar{c} = -\frac{R_p}{\Gamma} \left( \frac{c}{c_0} - 1 \right)$$

as suggested by (4.31), the negative sign ensures positive values of  $\bar{c}$ , at equilibrium  $\bar{c}_{\text{eq}} = 2 \sin \Phi/2$ . The normalized boundary conditions read

$$\bar{c}_{s2} = 2 \sin \Phi_2, \quad \bar{c}_{s1} = 2 \sin \Phi_1.$$

Several examples of numerical solutions are shown in Fig. 4.7. For each solution one can calculate the particle flux [Eq. (4.1)]

$$\mathbf{j} = \frac{D_m \Gamma c_0}{R_p^2} \nabla \bar{c},$$

where  $\nabla$  is taken over the normalized coordinates. The flux is integrated to get the total number of atoms that are transferred across the pore per second

$$J = \frac{D_m \Gamma c_0}{R_p^2} I,$$

where the integral  $I$  is determined over the trailing pore surface

$$I = \iint (\mathbf{n} \nabla \bar{c}) dS = R_p^2 \iint (\mathbf{n} \nabla \bar{c}) d\bar{x}\bar{y},$$

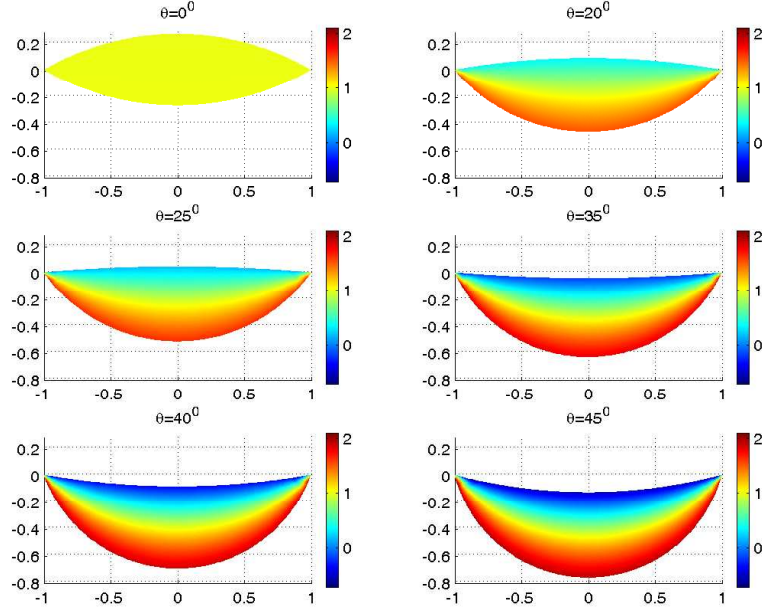


Figure 4.7: Several solutions of Eq. (4.41) obtained numerically with the boundary conditions (4.40) for  $\Phi = \pi/3$  and different values of  $\Theta_p$  as shown by labels. Density plot of  $\bar{c}(r, z)$  is shown.

and  $\mathbf{n}$  denotes the corresponding unit normal vector. Similar to section 4.3 the integration is actually performed over a smaller region, we have taken  $\bar{r} < 0.9$  instead of  $\bar{r} < 1$ . In addition, integration limits of  $\bar{r} = 0.85$  and  $\bar{r} = 0.95$  were tried but did not significantly affect the value of the integral.

The pore velocity is calculated as

$$U = \frac{J\Omega}{\pi R_p^2} = \frac{D_m \Omega \Gamma c_0}{R_p^2} \frac{1}{\pi} \iint (\mathbf{n} \nabla) c \, d\bar{x}\bar{y}. \quad (4.42)$$

For each value of the dihedral angle, velocity normalized in accord with Eq. (4.42)

$$u = U \left/ \frac{D_m \Omega \Gamma c_0}{R_p^2} \right. .$$

exhibits a maximum (Fig. 4.8). The maximum is, however, not reached for  $\Theta_p = \pi/2$  as for channel-like pores [Eq. (4.34)], but for intermediate values of the drag angle that systematically decrease with increasing dihedral angle.

Similar to the result for channel-like pores [Eq. (4.39)] the critical velocity strongly increases with decreasing dihedral angle (Fig. 4.9). The decrease can

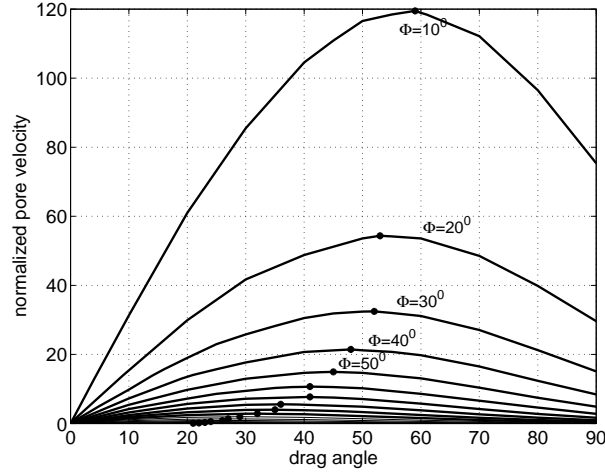


Figure 4.8: Normalized pore velocity versus drag angle for different values of the dihedral angle as shown by the labels. The maximum values of the pore velocity are shown by points.

be closely approximated by an analytical expression guessed from Eq. (4.39)

$$u_{\max} = 16.4 \frac{\cos \Phi/2}{\Phi}. \quad (4.43)$$

The correspondence between the numerical calculations and the analytical approximation is quite good. Returning to physical units we obtain from Eq. (4.43)

$$U_{\max} = \frac{8.2}{\Phi} \frac{\gamma_b D_m \Omega^2 c_0}{R_p^2 kT} \quad (4.44)$$

in accord with Eq. (4.39). The latter equation is our main result to the separation problem for a lenticular pore.

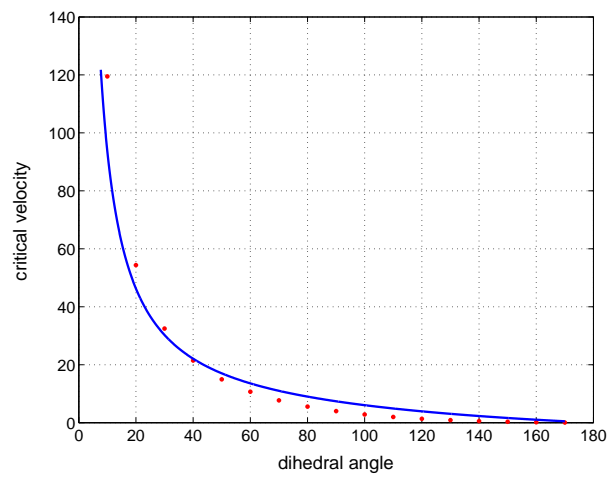


Figure 4.9: The normalized critical pore velocity is shown as a function of the dihedral angle. The numerical results are taken from Fig. 4.8 and are shown by points, the solid line is the analytical approximation (4.43).

# Chapter 5

## Conclusions

In this short chapter we summarize the most important new results from the previous chapters and discuss possible applications. A typical object that is described in this thesis is an elongated channel-like pore that can be formally considered as a two-dimensional object. The pore is embedded in a polycrystal, the latter is considered as a set of growing grains with the moving boundaries between them. We are interested in the pore-boundary interactions, especially in pores that are trapped by a moving boundary.

For coupled motion at small velocities, we calculated pore mobilities for several pore geometries and two important transport mechanisms. A straightforward application is to quantify the reduction of the boundary mobility by the attached pores in accord with Eq. (2.31) and (2.41).

An increase in boundary velocity greatly affects the shape of the dragged pore and at some critical velocity the coupled motion is not possible anymore. The pore is separated from the boundary. Our next main problem was to calculate this critical velocity for different pore geometries and different motion mechanisms. Also comparison of the pore mobilities and critical velocities for different mechanisms immediately reveals the dominating mechanism that controls drag and drop processes.

Pore separation is a highly complicated process that involves large perturbations of the pore. Therefore our investigations of the separation problem were mainly numerical. The numerical results were systematically approximated by simple analytical expressions, whose formulation was guided by the physical features of the process. Hence, practical calculation and comparison of the critical velocities in specific systems is possible.

Furthermore, we performed the first analysis of the numerical solutions for the pore in the vicinity of the singularity point. Therefore, we are confident that the results obtained in this thesis represent physical reality rather than numerical instabilities. This was necessary because of wide scattering of the

published data on drag and drop criteria (this is especially relevant for the dependence of critical velocity on dihedral angle, as discussed in section 1.4).

Let us now discuss the most important results of this thesis.

## 5.1 Boundary motion

### Critical velocities for grain boundaries

Previous investigations of pore drag dealt with a boundary migrating with constant velocity  $U$  driven by surface tension. Therefore we checked if such solutions are possible for the underlying boundary equations. For a boundary, e.g. with rotational symmetry, the corresponding solutions are readily obtained (see Fig. 2.6). For the two dimensional case, e.g. with the boundary parallel to  $OY$  axis, we encountered a new effect [Eq. (2.37)]: the boundary velocity cannot exceed the critical value

$$U_{\max} = \frac{\pi\mu_b\gamma_b}{2R_b},$$

where  $\mu_b$  and  $\gamma_b$  are the boundary mobility and surface tension coefficient, respectively; the boundary edges are positioned at  $x = \pm R_b$ .

### Global boundary mobility

We also investigated to which extent a boundary moving with constant velocity can be described in terms of mobility. The resulting global boundary mobility  $M_p$  [Eqs. (2.24) and (2.40)] reads

$$M_p = \frac{U}{K_{\text{drag}}} = \frac{\mu_b}{S},$$

where  $S$  is the boundary area. This expression is valid as long as the boundary is only slightly perturbed by the driving force, i.e., in the small slope approximation. We found that with increasing drag force the global mobility increases parabolically

$$M_p(U) = \frac{\mu_b}{S} \left( 1 + \frac{cU^2}{U_{\max}^2} \right)$$

with a dimensionless factor

$$c = \frac{\pi^2}{24} \approx 0.41$$



[see Eqs. (2.28)]. The increase is, however, relatively weak

$$M_p(U) \leq 1.41M_p,$$

because the velocity of a two dimensional boundary cannot exceed  $U_{\max}$ . In contrast, the nonlinear increase of the mobility in a three dimensional case can be large (see Eq. (2.39) for small velocities and Fig. 2.8 for arbitrary velocities).

## 5.2 Pore motion controlled by surface diffusion

### Mobility

Surface diffusion is the first transport mechanism that is considered in this thesis. Here, the main physical process is atomic motion along the pore-boundary interface caused by its nonuniform curvature. The resulting particle flux is proportional to curvature gradient, to  $D_s/(kT)$ , where  $D_s$  denotes surface diffusivity, and to  $\delta$  the width of the interface layer. An atom transported from the leading to the trailing pore surface increases volume of the growing grain by  $\Omega$ . We considered a channel-like pore with the tips at  $x = \pm R_p$  and the length  $L_p \gg R_p$ . The pore mobility reads

$$M_p = k_m(\Phi) \frac{D_s \Omega \delta}{kT L_p R_p^3},$$

where the ‘‘mobility factor’’  $k_m(\Phi) \approx 1$  depends on dihedral angle and geometry of the boundaries. A systematic way to calculate  $k_m(\Phi)$  was developed. The method was first applied to a channel-like pore at a boundary [Eq. (3.70)]. The resulting mobility is identical to that obtained previously from energy considerations [Svoboda and Riedel, 1992, Riedel and Svoboda, 1993]. Then our technique was applied to a pore at a triple junction [Eq. (3.96)], this expression for the mobility is new. Also both mobilities were calculated numerically; the correspondence between analytical and numerical results is very good (see Fig. 3.9 and Fig. 3.17).

Our results for  $k_m(\Phi)$  are summarized in Fig. 3.15. As we see, the dependence on dihedral angle is relatively weak. Also the pore mobility at a triple junction is approximately 30% smaller than that of the pore between the boundaries. In both cases a typical value of  $k_m(\Phi)$  is 0.5.

### Critical velocities

The coupled pore-boundary motion was treated numerically. With increasing velocity its relation to drag force becomes nonlinear. Also the pore shape becomes more and more deformed. At a critical velocity, no solution for coupled motion can be found. Our goal was to calculate this critical velocity for channel-like pores.

We returned to the viewpoint of the original papers [*Hsueh et al.*, 1982, *Spears and Evans*, 1982]. To this end we differently fixed the value of the common velocity and asked if a uniform coupled motion is possible. If so, the trapped pore self-organizes and becomes stationary in a moving coordinate frame, thereafter the pore shape and volume cannot change. To exclude artifacts due to numerical errors we carefully examined solutions near the critical velocity. Our results for  $U_{\max}$  can be summarized in a single equation

$$U_{\max} = k_s(\Phi) \frac{D_s \Omega \delta}{kT} \frac{\gamma_b}{R_p^3},$$

where the “separation factor”  $k_s(\Phi)$  depends on dihedral angle, direction of motion and geometry of the boundaries. In particular, the factor was non-zero for a circular pore. For the pore at a boundary the critical velocity is given in Eq. (3.75). It decreases with the increase of  $\Phi$ ; the critical velocity at  $\Phi = 0$  is almost 5 times larger than that for  $\Phi = \pi$ .

For the pore at a triple junction, two directions of motion must be distinguished, the results for the critical velocities are given in Eq. (3.100) and (3.101). Again,  $U_{\max}$  decreases several times with the increase of  $\Phi$ , but is nonzero for  $\Phi = \pi$ . Typical values of  $U_{\max}$  for the upward motion (Fig. 3.14) are approximately 10 times larger than that for the downward motion.

## 5.3 Diffusion through the pore-filling fluid

### Mobility and critical velocity

The second transport process we were interested in was diffusion of matrix atoms through the pore-filling fluid. Matrix atoms are dissolved from the leading surface, diffuse through the fluid, and precipitate on the trailing surface. The gradient in solution concentration causing the flux results from the dependence of local solubility on the curvature of the solid-liquid interfaces (Thompson-Freundlich relation). The curvature of the leading surface with respect to the upper grain is smaller (or even negative) than that of the trailing surface with respect to the lower grain (Fig. 4.4). Therefore the solution

concentration increases upwards and the diffusion flux is, in turn, directed downwards.

From a mathematical point of view one has to deal with the diffusion equation for the solution concentration in a permanently changing domain, where the boundary conditions are determined by the curvature of the boundaries. Because this problem is extremely complicated, only rough estimates can be found in the literature for the pore mobility and critical velocity [Monchoux and Rabkin, 2002]. In particular, systematic solution of the diffusion equation was not obtained, particle flux was artificially assumed to be parallel to the motion direction, dependence of the mobility and critical velocity on dihedral angle was not investigated, etc.

Considering this problem, we first started with an accurate mathematical formulation following [Mullins, 1960] strategy for a similar groove formation problem. To prove that the problem posing is mathematically correct we investigated stability of a plane interface and derived characteristic time scales that apply to the interface relaxation accommodated by diffusion through the pore-filling fluid. Then we considered motion of a channel-like cylindrical pore for the condition that the equilibrium solution concentration is established “instantaneously” relative to slow changes of boundary conditions.

Mathematical treatment of a stationary two-dimensional diffusion equation is much easier than that in three dimensions. Therefore it was possible to find an exact solution for the solution concentration in a channel-like pore where both interfaces have constant curvatures. The relation between the drag force and the resulting pore velocity was found as above. The induced diffusion flux is proportional to the ratio  $D_m/(kT)$  where  $D_m$  is volume diffusivity of the matrix atom in the solution. The pore geometry is as above characterized by two parameters  $R_p$  and  $L_p$ . The pore mobility reads

$$M_p = \frac{C_{\log}}{2\Phi} \frac{D_m \Omega^2 c_0}{L_p R_p^2 kT},$$

where  $c_0$  is the equilibrium solution concentration for a plain interface. Here  $C_{\log} \approx \ln(10^7 R_p / 1 \text{ cm})$ . An interesting point is that if one keeps  $R_p = \text{const}$  and decreases  $\Phi$  the mobility increases (see Fig. 4.6 for explanation). If, however, one keeps the pore volume constant, as it is natural for the fluid filled pore, the value of the mobility is finite for all values of  $\Phi$  [see Eq. (3.72)].

Using the exact solution for the solution concentration the maximal pore velocity can be also found. The result reads

$$U_{\max} = \frac{C_{\log}}{\Phi} \frac{\gamma_b D_m \Omega^2 c_0}{R_p^2 kT}.$$

To our knowledge this is a new result that quantifies critical velocity controlled by the diffusion through the pore-filling fluid. The result directly shows how  $U_{\max}$  depends on the dihedral angle.

Close investigation shows that this approach is not restricted to channel-like pores but can be also applied to lenticular pores. The only significant difference is that in order to replace the analytical solution given by Eq. (4.31) one has to solve the stationary diffusion equation numerically. We have performed this for a lenticular pore with rotational symmetry. The expression for the critical velocity is identical to that for the channel-like pore, again the quantity  $C_{\log}$  can be calculated only to logarithmical accuracy, in our example its numerical value was  $\sim 10$ .

### Controlling mechanism

All above considerations were made either for surface diffusion or diffusion through the pore-filling fluid. However, these two transport processes occur always simultaneously with different efficiency. Using our results, it is straightforward to identify the controlling transport mechanism. Indeed, the ratio of critical velocities for two mechanisms reads

$$\frac{U_{\max}^{\text{surface}}}{U_{\max}^{\text{volume}}} = \Phi \frac{k_s(\Phi)}{C_{\log}} \frac{D_s}{D_m} \frac{\delta}{R_p} \frac{1}{\Omega c_0},$$

where the separation factor  $k_s(\Phi) \sim 1$  as calculated above. The ratio of pore mobilities for two mechanisms reads

$$\frac{M_p^{\text{surface}}}{M_p^{\text{volume}}} = \Phi \frac{2k_m(\Phi)}{C_{\log}} \frac{D_s}{D_m} \frac{\delta}{R_p} \frac{1}{\Omega c_0},$$

where the mobility factor  $k_m(\Phi) \approx 0.5$  as calculated above. Therefore it is useful to introduce a dimensionless parameter

$$\xi = \frac{\Phi}{C_{\log}} \frac{D_s}{D_m} \frac{\delta}{R_p} \frac{1}{\Omega c_0},$$

where the numerical factor  $C_{\log}$  is of order 10. The pore drag and drop is controlled by surface diffusion if  $\xi \gg 1$ . Diffusion through the pore-filling fluid dominates if  $\xi \ll 1$ .

# Notation

| Symbol                         | Comment   |
|--------------------------------|---|
| $\mathcal{K}_b$                | Normal driving force per unit area of the boundary              |
| $K_{\text{drag}}$              | Total drag force acting on the boundary or pore                 |
| $D_s$                          | Diffusivity of matrix atoms on the pore surface                 |
| $D_m$                          | Diffusivity of matrix atoms in water                            |
| $\gamma_b$                     | Surface tension coefficient of the grain-grain interface        |
| $\gamma_s$                     | Surface tension coefficient of the pore-grain interface         |
| $\mu_b$                        | Local boundary mobility   |
| $M_b$                          | Global boundary mobility  |
| $M_p$                          | Pore mobility   |
| $\Omega$                       | Volume per atom into the matrix                                 |
| $\delta$                       | Effective boundary width  |
| $\kappa = \kappa_1 + \kappa_2$ | Main and mean curvatures of the surface                         |
| $U$ (or $u$ )                  | Pore or boundary velocity (normalized)                          |
| $\mathcal{F}(t, x, y, z)$      | Is used for the implicit boundary definition                    |
| $f(t, x, y)$                   | Is used for the explicit boundary definition                    |
| $F(x, y)$                      | Is used for the explicit boundary description in a moving frame |
| $\mathcal{G}(t, x, y, z)$      | Is used for the implicit pore definition                        |
| $g(t, x, y)$                   | Is used for the explicit pore definition                        |
| $G(x, y)$                      | Is used for the explicit pore description in a moving frame     |
| $R_b$                          | Boundary size, $ x  < R_b$ in 2D and $r < R_b$ in 3D            |
| $R_p$                          | Pore size, $ x  < R_p$ in 2D and $r < R_p$ in 3D                |
| $L_b, L_p$                     | Large ( $\parallel OY$ ) scale of a boundary or a pore in 2D    |
| $\theta$                       | Boundary slope angle  |
| $\varphi$                      | Pore slope angle  |
| $\Theta_b$                     | Boundary drag angle. Last value of $\theta$                     |
| $\Theta_p$                     | Pore drag angle. Last value of $\varphi$                        |
| $c$                            | Solution concentration  |
| $c_s$                          | Interface value of the solution concentration                   |
| $\Gamma$                       | See Eq. (4.6). Is used for $c_s$ definition                     |
| $V_p$                          | Pore volume   |



# Bibliography

- [Arzt, 1998] Arzt, E. Size effects in materials due to microstructural and dimensional constraints: a comparative review. *Acta Mater.*, 46, 5611–5626, 1998.
- [Atkinson, 1988] Atkinson, H. V. Theories of normal grain growth in pure single phase systems. *Acta Metall.*, 36, 469–491, 1988.
- [Beck, 1954] Beck, P. A. *Adv. Phys.*, 3, 245, 1954.
- [Bolling and Winegard, 1958] Bolling, G. F. and W. C. Winegard. *Acta Metall.*, 6, 283, 1958.
- [Brook, 1969] Brook, R. J. Pore-boundary interactions and grain growth. *J. Am. Ceram. Soc.*, 52, 56–57, 1969.
- [Burke, 1948] Burke, J. E. *Metal. Tech. T. P.*, page 2472, 1948.
- [Burke and Turnbull, 1952] Burke, J. E. and D. Turnbull. Recrystallization and Grain Growth. *Prog. Metal. Phys.*, 3, 220, 1952.
- [Crank, 1975] Crank, J. *The mathematics of diffusion*. Oxford University Press, Oxford, 1975.
- [Drolet and Galibois, 1968] Drolet, J. P. and A. Galibois. *Acta Metall.*, 16, 1387, 1968.
- [Dubrovina et al., 1992] Dubrovina, B. A., A. T. Fomenko, and S. P. Novikov. *Modern geometry — methods and applications*. Springer-Verlag, New York, 1992.
- [Evans et al., 2001] Evans, B., J. Renner, and G. Hirth. A few remarks on the kinetics of static grain growth in rocks. *Int. J. Earth Sci.*, 90, 88–103, 2001.

- [*Exner, 1972*] Exner, H. E. Analysis of grain- and particle-size distributions in metallic materials. *International metallurgical reviews*, 17, 25–42, 1972.
- [*Feltham, 1957*] Feltham, P. Grain growth in metals. *Acta Metall.*, 5, 97–105, 1957.
- [*Fujita, 1952a*] Fujita, H. The exact pattern of a concentration-dependent diffusion in a semi-infinite medium, Part I. *Textile Research Journal*, 22, 757, 1952a.
- [*Fujita, 1952b*] Fujita, H. The exact pattern of a concentration-dependent diffusion in a semi-infinite medium, Part II. *Textile Research Journal*, 22, 823, 1952b.
- [*Genin et al., 1993*] Genin, F. Y., W. W. Mullins, and P. Wynblatt. The effect of stress on grain-boundary grooving. *Acta Metall. Mater*, 41, 3541–3547, 1993.
- [*Gordon and Bassyouni, 1965*] Gordon, P. and T. A. E. Bassyouni. *Trans. Am. Inst. Min. Engrs.*, 233, 391, 1965.
- [*Gottstein and Shvindlerman, 1999*] Gottstein, G. and L. S. Shvindlerman. *Grain Boundary Migration in Metals: Thermodynamic, Kinetics, Applications*. CRC Press, 1999.
- [*Haken, 2004*] Haken, H. *Synergetics: Introduction and Advanced topics*. Springer-Verlag, Berlin, 2004.
- [*Hilbert, 1965*] Hilbert, M. *Acta Metall.*, 13, 227, 1965.
- [*Hollister and Crawford, 1981*] Hollister, L. and M. Crawford. *Short Course in Fluid Inclusions: Applications to Petrology*, volume 6. Mineralogical Association of Canada, Calgary, Canada, 1981.
- [*Holmes and Winegard, 1959*] Holmes, E. L. and W. C. Winegard. *Acta Metall.*, 7, 411, 1959.
- [*Hsueh et al., 1982*] Hsueh, C. H., A. G. Evans, and R. L. Coble. Microstructure development during final/intermediate stage sintering — I. Pore-grain boundary separation. *Acta Metall.*, 30, 1269, 1982.
- [*Hu, 1974*] Hu, H. *Can. Metall. Q.*, 13, 275, 1974.



- [Huang et al., 2004] Huang, M., Y. Wang, and Y. A. Chang. *Thin Solid Films*, 449, 113, 2004.
- [Hunderi and Ryum, 1980] Hunderi, O. and N. Ryum. *J. Mater. Sci.*, 15, 1104, 1980.
- [Jankowski and Hayes, 2004] Jankowski, A. and J. Hayes. The evaporative deposition of aluminum coatings and shapes with grain size control. *Thin Solid Films*, 447–448, 568, 2004.
- [Kaur et al., 1995] Kaur, I., Y. Mishin, and W. Gust. *Fundamentals of grain and interphase boundary diffusion*. John Wiley & Sons Ltd, Chichester, 1995.
- [Lavrentjev and Shabat, 1998] Lavrentjev, M. and B. Shabat. *Metody teorii funkzij kompleksnogo peremennogo (in russian)*. Nauka, 1998.
- [Lifshitz and Slyozov, 1961] Lifshitz, I. M. and V. V. Slyozov. The kinetics of precipitation from supersaturated solid solutions. *J. Phys. Chem. Solids*, 19, 35–50, 1961.
- [Louat, 1974] Louat, N. P. *Acta Metall.*, 22, 721, 1974.
- [Monchoux and Rabkin, 2002] Monchoux, J. P. and E. Rabkin. Microstructure evolution and interfacial properties in the Fe-Pb system. *Acta Mater.*, 50, 3159–3174, 2002.
- [Mullins, 1956] Mullins, W. W. Two dimensional motion of idealized grain boundaries. *J. Appl. Phys.*, 27, 900, 1956.
- [Mullins, 1957] Mullins, W. W. Theory of thermal grooving. *J. Appl. Phys.*, 28, 333, 1957.
- [Mullins, 1960] Mullins, W. W. Grain-boundary grooving by volume diffusion. *AIME Trans.*, 218, 354–361, 1960.
- [Mullins and Sekerka, 1960] Mullins, W. W. and R. F. Sekerka. Morphological stability of a particle growing by diffusion or heat flow. *J. Appl. Phys.*, 34, 323–329, 1960.
- [Mullins and Shewmon, 1959] Mullins, W. W. and P. G. Shewmon. The kinetics of grain-boundary grooving in cooper. *Acta Metall.*, 7, 163–170, 1959.

- [Nes *et al.*, 1985] Nes, E., N. Ryum, and O. Hunderi. On the Zener drag. *Acta Metall.*, 33, 11, 1985.
- [Neumann, 1952] Neumann, J. V. *Metal Interfaces*. American Society for Testing of Materials, Cleveland, 1952.
- [Nichols, 1968] Nichols, F. A. Further comments on the theory of grain growth in porous materials. *J. Am. Ceram. Soc.*, 51, 468–469, 1968.
- [Partington, 1952] Partington, J. *An advanced treatise on physical chemistry*. Longmans, 1952.
- [Petrishcheva and Renner, 2005] Petrishcheva, E. and J. Renner. Two-dimensional analysis of pore drag and drop. *Acta Mater.*, 53, 2793–2803, 2005.
- [Petrishcheva *et al.*, 2006a] Petrishcheva, E., J. Renner, and R. Abart. Pore drag and drop: volume diffusion control. In *EGU General Assembly*. European Geosciences Union, 2006a.
- [Petrishcheva *et al.*, 2006b] Petrishcheva, E., J. Renner, and R. Abart. Volume diffusion controlled pore drag and drop at moving grain boundary. In *84 Jahrestagung*. Deutsche Mineralogische Gesellschaft, 2006b.
- [Raj, 1982] Raj, R. Creep in polycrystalline aggregates by matter transport through a liquid phase. *J. Geophys. Res.*, 87, 4731–4739, 1982.
- [Ramasubramaniam and Shenoy, 2005] Ramasubramaniam, A. and V. B. Shenoy. On the evolution of faceted grain-boundary grooves by surface diffusion. *Acta Mater.*, 53, 2943–2956, 2005.
- [Renner *et al.*, 2002a] Renner, J., B. Evans, and G. Hirth. Grain growth and inclusion formation in partially molten carbonate rocks. *Contrib. Mineral. Petrol.*, 142, 501–514, 2002a.
- [Renner *et al.*, 2002b] Renner, J., B. Evans, and G. Siddiqi. Dislocation creep of calcite. *J. Geophys. Res.*, 107(B12), doi:10.1029/2001JB001680, 2002b.
- [Riedel and Svoboda, 1993] Riedel, H. and J. Svoboda. A theoretical study of grain growth in porous solids during sintering. *Acta Metall. Mater.*, 41, 1929, 1993.
- [Roedder, 1984] Roedder, E. *Fluid Inclusions*, volume 12. Mineralogical Society of America, Washington, DC, 1984.

- [Sedov, 1959] Sedov, L. I. *Similarity and dimensional methods in mechanics*. Academic, London, 1959.
- [Shewmon, 1964] Shewmon, P. G. The movement of small inclusions in solids by a temperature gradient. *Trans. Metall. Soc. AIME*, 230, 1134–1137, 1964.
- [Smith, 1948a] Smith, C. S. *Trans. Amer. Inst. Min. Met. Eng.*, 175, 5, 1948a.
- [Smith, 1948b] Smith, C. S. Grains, phases, and interactions: An interpretation of microstructure. *Trans. Metall. Soc. AIME*, 175, 15, 1948b.
- [Smith, 1952] Smith, C. S. In *Metal Interfaces*. Amer. Soc. Met., Cleveland, OH, 1952.
- [Smith, 1964a] Smith, S. C. *Rev. Mod. Phys.*, page 524, 1964a.
- [Smith, 1964b] Smith, S. C. *Metall. Rev.*, 9, 1, 1964b.
- [Spears and Evans, 1982] Spears, M. A. and A. G. Evans. Microstructure development during final/intermediate stage sintering — II. Grain and pore coarsening. *Acta Metall.*, 30, 1281, 1982.
- [Svoboda and Riedel, 1992] Svoboda, J. and H. Riedel. Pore-boundary interactions and evolution equations for the porosity and the grain size during sintering. *Acta Metall. Mater.*, 40, 2829, 1992.
- [Takei, 2002] Takei, Y. Effect of pore geometry on  $V_P/V_S$ : From equilibrium geometry to crack. *J. Geophys. Res.*, 107, 2043, 2002.
- [Thompson, 1982] Thompson, J. M. *Instabilities and Catastrophes in Science and Engineering*. Chichester, Wiley, 1982.
- [Underwood, 1970] Underwood, E. E. *Quantitative Stereology*. Addison-Wesley, 1970.
- [von Bargen and Waff, 1986] von Bargen, N. and H. S. Waff. Permeabilities, interfacial areas and curvatures of partially molten systems: results of numerical computations of equilibrium microstructures. *J. Geophys. Res.*, 91, 9261–9276, 1986.
- [Weaire and Rivier, 1984] Weaire, D. and N. Rivier. *Contemporary Phys.*, 25, 59, 1984.

- [*Yan et al.*, 1977] Yan, M. F., R. F. Cannon, and H. K. Bowen. *Ceramic microstructures. Grain boundary migration in ceramics*, volume 76. Westview Press, Boulder, 1977.
- [*Yu and Suo*, 1999] Yu, H. and Z. Suo. An axisymmetric model of pore-grain boundary separation. *J. Mech. Phys. Solids*, 47, 1131, 1999.
- [*Zener*, 1949] Zener, C. Theory of growth of spherical precipitates from solid solution. *J. Appl. Phys.*, 20, 950–953, 1949.

## Lebenslauf

von Frau Elena Petrishcheva  
aus Obninsk, Russland  
21.11.2006

|                |                                 |
|----------------|---------------------------------|
| Name:          | Elena Petrishcheva              |
| Geburtsdatum:  | 26.05.1965                      |
| aus            | Obninsk, Russland               |
| Adresse:       | Marienstr., 3<br>D-12207 Berlin |
| Familienstand: | verheiratet<br>zwei Kinder      |

### Schul- und Hochschulbildung

|           |  |
|-----------|--|
| 1972-1982 | Schule, Obninsk, Russland                            |
| 1982      | Abitur   |
| 1983-1990 | Diplomstudium Physik/Geophysik<br>Universität Moskau |

### Beruflicher Werdegang

|                 |  |
|-----------------|--|
| 1982-1983       | Labortechnikerin<br>Fakultät für Physik<br>Universität Moskau  |
| 1990-2001       | Lecturer für Physik<br>Lehrstuhl für Physik und Mathematik<br>Universität für Atomtechnologie<br>Obninsk, Russland |
| 02/2003-09/2005 | Wissenschaftliche Mitarbeiterin<br>Institut für Geologie,<br>Mineralogie und Geophysik<br>Ruhr-Universität Bochum  |
| seit 10/2005    | Wissenschaftliche Mitarbeiterin<br>Institut für Geologische Wissenschaften<br>Freie Universität Berlin             |